REPORT ON ERS-1 SAR INTERFEROMETRIC TECHNIQUES AND APPLICATIONS

C. Prati
F. Rocca
A. Monti Guarnieri
P. Pasquali

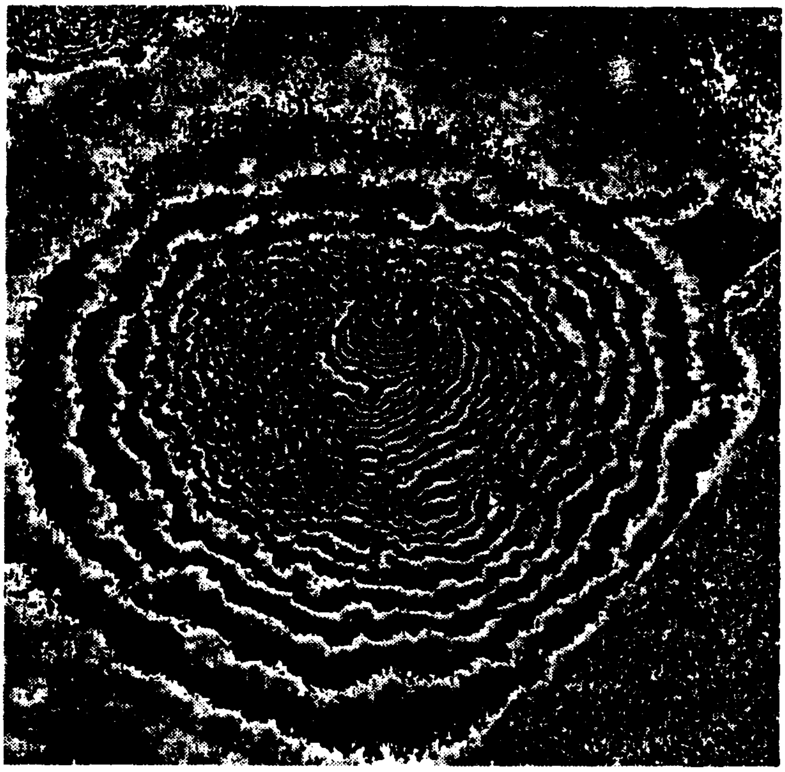

Dipartimento di Elettronica - Politecnico di Milano
Piazza L. da Vinci, 32 - 20133 Milano - Italy
Ph.: +39 2 2399 3585 - Fax: +39 2 2399 3413 - e.mail: prati@ipmel2.elet.polimi.it

June 1994

ESA STUDY CONTRACT REPORT

ESA CONTRACT N.:	SUBJECT: Final report on "ERS-1 SAR	NAME OF CONTRACTOR:
10179/93/YT/I/SC	Interferometric Techniques and Applications	POLIMI

ESA CR( ) N.:	STAR CODE	N. of Volumes: 1 This is Volume N.: 1	CONTRACTOR'S REFERENCE

ABSTRACT:

This report deals with applications of ERS-1 SAR interferometry: separation of layover areas, estimation and uses of coherence, separation of surface and volume scattering, phase unwrapping for DEM generation, ground range resolution improvement (super-resolution), monitoring small terrain changes. After a short introduction where the interferometric SAR geometry and main ERS-1 parameters are presented, sections 2 and 3 deal with the monochromatic and the spectral shift approach for SAR interferograms generation. The spectral shift approach is then applied to the separation of layover areas. In section 4 the complex coherence is introduced. Processing techniques have to be reconsidered to avoid coherence losses due to incorrect processing. The effects of all the processing steps are analyzed. In section 5, examples of the coherence use are presented. Namely they are: detection of exposed rocks terrain (examples of old lava flows on Mt. Etna and Mt. Vesuvius are shown), identification of areas where SAR data are usable for interferometric fringes generation, separation of volume and surface scattering (synthetics and real ERS-1 data of the area of Bonn are presented). In section 6, phase unwrapping is dealt with. A deterministic technique as well as LMS one are presented. It is also shown that the best phase unwrapping results can be achieved with a combination of the two techniques. Section 7 is dedicated to the measurement of small terrain motions. Finally in chapter 8, the super-resolution technique is analyzed in detail. It is shown how multiple interferometric SAR images should be combined in order to get an improved range resolution SAR image. A 4 meters range resolution image of Bonn obtained with the combination of 6 ERS-1 images is shown.

Names of authors:

Claudio Prati
Fabio Rocca
Andrea Monti Guarnieri
Paolo Pasquali

NAME OF ESA STUDY MANAGER	ESA BUDGET HEADING
Dr. M. Doherty / Dr. S. Coulson Earth Observation Division - ESRIN	60.512

Contents

List of Figures

Chapter 1

INTRODUCTION

One of the peculiarities of Synthetic Aperture Radar (SAR) systems is their capability of recording both amplitude and phase of the backscattered echoes.

The phase of each pixel (ground resolution cell) of a focused SAR image is the sum of three distinct contributions:

1 - the two-ways travel path (sensor-target-sensor: hundreds of kilometers in the satellite case) that, divided by the used wavelength (a few centimeters), corresponds to millions of cycles;
2 - the interaction between the incident e.m. waves and the scatterers within the ground resolution cell;
3 - the phase shift induced by the processing system used to focus the image.

Therefore, the phase of a single SAR image is of no practical use.

On the contrary, if two SAR images from slightly different viewing angles are considered (*stereo pair*), it will be shown that their phase difference (*interferometric fringes*) can be usefully exploited to generate Digital Elevation Maps (DEMs), to monitor terrain changes and to improve the range resolution. The interferometric fringes image is derived as the phase of the SAR *interferogram*, that is the complex image formed by cross-multiplying the two SAR images.

The relation between the interferometric fringes and ground elevation is usually explained by means of the *monochromatic approach* [1, 2]. It is based on the assumption that the RF bandwidth is so small (and this is the case of most satellite systems including SEASAT, ERS-1, JERS-1 and the forthcoming ERS-2 and RADARSAT) to be negligible. Thus the system is considered monochromatic.
We shall see, however, that this approximation hides an important aspect of the interferometric fringes generation mechanism. In fact, if the finite bandwidth of the system is considered (*spectral shift* approach), a relative shift of the ground wavenumber spectra dependent on the baseline and the local slope is found. A few important consequences come out from this result [6, 7].
Both approaches will be dealt with in this text. In particular, the simpler monochromatic approach will be used in section 2 to show the relationship between the relative terrain elevation and the interferometric fringes. In section 3 a deeper insight into SAR interferometry will be given by exploiting the wavenumber shift approach. After these two sections, section 4.3 will be dedicated to a more practical description of the *interferogram* generation. In section 6 the *phase*

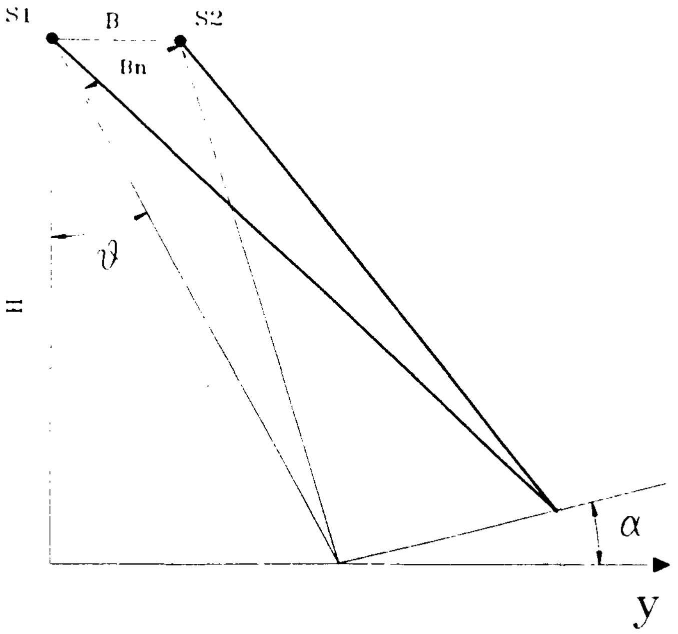

Figure 1.1: Interferometric SAR geometry (see table 1).

unwrapping problem will be addressed. Eventually, the last two sections 7 and 8 will be dedicated to the description of advanced topics of SAR interferometry: small terrain motion detection and slant range resolution enhancement.

Symbols that will be used through the text (together with the main ERS-1 parameters, used as a reference system) are summarized in table 1.1 and figure 1.1.

Symbol	Meaning	ERS-1
λ	wavelength	5.66 cm
$f_o = c/\lambda$	central frequency	5.3 GHz
W	system bandwidth	16 MHz
f_s	sampling frequency	18.96 MHz
$f_{Ny} = f_s/2$	Nyquist frequency	9.48 MHz
θ	off-nadir angle	23^o
α	local terrain slope (range)	
H	platform altitude	780 km
ρ_s	slant range resolution	9.375 m
Δz	slant range sampling interval	7.91 m
$\rho_g \simeq \rho_s / \sin(\theta - \alpha)$	ground range resolution	
B	horizontal interferometer baseline	
B_n	B project. normal to the look direction	
B_{nc}	critical baseline	$\simeq$ 1100m for $\alpha = 0$
r	slant range axis	
r_o	sensor-target distance	
y	ground range axis	
k_y	ground range wave number	
ϕ	interferometric phase	

Table 1.1: List of symbols

Chapter 2

THE MONOCHROMATIC APPROACH

Let us consider two complex SAR images from two slightly different viewing angles (see figure 1.1), v_1 and v_2. If non simultaneous acquisitions are considered, we shall suppose, for the sake of simplicity, that the terrain backscatter did not change.

Let us now exploit the "monochromatic approximation": the relative system bandwidth is so small (i.e in the ERS-1 case its value is $3 \cdot 10^{-3}$) to be neglected. Thus, the phase difference ϕ between correspondent complex pixels in v_1 and v_2 is proportional to the travel path difference $2\Delta r_o$ (the factor 2 accounts for the two ways travel path):

$$\phi = \frac{4\pi}{\lambda}\Delta r_o \tag{2.1}$$

The interferometric phase ϕ of a single pixel is still of no practical use. The travel path difference $2\Delta r_o$ is usually much greater than the wavelength λ (in most of the practical cases, the travel path difference from the satellite can be as large as a few hundred meters whereas the used wavelength is of the order of a few centimeters) and the measured phase ϕ shows an ambiguity of many cycles. On the other hand, passing from one pixel to its neighbour (only a few meters apart in the slant range direction), the variation of the travel path difference $(\Delta(\Delta r_o))$ may be much smaller than the used wavelength (we shall see in the following under which conditions this is true) and the variation of the interferometric phase $\Delta\phi$ is not ambiguous. Moreover, a simple relation between $\Delta\phi$ and the relative terrain elevation can be derived.
For this purpose let us refer to the system of coordinate axes of figure 2.1.

Here we have indicated the position of the two SAR sensors (S_1 and S_2) and their relative displacements parallel (r_s) and normal (n_s) to the slant range direction. We have also indicated the position of two point scatterers and their relative displacements parallel (r_p) and normal (n_p) to the slant range direction. Let us assume as a reference the positions of S_1 and P_1 with their relative distance r_o. By changing the sensor and target position by (r_p, n_p) and (r_s, n_s) respectively the sensor-target distance becomes:

$$r = \sqrt{(r_o + r_p - r_s)^2 + (n_p - n_s)^2} \tag{2.2}$$

Since the distance between the two SAR sensors is generally much smaller than the

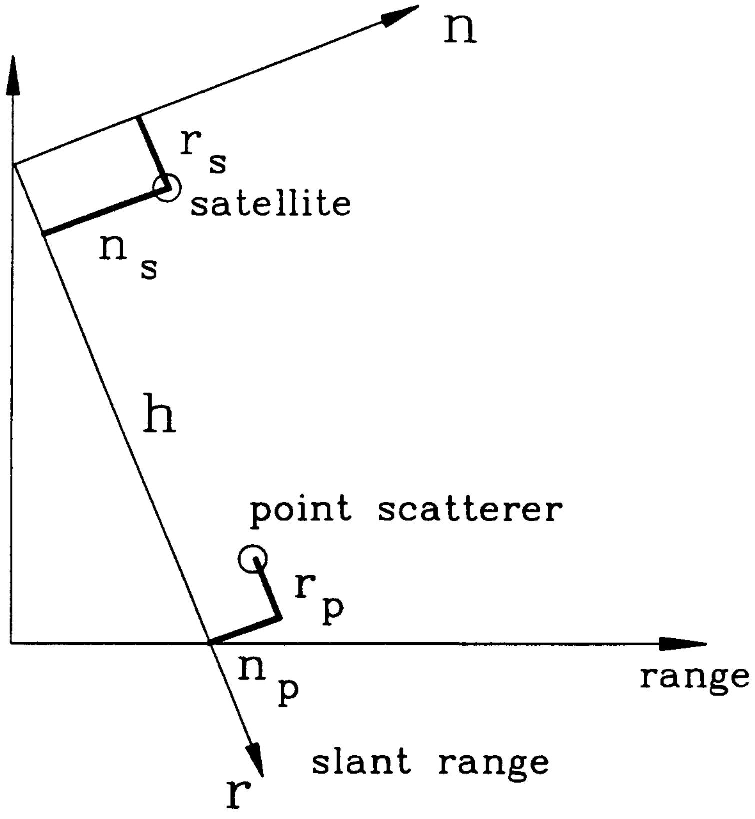

Figure 2.1: Description of the coordinates system utilized in this text.

sensor-target distance $r_\circ$ (a few hundred meters compared with 800km, in the ERS-1 case), the distance variation $\Delta r_\circ$ induced by a change of the sensor position can be approximated with the differential:

$$\Delta r_\circ = \frac{\partial r}{\partial n_s}\big|_{r_p=r_s=n_p=n_s=0} \cdot n_s + \frac{\partial r}{\partial r_s}\big|_{r_p=r_s=n_p=n_s=0} \cdot r_s \tag{2.3}$$

Then, the variation of this function with respect to the backscatterer position can be expressed as:

$$\Delta(\Delta r_\circ) = \frac{\partial \Delta r_\circ}{\partial n_p}\big|_{r_p=r_s=n_p=n_s=0} \cdot n_p + \frac{\partial \Delta r_\circ}{\partial r_p}\big|_{r_p=r_s=n_p=n_s=0} \cdot r_p = \tag{2.4}$$

$$= \frac{\partial^2 r}{\partial n_s \partial n_p}\big|_{r_p=r_s=n_p=n_s=0} \cdot n_p n_s + \frac{\partial^2 r}{\partial n_s \partial r_p}\big|_{r_p=r_s=n_p=n_s=0} \cdot n_s r_p +$$

$$+ \frac{\partial^2 r}{\partial r_s \partial r_p}\big|_{r_p=r_s=n_p=n_s=0} \cdot r_s r_p + \frac{\partial^2 r}{\partial r_s \partial n_p}\big|_{r_p=r_s=n_p=n_s=0} \cdot r_s n_p \tag{2.5}$$

It can be shown that all second derivatives in the previous equation are zero, but for the first one which depends on the points and satellite displacement measured along the direction *normal* to the *slant range*.
Thus, the final expression of $\Delta(\Delta r_\circ)$ becomes:

$$\Delta(\Delta r_\circ) = \frac{n_s n_p}{r_\circ} \tag{2.6}$$

Consequently, the following expression of the interferometric phase variation holds:

$$\Delta\phi = \frac{4\pi}{\lambda}\Delta(\Delta r_\circ) = \frac{4\pi n_s n_p}{\lambda r_\circ} \tag{2.7}$$

This result shows that if we know the relative displacement of the two orbits normal to the slant range direction n_s, the distance $r_\circ$ and the value of the SAR wavelength λ, then the phase difference $\Delta\phi$ depends only on the n_p value, i.e. on the elevation difference between the points displayed in Figure 2.1, measured in the direction normal to the slant range axis.

Thus the interferometric phase image represents a map of the relative terrain elevation with respect to the slant range direction. However since our interest is an elevation map (with respect to a horizontal plane) the phase image must be modified.

2.1 Flattening the interferometric phase image

Let us derive the form of the phase difference $\Delta\phi$ for flat terrain.
Consider the point scatterers of Figure 2.2: they have the same drop with respect to the horizontal reference level, but their normal displacement n_p is different. Consequently they do not, according to equation 2.7, produce the same phase difference $\Delta\phi$.

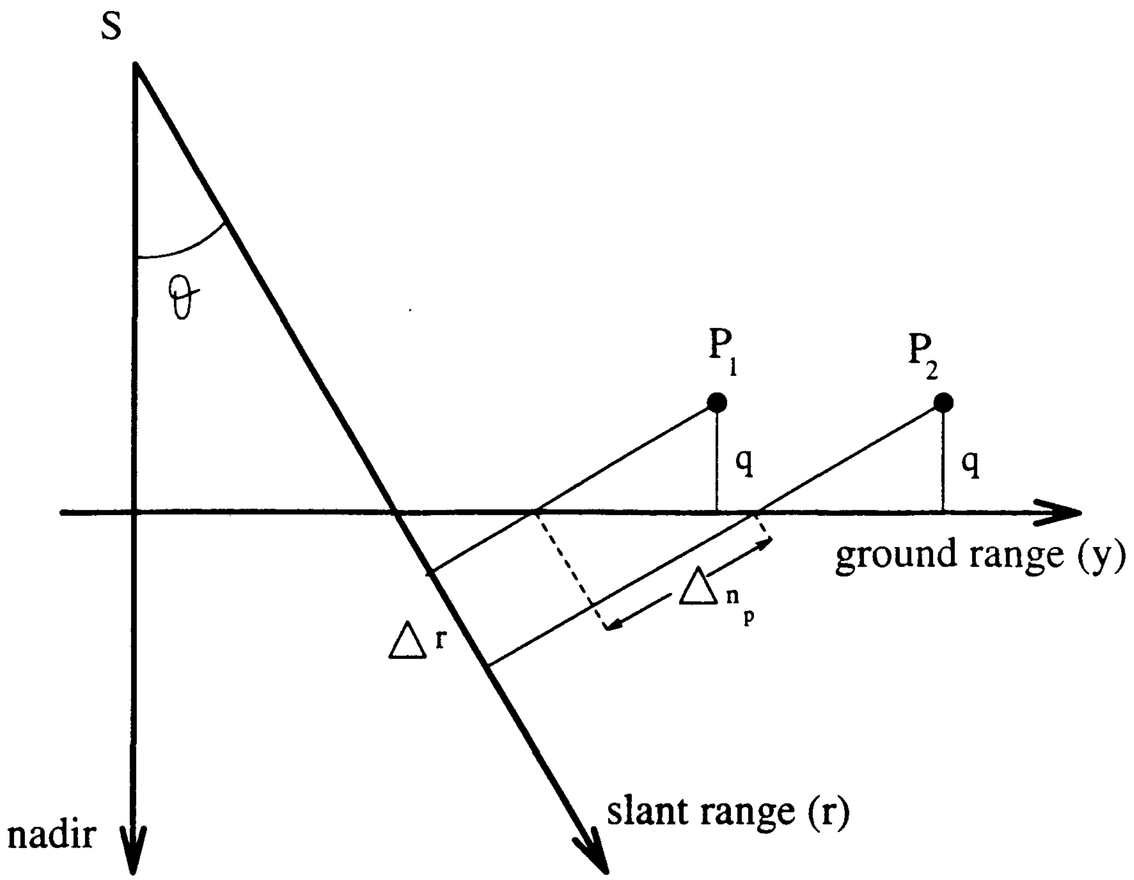

Figure 2.2: Displacement normal to the slant range direction with flat terrain.

The difference of the coordinates along the normal direction of these points can be computed easily:

$$n_p = \frac{\Delta r}{\tan\theta} \tag{2.8}$$

where Δr is the slant range displacement and θ the off-nadir angle of the SAR antenna. Therefore through equation 2.6 the phase difference is:

$$\Delta\phi = \frac{4\pi n_s \Delta r}{\lambda r_o \tan\theta} \tag{2.9}$$

For flat terrain the phase differences of the interferometrical image have a linear dependence on slant range variation Δr; in other words the SAR system transforms a horizontal plane into an inclined one (in practice, this is just a first approximation valid for a range swath much smaller than the sensor-target distance r_o). A linear term can then be subtracted from the interferometric phase so that the phase corresponding to flat terrain will be a constant; otherwise, its changes will be proportional to the elevation.

The desired result can be obtained by subtracting the linear term 2.9 from the phase of the

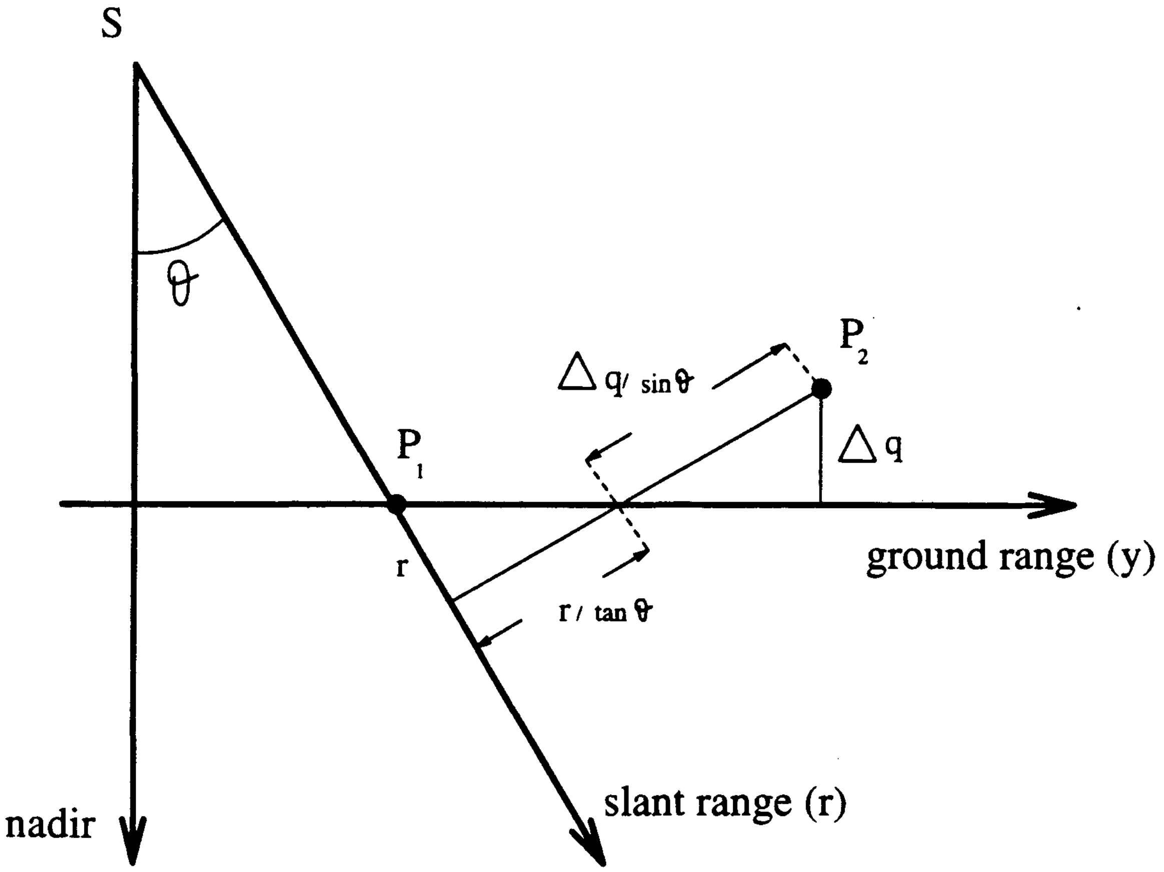

Figure 2.3: Displacement normal to the slant range direction after the geometrical compensation.

interferometrical image. After some algebra, the version of equation 2.6 that refers to the elevation with respect to a flat terrain becomes:

$$\Delta\phi = \frac{4\pi n_s q}{\lambda r_o \sin\theta} = K \cdot q \tag{2.10}$$

According to this equation the topography variations q are proportional to the interferometric phase variations of the corresponding points. Therefore, if the value of the parameters related to constant K are known, a relative elevation map of the terrain can be obtained from the interferometric phase image [1].

From now on, we shall call B_n the normal baseline, that is the normal displacement between the satellites n_s.

2.2 Approximate determination of the baseline

If the value of the parameters related to the constant K of equation 2.10 are not available with high accuracy, the elevation map is affected by large but systematic errors. This type of errors, however, can be strongly reduced if the elevation of a few Ground Control Points (GCP) is known [8].

Let us suppose that there is a path that, as we shall see in the next section, allows phase unwrapping, i.e. unambiguous phase determination, across the entire range swath. By fitting the interferometric phase at the GCP's to their known elevation it is possible to estimate the unknown geometric parameters of the satellite (i.e the two baseline components, the platform elevation, the closest approach distance and the convergence rate of the orbits with azimuth). In the case of ERS-1 the swath is about 100 km and the simple approximated relations between phase and elevation of equations 2.7 and 2.10 are no longer valid. A more accurate model that takes into account the geometric variations with range must be adopted and the following expression of the interferometric phase holds:

$$\phi = \frac{4\pi}{\lambda}\left(\sqrt{B_y^2 + B_z^2 + r^2 + 2B_z(H-q) - 2B_y\sqrt{r^2-(H-q)^2}} - r\right) \tag{2.11}$$

The exact expression of the elevation q can now be derived from equation 2.11 and fitted to the elevation of the GCPs by changing the four parameters H, r_o (the closest approach distance), B_y and B_z. It can be shown that the estimated elevation q has a weak dependence on the first two parameters, whereas it has a very strong dependence on a combination of the two baseline components. This can be clearly seen if we plot the phase error as a function of the two components B_y and B_z (see figure 2.4). As expected, the error function is, as a first approximation, a flat valley in the direction along which the combination of B_y and B_z produces an almost constant normal baseline component n_s.

---

[1] Note that the resultant expression 2.10 was derived on the assumption that the sensor-target distance is much greater than the considered range swath. This assumption is correct for the spacecraft case only if a range swath no larger than a few hundred meters is considered. On the contrary the approximation is not valid for larger range swaths or in the case of SAR airborne images, and the exact expression of $\Delta\phi$ must be derived starting from equations 2 and 2.1.

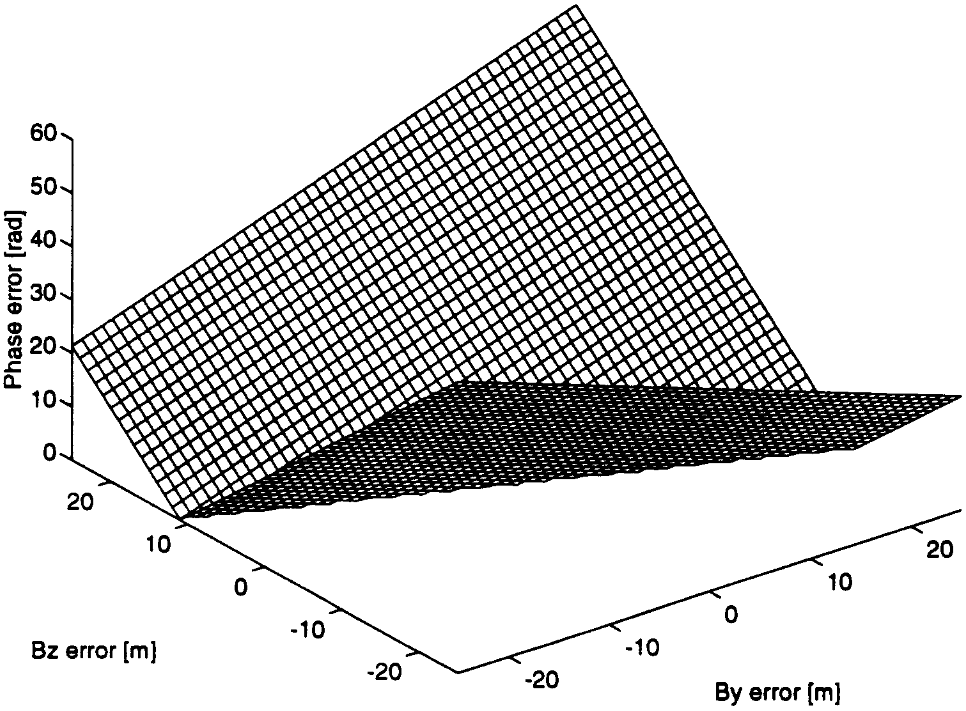

Figure 2.4: Phase error as a function of the two baseline components B_y and B_z.

It is clear that the accuracy of the estimated geometric parameters depends on the GCP's elevation error. Just to have an idea of the role played by the GCP's elevation error on the systematic elevation error on the whole swath, let us consider the following simple example: only 3 almost regularly spaced GCPs are available over the whole swath. In the following, we shall not consider the interferometric phase noise since it can be regarded as an equivalent (baseline dependent) GCP's elevation error.

The elevation error curve along the swath induced by the parameters' error is essentially limited to its first and second order components. Thus, the worst situation is met in the following cases.

The elevation errors (including the effect of the phase noise) of the first and second GCP are at their positive (negative) maximum (M), and that of the last GCP is at its negative (positive) maximum ($-M$).

In this case, the second order curve that fits the data is a parabola with its apex located in the middle of the first two GCP's where its value is $+5/4M$. Thus, the elevation error on the whole swath will not be greater than 9/4 the largest GCP elevation error. Of course, if the 3 GCP's of our example are not regularly spaced (i.e the last two are very close to each other, a situation that must be avoided in practice) greater errors will be found.

In conclusion, if just a few GCP's are available, they should be almost regularly spaced along the swath and their elevation error should be as small as the requested elevation error of the map (this is the typical situation where artificial GCP's, as corner reflectors, are used). On the other hand, if many GCP's are available (i.e. railtracks, power lines, roads, coastlines, etc. ...), the systematic elevation error will be limited to the linear and parabolic components of the GCP's elevation error. Since the GCP's elevation error is a zero mean random variable, the amplitude of these components is inversely proportional to the number of GCP's. Thus, with N GCP's available, the requirements on their elevation accuracy is approximately reduced by a $1/\sqrt{N}$ factor.

2.2.1 The Bonn experiment

An experimental validation of the possibilities of SAR interferometry to obtain DEM has been carried out in a cooperation between ESA-ESRIN (mission planning and organization), INS-University of Stuttgart (fields experiment), and Politecnico di Milano (data processing). Here, we shall summarize the main results of the processing of the data, obtained through this international cooperation [24].

From the 2^{nd} to the 29^{th} of March 1992, ERS-1 surveyed ten times (i.e every three days) the area around Bonn. The experiment for DEM validation and centimetric motion detection has been conducted on a smaller area in the south west of the city of Bonn (in the central part of image 2.6). An array of 19 corner reflectors (1.4 meters) was deployed by INS Stuttgart along a 20 km spread in the across-track direction. Since corners were positioned very precisely by means of differential GPS, they have been exploited to estimate the effective baseline.

The precise layout of the corner reflectors allowed, besides the precise estimate of the baseline, the creation of a phase reference for the areas of terrain surrounding the corner reflectors. To this scope, a big rectangular field centered around each corner reflector, with sides of 8 pixels (363.4m) in ground range and 20 pixels (164.8m) along azimuth respectively, was identified; the 80 central pixels (a 8x10 pixels rectangle), dominated by the echo of the corner reflector, were

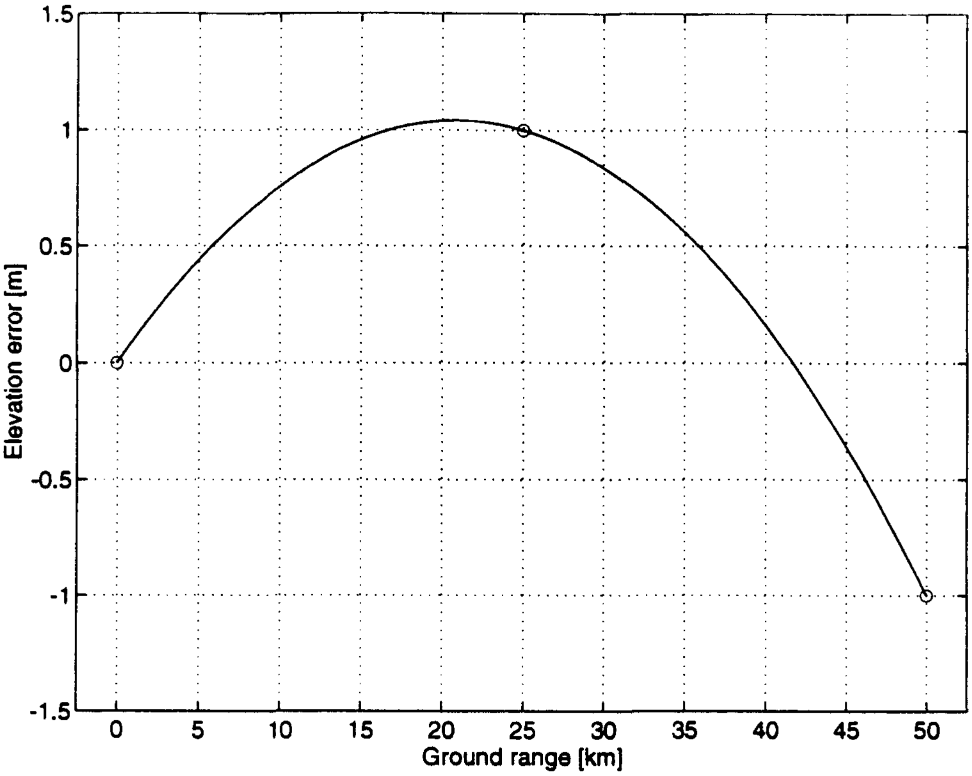

Figure 2.5: Elevation error curve along the swath induced by GCPs elevation errors. GCPs positions are indicated with a circle.

Figure 2.6: Detected image of corner reflectors area near Bonn.

discarded to avoid unwanted combination of the effects.

Complex values of the pixels in that area were averaged; before that, a slowly varying phase term was removed to compensate for the earth slope and curvature and possible centimetric difformities of the orbits (azimuth fringes); bias, linear, and quadratic phase terms along the array were fitted to the DEM provided by GPS and removed.

In figure 2.7 we show the derived elevations of those areas compared with differential GPS (the largest elevation error is less than 5 meters). It is also shown the elevation carried out by averaging 7 interferometric images (the elevation error is now reduced to about 2 meters).

It can be noted that by averaging the passes, the elevations, debiased using GCPs, appear to converge to those yielded by differential GPS.

2.3 Principal phase values

Up to now it has been assumed that the phase difference $\Delta\phi$ of equation 2.10 would be directly obtained from the interferometric fringes. However such an assumption is in some way misleading. In fact, from the interferogram, the complex values $e^{j\Delta\phi}$ can be determined but not the $\Delta\phi$ values themselves. Moreover, it is obvious that an infinite number of phase angles differing by an integer

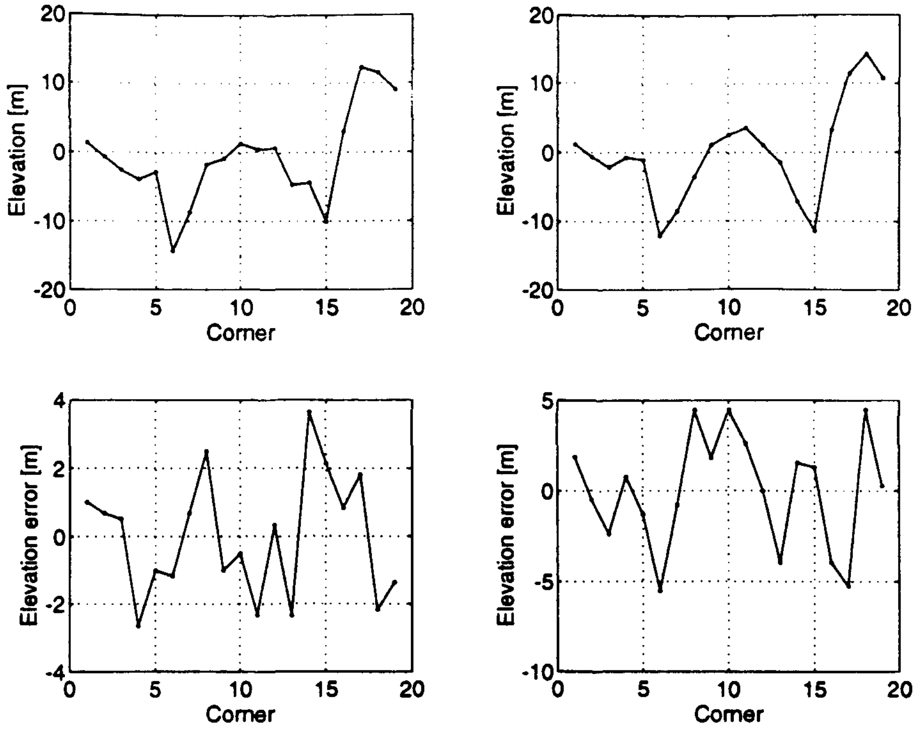

Figure 2.7: DEMs of the terrain surrounding the corner reflectors. Upper left: Differential GPS. Upper right: Average of 7 interferometric surveys. Lower left: Difference GPS - average. Lower right: Difference GPS - 10-9 interferometric survey.

multiple of 2π radians can correspond to $e^{j\Delta\phi}$. In other words, what is measured from the interferometrical image is not the phase difference value $\Delta\phi$, but its principal value $\Delta\phi_p$, limited between $-\pi$ and $+\pi$. Furthermore, as the principal phase values are limited, the interferometrical fringes show typical discontinuities like those shown in figure 2.8.

The two adjacent discontinuities separated by a constant elevation increment, corresponding to a 2π phase drop, represent the height contours of the terrain elevation map.

However, since the real phase values are " wrapped" around a 2π interval, to obtain the correct map (and, thus, the correct labels of each contour line), the principal phase values must be *"unwrapped"* as it will be shown in section 6.

In conclusion we can say that while the phase difference $\Delta\phi$ between adjacent pixels is generally not ambiguous ($\Delta\phi = \Delta\phi_p$) as said in section 2, this may be not true for distant pixels. In other words, what can be directly measured from the interferometric fringes is the elevation difference between close pixels or, as it will be discussed in section 3, the local terrain slope. Thus, as will be discussed in section 6, the phase unwrapping problem can be usefully approached as the problem of the integration of the estimated local slopes of the terrain.

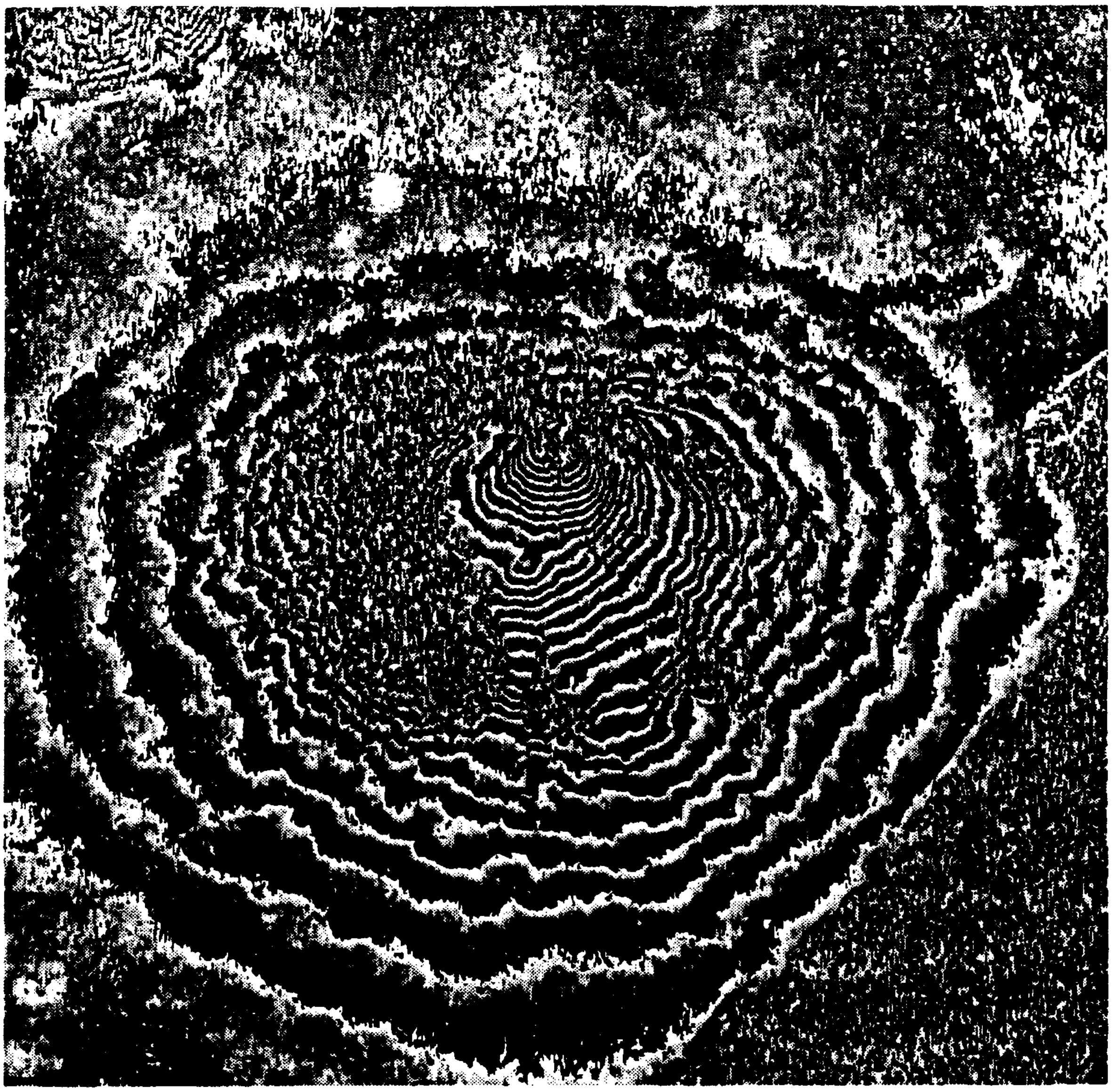

Figure 2.8: ERS-1 - Mt. Vesuvius (Italy) August 27th and September 5th, 1991. - Interferometric fringes. The estimated normal baseline is $B_n = 193$meters.

Chapter 3

THE WAVENUMBER SHIFT APPROACH

The above described monochromatic approximation, notwithstanding its simplicity, hides an important aspect of the interferogram generation mechanism that will be discussed in this section.

Let us consider the approximated relation between the frequency f and the ground wavenumber k_y (along the range direction y as shown in figure 1.1). It can be easily derived by projecting the transmitted wavelength λ, measured along the slant range direction, on the terrain. For sake of simplicity we shall suppose that the terrain has a constant slope α. Thus, as a first approximation, the wavelength λ projected on the terrain is scaled by the factor $1/\sin(\theta-\alpha)$. Then, the factor 2 accounting for the two ways travel path, the following expression of the ground wavenumber holds:

$$k_y = \frac{4\pi}{\lambda}\sin(\theta-\alpha) = \frac{4\pi f}{c}\sin(\theta-\alpha) \tag{3.1}$$

Thus, in general, a looking angle difference $\Delta\theta$ generates a shift and a stretch of the imaged terrain spectra. However, if the relative system bandwidth is small, the frequency f in the second term of equation 3.1 can be substituted with the central frequency $f_\circ$. The stretch can be neglected and the following equation holds.

$$\Delta k_y = \frac{4\pi f_\circ \Delta\theta}{c}\cos(\theta-\alpha) \tag{3.2}$$

Finally, since the radar is not monochromatic (we have a bandwidth W centered around the central frequency $f_\circ$), we can conclude that by changing the looking angle of the SAR acquisition, we get a different corrispondence between the ground reflectivity spectrum and the radiofrequency spectrum.

Now, in order to compare the shift of the ground reflectivity spectrum with the SAR bandwidth W, it is worth to express the ground wavenumber shift of equation 3.2 as an equivalent frequency shift Δf. The following expression of Δf for an angular separation $\Delta\theta$ can be obtained by differentiation of equation 3.1 directly,

$$\Delta f = -\frac{f_\circ \Delta\theta}{\tan(\theta-\alpha)} = -\frac{cB_n}{r_\circ \lambda \tan(\theta-\alpha)} \tag{3.3}$$

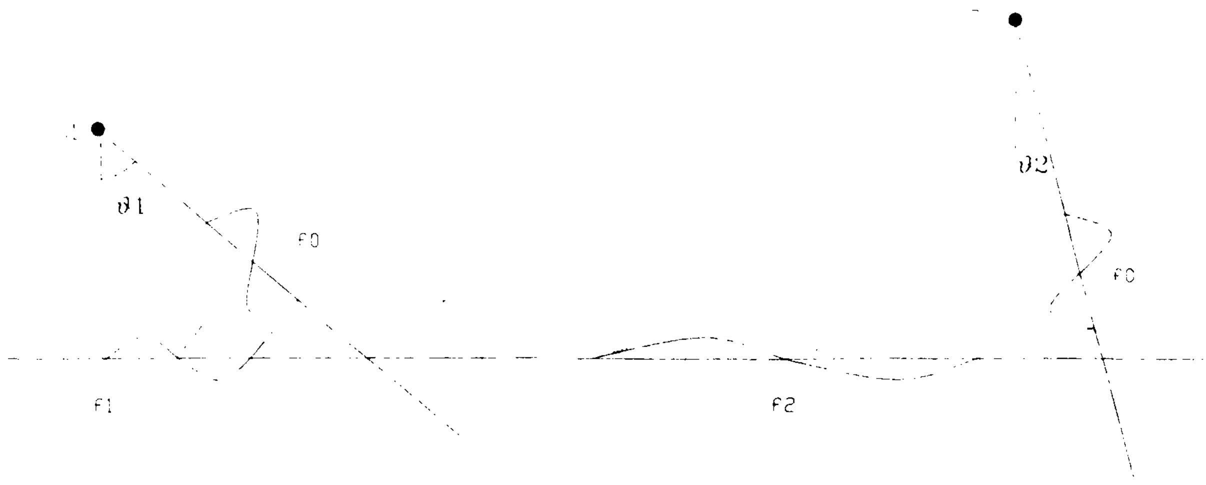

Figure 3.1: The wavenumber shift principle. By changing the looking angle of the SAR acquisition we get different wavenumbers of the ground reflectivity spectrum.

We would like to stress again that equation 3.3 does not state that by changing the looking angle of the SAR acquisition the radar bandwidth is shifted by Δf. It just says that by changing the SAR looking angle, the backscattered signal contains different spectral components of the ground reflectivity spectrum. In other words, if we look at the signals received by two SARs separated by an angle $\Delta\theta$, equation 3.3 states that the same spectral components of the first signal are found in the second spectrum shifted by Δf.

In figure 3.1 the wavenumber shift principle is sketched.

Different bands of the ground reflectivity spectrum (limited by the finite bandwidth of the SAR systems) observed from slightly different looking angles are shown. Notice that whenever the spectral shift Δf is smaller than the system bandwidth W, we have that only part of the ground reflectivity spectrum is common to both spectra. In the following, we shall refer to that as the "common band".

In the case of distributed random scatterers, there can be a correlation of the two return signals only if there is such a common band; in such a case, by considering equation 3.3, it is clear that the spectral shift Δf (the fringe frequency, of course) between the two images can be measured and, if we know the geometric parameters B_n, θ and r_o, the local terrain slope α can be recovered. Then, by integrating the local terrain slope, the terrain topography can be derived.

From equation 3.3, the expression can be easily derived of the critical baseline for which the two spectra become totally disjoint, the correlation of the two return signal goes to zero and the spectral shift cannot be computed.

$$| B_{nc} | = \frac{W r_o \lambda \tan(\theta - \alpha)}{c} \tag{3.4}$$

Then, since $W = c/(2\rho_s)$, the expression of the critical baselines can be rewritten in the following form:

$$| B_{nc} |= \frac{\lambda \cdot r_o \cdot \tan(\theta - \alpha)}{2\rho_s} \tag{3.5}$$

As an example, from equation 3.5 the ERS-1 critical baseline for flat terrain ($\alpha = 0$) can be computed:

$$| B_{nc} |= \frac{5.6 \cdot 10^{-2} \cdot 830 \cdot 10^{3} \cdot \tan(23)}{2 \cdot 9} \simeq 1100\text{meters}$$

A result similar to that found for the *monostatic* SAR (both systems are transmitting and receiving) can be demonstrated for the *bistatic* SAR case (not the ERS-1 case). In that case the stereo pair is acquired simultaneously by two sensors: the first one is equipped with a transmitter and a receiver, whereas the second one with a receiver only. It can be shown that the spectral shift induced by a baseline B_n is half that obtained in the monostatic case:

$$\Delta f = -\frac{cB_n}{2r_o\lambda\tan(\theta - \alpha)} \tag{3.6}$$

3.1 Separation of layover areas

The spectral shift between the two images given in equation 3.3 shows a dependence upon the local terrain slope along range α. As the local slope approaches the off-nadir angle the spectral shift goes to infinity and the spectra are always disjoint (blind angles). If the local slope increases again (layover) the absolute value of the spectral shift decreases, but with an opposite sign. As a consequence, negative and positive frequencies of the interferograms spectra refer to areas of layover and non layover respectively. Therefore they can be separated using selective filters provided that the slant range span of the layover slope is long enough to accommodate the indetermination principle. In figure 3.2 the spectral shift as a function of the local slope is shown in the case of ERS-1 with a baseline of 100m and a nominal off-nadir angle of 23 degrees. An example of layover separation with ERS-1 data of a mountainous area in Switzerland is shown in figure 3.3. Since layover areas can be separated from the rest of the image, slopes in the range direction from 26 to 90 degrees (together with those from -67 to 20 degrees) can be recovered by ERS-1 SAR interferometry with ground resolution dependent on slope, as usual. Moreover, by exploiting both ascending and descending ERS-1 passes, almost all the slopes from -90 to $+90$ degrees with whatever azimuth orientation are recovered. We shall come again to that in section 6.8.

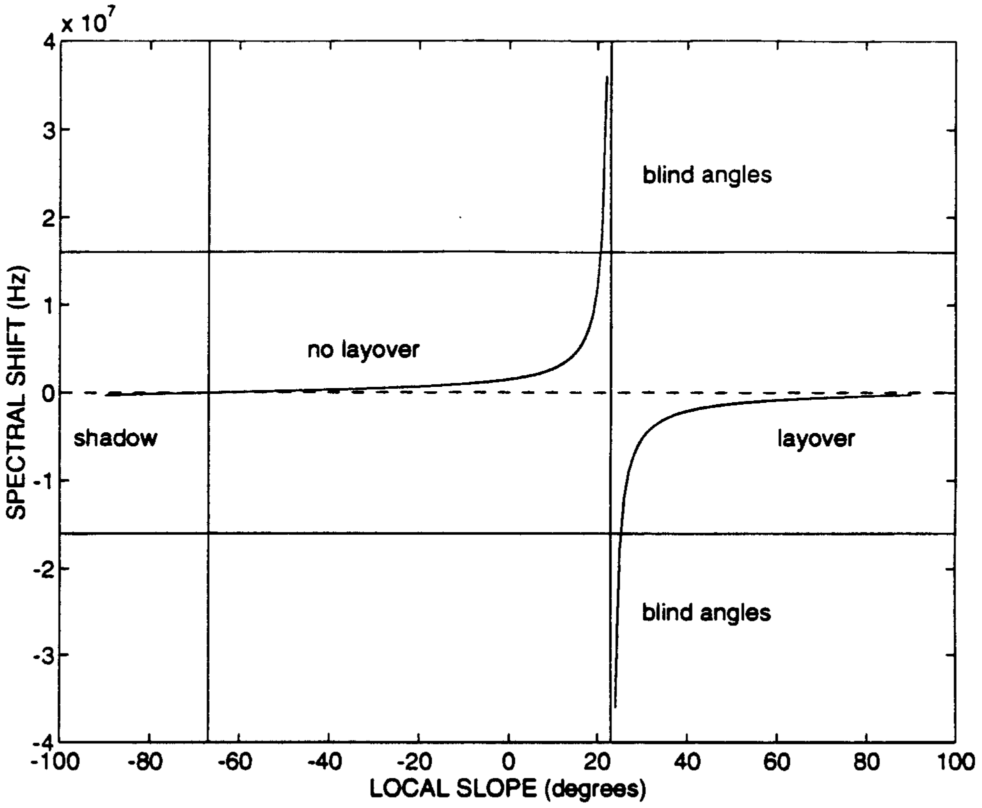

Figure 3.2: Spectral shift as a function of the local slope in the case of ERS-1 with a baseline of 100m and a nominal off-nadir angle of 23 degrees. Blind angles: from 20.76 to 25.23 degrees. The two horizontal continuous lines limit the usable spectral shift (±16MHz).

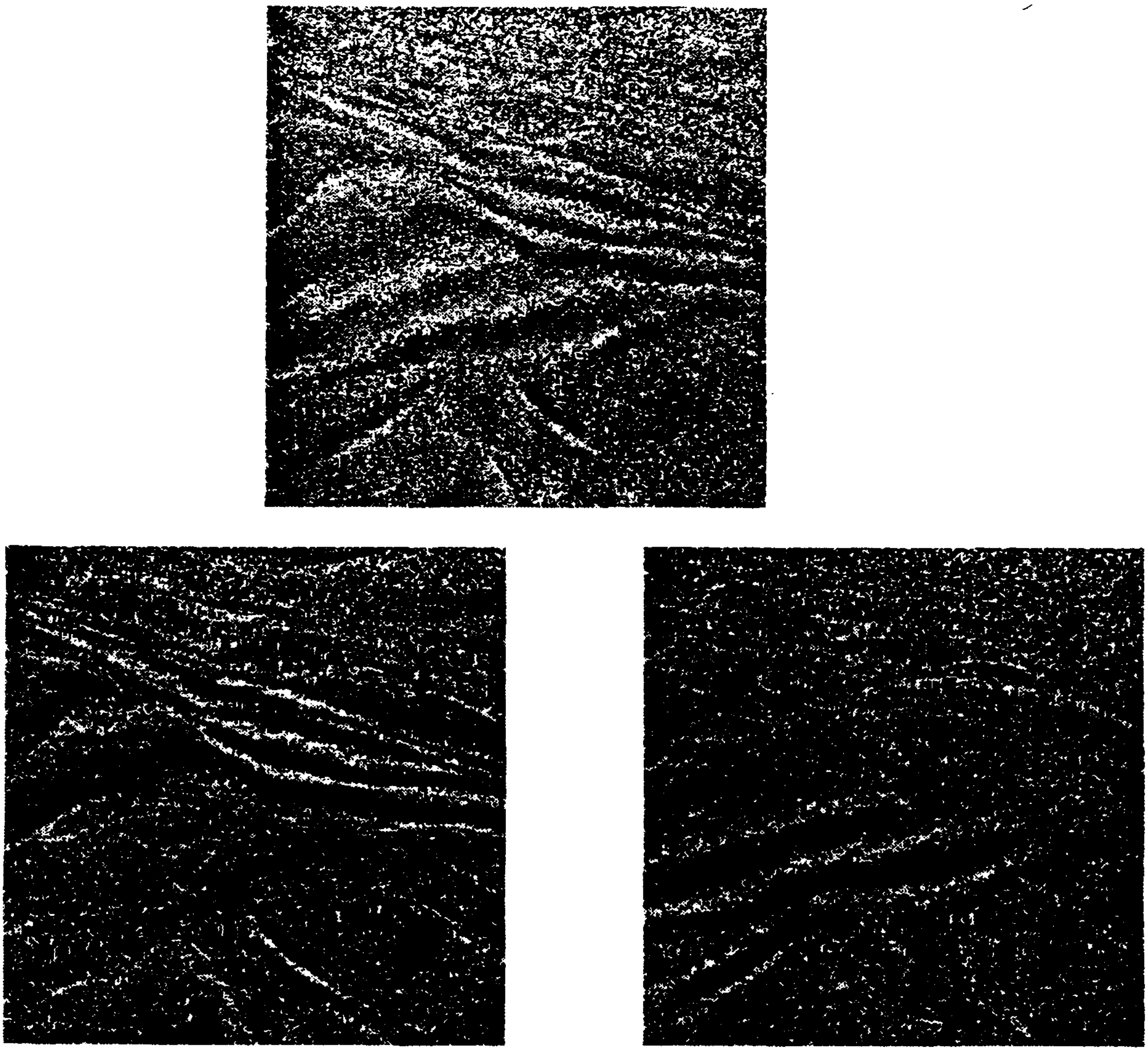

Figure 3.3: Layover separation with ERS-1 data of a mountainous area in Switzerland near Lucern. Upper: fringes. Left: fringes of non layover areas. Right: fringes of layover areas.

Chapter 4

COHERENCE OPTIMIZATION

The quality of the interferometric phase (and, as we shall see, of the measured coherence) depends on the amount of phase noise that, in general, comes from distinct sources [2, 9]:
i- system noise
ii- terrain change (non simultaneous acquisitions)
iii- images misregistration
iv- approximate and unequal focusing of the two passes
v- decorrelation due to the baseline ("geometric" decorrelation)

It is obvious that there is no way to avoid the first two sources of noise. On the other hand, as far as the last three sources are concerned, they can be taken under control.

In other words, since in the ERS-1 case the system noise is quite small compared with the usual sensed signals, it will be shown that the fringes quality can be degraded by scattering change in time and volumetric effects (see section 5.3) only.

4.1 Introduction: coherence and its degradation

The coherence γ of two complex SAR images v_1 and v_2, is defined as follows [6]:

$$\gamma = \frac{E[v_1 v_2^*]}{\sqrt{E[\mid v_1 \mid^2] E[\mid v_2 \mid^2]}} \tag{4.1}$$

where E[.] means the expectation value (that in practice will be approximated with a sampled average) and * the complex conjugate. The absolute value of γ is a fundamental information on the exploitability of SAR interferograms.

In fact, due to different causes (see section 4.3), the interferogram can be affected by noise. The signal (usable fringes) to noise ratio Ξ can be usefully expressed as a function of the coherence:

$$\Xi = \frac{\mid \gamma \mid}{1 - \mid \gamma \mid} \tag{4.2}$$

In correspondence to the absolute value of the measured coherence, that ranges between 0 (the two images are totally uncorrelated) and 1 (no change between the repeated passes or, in general, no noise), the signal to noise ratio allows the computation of the phase noise superimposed to the usable fringes.

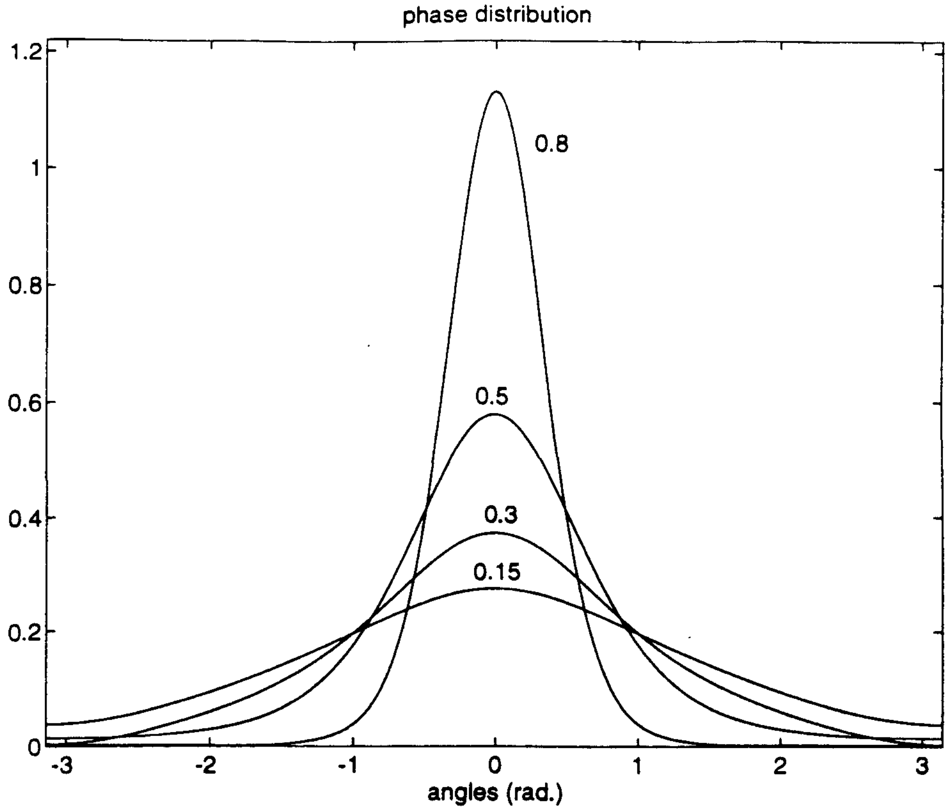

Figure 4.1: Interferometric phase distribution in correspondence to $\gamma = 0.15$, $\gamma = 0.3$, $\gamma = 0.5$ and $\gamma = 0.8$.

As an example, the interferometric phase distribution for different values of coherence ($\gamma = 0.15$, $\gamma = 0.3$, $\gamma = 0.5$ and $\gamma = 0.8$) are shown in figures 4.1.

Thus, it is clear that every effort should be dedicated to avoid coherence loss during the interferogram generation process (section 4.3).

4.2 Sampled coherence

The statistical confidence of the estimated coherence (sampled coherence) and of the derived measurements, depends on the number of indipendent samples (n) that can be combined for the computation. As a first approximation, the standard deviation of the estimator is proportional to $1/\sqrt{n}$ (see APPENDIX A). Thus, whenever statistically uniform areas are identified, the sampled coherence can be computed as:

$$\gamma = \frac{\sum_n v_1 v_2^*}{\sqrt{\sum_n \mid v_1 \mid^2 \sum_n \mid v_2 \mid^2}} \tag{4.3}$$

Furthermore, since coherence has to be estimated from the combination of the phases of a few pixels at the very least (say 16 pixels limit statistical errors to about 25%), the topography effects on the interferometric phase ϕ have to be removed from the result. This point can be easily understood by considering the ideal case where no noise is present. In such a case an unitary coherence is expected. That is, we expect that the modulus of the numerator and denominator of equation 4.3 sum to the same number. However, since the interferometric phase ϕ is proportional to the terrain slope, the numerator will be, in general, smaller than the denominator and the computed coherence γ will be smaller than one. This is evident if the numerator is regarded as the sum of vectors pointing to different directions, whereas in the denominator we have the square root of the sum of their squared moduli. Thus, in order to compensate this unwanted effect, the vectors at the numerator of equation 4.3 must be *deskewed* before summing. The following estimate of the coherence γ holds:

$$\gamma = \frac{\sum_n v_1 v_2^* e^{-j\phi}}{\sqrt{\sum_n \mid v_1 \mid^2 \sum_n \mid v_2 \mid^2}} \tag{4.4}$$

4.3 Sources of coherence degradation

4.3.1 Images registration

It is clear that, in order to generate an interferogram, the pixels of the images gathered in the two different images must be registered accurately, so that the random variates corresponding to the reflectivity are properly aligned. A single pixel shift, if the focusing processor is a good one (see section 4.3.2), should be enough to practically zero the correlation. Only the case of almost parallel trajectories will be considered in the text since it is by far the most important case in practice (SEASAT, ERS-1 and ERS-2 fall in this case). Furthermore, if crossing orbits have to be considered, we should face with a tough problem since the shift between the pixels of the images is also very dependent on their elevation [14].

When the two SAR trajectories are almost parallel the images registration can be accomplished by means of the following steps:

i - A shift in the azimuth direction.

ii - A shift in the slant range direction.

iii - An interpolation and resampling in the slant range direction of one of the two images. The different viewpoints cause a slight difference of the ground sampling rate.

iv - An interpolation and resampling in the azimuth direction of one of the two images. This step can be neglected for almost parallel trajectories and equal azimuth sampling in the two images.

v - A rotation. It can be introduced by a very slight cross angle β between the two orbits.

The relationship between the azimuth and slant range coordinates (x_1, r_1) of image v_1 and (x_2, r_2) of image v_2 is:

$$x_1 = x_2 \cos\beta - r_2 \sin\beta \tag{4.5}$$

$$r_1 = x_2 \sin\beta + r_2 \cos\beta \tag{4.6}$$

For slight cross angle we obtain:

$$x_1 \simeq x_2 - r_2\beta \tag{4.7}$$

$$r_1 \simeq x_2\beta + r_2 \tag{4.8}$$

Therefore, the rotation can be applied as a shift in the azimuth direction dependent on the slant range coordinate and a shift in the slant range direction dependent on the azimuth coordinate. Furthermore, since for ERS-1 the sampling rate in azimuth is much smaller than in range, the second shift (equation 4.8) can be neglected.

This is a simple approximation of the pixel displacement, not the exact expression; however, it can be shown [14] that the difference between the previous expression and the correct one is only slight.

To perform the registration process the value of several parameters must be known. These values can be ascertained as follows: first the rough displacement between the pixels of the two images is calculated by searching for the displacement that maximizes the cross-correlation of the two detected images. Then, a fine search can be performed on small limited areas (a few pixels in azimuth and range) seeking the displacement that maximizes the fringes contrast[1] [15] or the amplitude of the local complex coherence γ). The shifting and stretching parameters can be then fitted to the data using a LMS algorithm.

In the following it is shown that for reasonable high value of the coherence ($\gamma > .3$), the resulting registration accuracy can be as good as 1/50 of a pixel.

Using the definition of coherence given in equation 4.1 (a constant interferometric phase is assumed) it is possible to derive expressions for the coherence loss in the case of misregistration.

To make this derivation we neglect noise and exploit that the transfer function is a frequency dependent phase shift, for these two cases.

We consider only the monodimensional case. We refer to a generic x coordinate system with a sampling distance Δ.

Exploiting the Parseval theorem in equation 4.1, we obtain:

$$\gamma = \frac{\Delta}{2\pi} \frac{E[\int_{-\pi/\Delta}^{+\pi/\Delta} V_1(\omega)V_2^*(\omega)d\omega]}{\sqrt{E[\mid v_1 \mid^2]E[\mid v_2 \mid^2]}} \tag{4.9}$$

where $V_1(\omega)$ and $V_2(\omega)$ are the Fourier transforms of v_1 and v_2. If we consider the effect of misregistration and differential defocusing as a linear filter applyed to the image v_2,

$$V_1(\omega) = H(\omega)V_2(\omega) \tag{4.10}$$

equation 4.9 simplifies:

$$\gamma = \frac{\Delta}{2\pi} \frac{E[\int_{-\pi/\Delta}^{+\pi/\Delta} \mid V_2(\omega) \mid^2 H(\omega)d\omega]}{E[\mid v_2 \mid^2]} \tag{4.11}$$

---

[1] In fact, the fringe patterns appear clearly throughout the interferometrical image only if the two complex SAR images are registered properly; even the smallest of differences from the correct pixel displacement will cause the interferometrical fringes to become hazy.

In general, the spectrum of the reflectivity $V_2(\omega)$ can be considered white, obtaining:

$$E[\mid V_2(\omega)\mid^2] = \beta^2 = E[\mid v_1 \mid^2] \tag{4.12}$$

By substituting it in equation 4.11, we obtain:

$$\mid \gamma \mid = \mid \frac{\Delta}{2\pi} \int_{-\pi/\Delta}^{+\pi/\Delta} H(\omega) d\omega \mid \tag{4.13}$$

In the case of misregistration between v_1 and v_2, we have:

$$H(\omega) = e^{-j\omega\mu\Delta} \tag{4.14}$$

where μ is the residual shift in pixels between the two images. From equations 4.14 and 4.13 we obtain now:

$$\mid \gamma(\mu) \mid = \mid \frac{\sin(\pi\mu)}{\pi\mu} \mid \tag{4.15}$$

Therefore, for a misregistration of one pixel there is no more coherence between the two images.

The second member of equation 4.15 can be expanded as a Mac Laurin series, truncated at the second order, obtaining the following approximation:

$$\gamma(\mu) \simeq 1 - \frac{(\pi^2\mu^2)}{6} \tag{4.16}$$

The dispersion of the residual shift μ can be estimated as follow. In a monodimensional case, we have:

$$v_1(x + \mu\Delta) = v_1(x) + \mu\Delta\frac{dv_1}{dx} + \epsilon \tag{4.17}$$

If we consider the noise of the system as a zero mean complex Gaussian white noise with variance σ_n^2, it has been shown [17] that:

$$\sigma_{\mu\Delta}^2 = \frac{\sigma_n^2}{N\sigma_{v1'}^2} \tag{4.18}$$

where N is the number of independent data points; when $N = 2mn$, m and n are the dimensions of the window where the shift has been estimated and

$$\sigma_{v1'}^2 = E[\frac{dv_1}{dx}]^2 \tag{4.19}$$

We can derive:

$$\frac{\sigma_n^2}{\sigma_{v_1}^2} = \frac{1}{SNR} = \frac{1-\gamma}{\gamma} \tag{4.20}$$

From 4.12 we have:

$$\sigma_{v_1}^2 = R_{v_1}(0) = \frac{\Delta \int_{-\pi/\Delta}^{\pi/\Delta} \beta^2 d\omega}{2\pi} = \beta^2 \tag{4.21}$$

$$\sigma^2_{v1'} = R_{v1'}(0) = \frac{\Delta \int_{-\pi/\Delta}^{\pi/\Delta} \omega^2 \beta^2 d\omega}{2\pi} = \frac{\pi^2\beta^2}{3\Delta^2} \tag{4.22}$$

Now, by combining these equations with 4.20 we have:

$$\sigma^2_{\mu\Delta} = \frac{1-\gamma}{\gamma}\frac{3\Delta^2}{\pi^2 N} \tag{4.23}$$

$$\sigma^2_{\mu} = \frac{1-\gamma}{\gamma}\frac{3}{\pi^2 N} \tag{4.24}$$

Therefore, for an estimation window with $m = n = 64$, $\gamma = 0.3$, we have $\sigma_\mu \simeq 0.01$, that leads to an accuracy of the registration as good as 1/50 of a pixel.

4.3.2 Effects of approximate focusing

As far as SAR data focusing is concerned, we note that different precision processors have been proposed and tested with success on interferometric data. They are based on the well known *range Doppler* [10] and the more recent *wavenumber domain* schemes [11, 12]. Coherence can be exploited as a tool to evaluate the focusing quality for SAR interferometry applications.

The quality of the processor plays a fundamental role as far as the interferogram quality is concerned. In fact, processors designed to fulfil even strict requirements on detected images might not be accurate enough for SAR interferometry.

As an example, the same area (i.e. the Gennargentu ERS-1 stereo pair used as a test image within the ESA FRINGE group) has been focused with two different processors: the phase preserving $\omega - k$ [11] and a Range-Doppler processor designed for the production of detected SAR images.

The coherence maps achieved in the two cases are shown in figures 4.2 and 4.3. Histograms of the two images are shown in figures 4.4 and 4.5. The difference between the two cases is clearly visible and, as one expects, the interferogram generated with that particular Range-Doppler processor is of poor quality. Notice that the achievable interferogram quality is not a direct consequence of the particular focusing method (at least as ERS-1 data are considered), but depends on the care adopted for all the processing steps (for one, the interpolators design). In fact other processors based on the Range-Doppler architecture (e.g. the VMP processor used in ESRIN) give the same good quality shown by the $\omega - k$ processor.

4.3.3 Effects of different focusing of the two takes

A good processor design is not sufficient to get the best result. Particular care should be given to the focusing parameters selection.

In the case of different focusing between v_1 and v_2, the following differential focusing operator holds:

$$H(k_x) = \exp(-j\frac{k_x^2 \lambda z}{8\pi}) \tag{4.25}$$

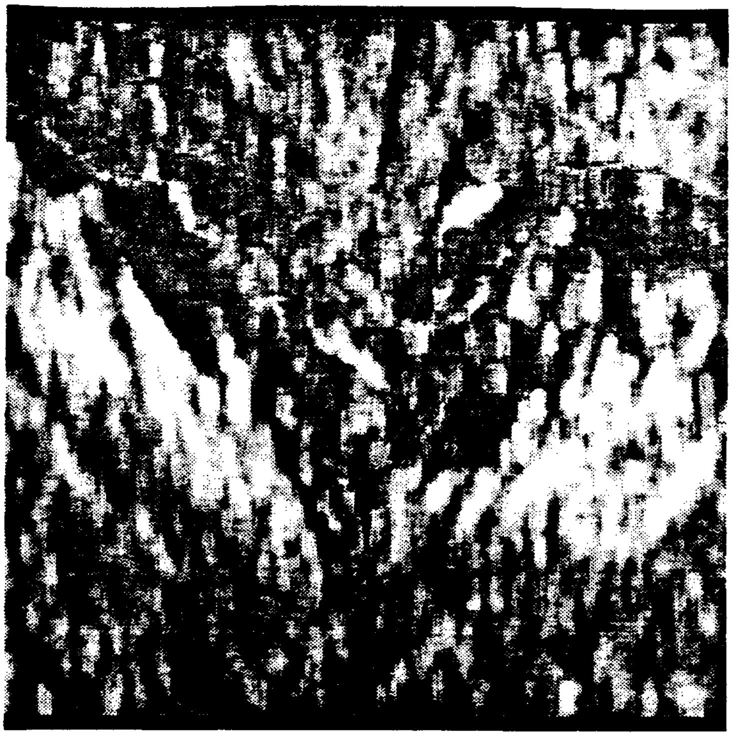

Figure 4.2: Coherence map of the Gennargentu data focused with the $\omega - k$ processor.

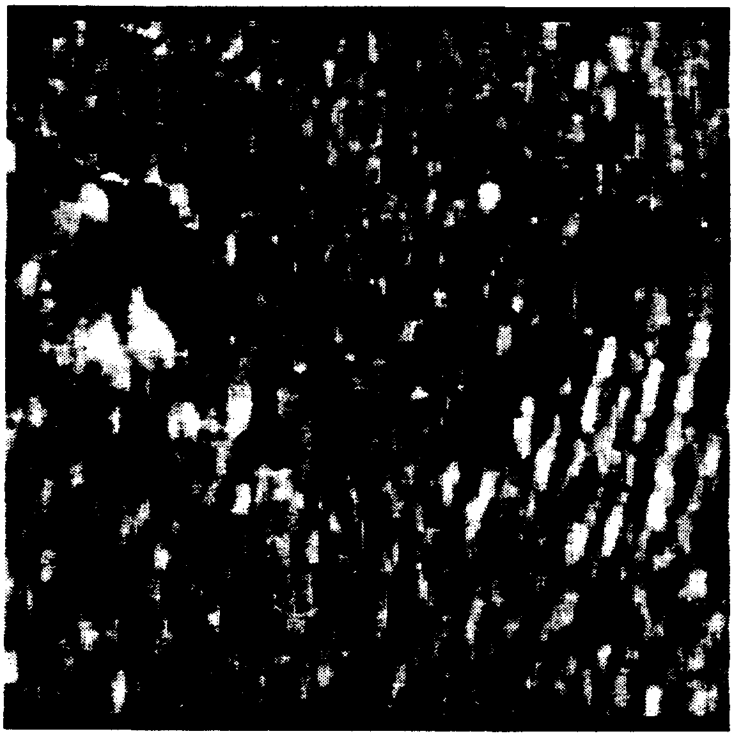

Figure 4.3: Coherence map of the Gennargentu data focused with the second processor.

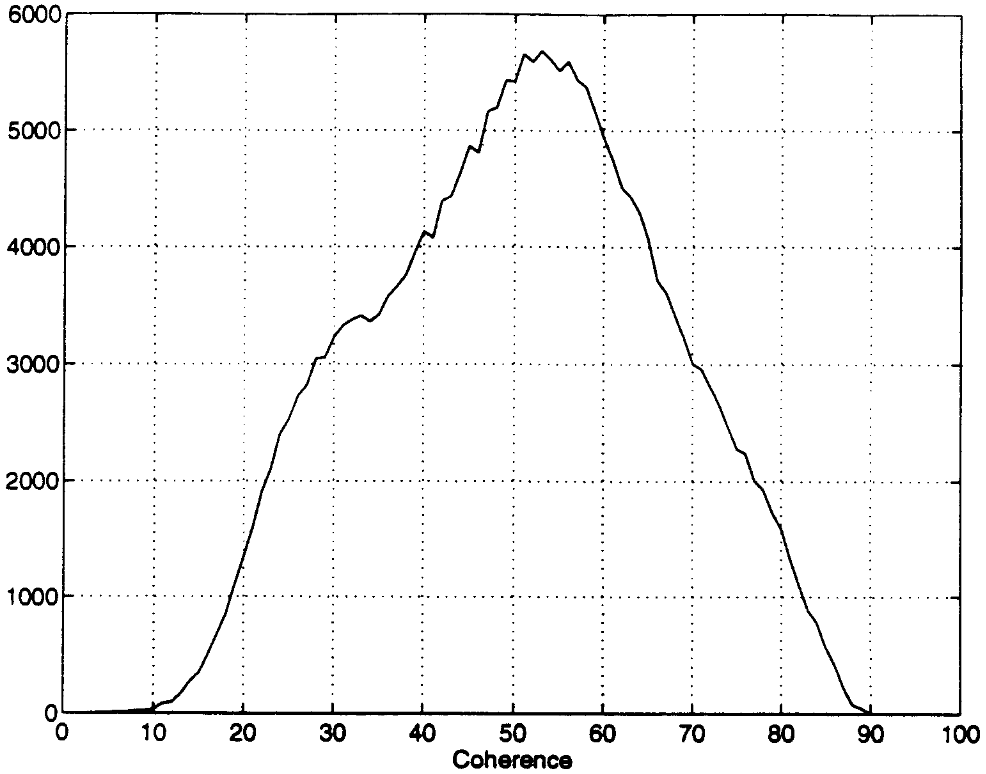

Figure 4.4: Histogram of the coherence map shown in figure 4.2.

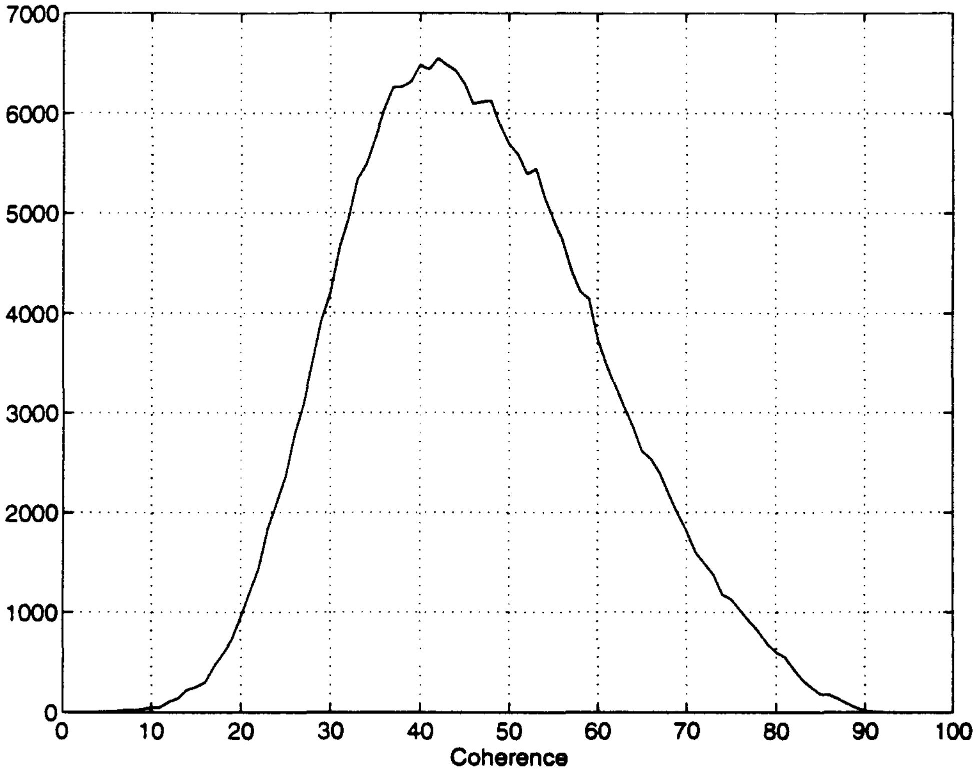

Figure 4.5: Histogram of the coherence map shown in figure 4.3.

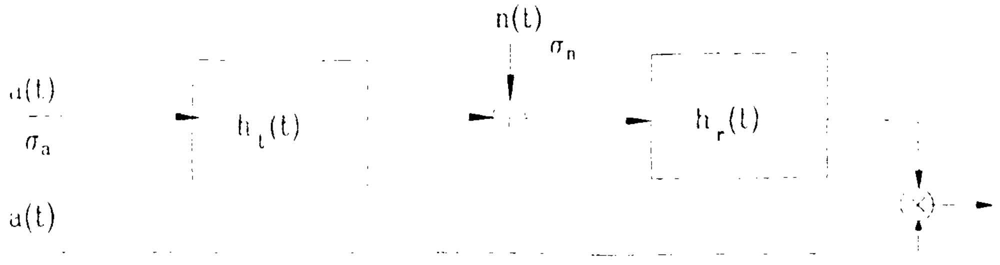

Figure 4.6: Model of the range focusing effects on the interferometric image

where k_x is the azimuth wavenumber and z is the differential error of estimation of r_0 between the two images. By substituting this equation in 4.13 we obtain:

$$\gamma = \frac{\Delta}{2\pi}\int_{-\pi/\Delta}^{+\pi/\Delta} \exp(-j\frac{k_x^2\lambda z}{8\pi})dk_x \tag{4.26}$$

By expanding the exponential term as a Mac Laurin series, truncated at the second order, we obtain:

$$\gamma = \mid 1 - j\frac{1}{3}\frac{\pi\lambda z}{8\Delta^2} - \frac{1}{10}(\frac{\pi\lambda z}{8\Delta^2})^2 \mid \tag{4.27}$$

This equation can be approximated as:

$$\gamma \simeq 1 - \frac{4}{90}(\frac{\pi\lambda z}{8\Delta^2})^2 \tag{4.28}$$

and by substituting ERS-1 values for Δ and λ we obtain:

$$\gamma \simeq 1 - 7.4\cdot 10^{-8} z^2 \tag{4.29}$$

In this case, i.e. a value of $z = 300$m generates a loss of coherence of $7\cdot 10^{-3}$, that corresponds to the effect of a misregistration of about 6/100 of a pixel.

4.3.4 Use of the chirp replica for the range focusing

The accuracy of range and azimuth focusing influences the coherence of the interferogram. These effects can be computed using the model of the interferometric SAR system, represented in figure 4.6.

This model regards only the effects of range focusing: it includes the SAR sources (that is the target reflectivity), $a(t)$; the transmitted pulse coding (usually a chirp), $h_t(t)$; the range compression filter, $h_r(t)$; a thermal noise source, $n_r(t)$, assumed uncorrelated, white; and the range-focused reflectivity, $v(t)$. All the signals are represented in the slant-range domain t.

The complex coherence can be derived, like in the previous section, by means of the definition (4.1) and by exploiting the Parseval theorem:

$$\gamma = \frac{E[\frac{1}{\Delta}\int_{-\Delta/2}^{\Delta/2} V_1(f)V_2^*(f)df]}{\sqrt{E[\mid v_1 \mid^2]E[\mid v_2 \mid^2]}} \tag{4.30}$$

The Fourier transform of the outputs, (V_1, V_2) can be derived from the model in figure 4.6:

$$\begin{aligned} V_1(f) &= (A(f) \cdot H_t(f) + N_r(f))H_r(f) \\ V_2(f) &= A(f) \end{aligned} \tag{4.31}$$

where capitals letters denote Fourier Transforms of the functions defined above. If we assume a random distributed, white target, incorrelated with the noise source, by combining expressions (4.30) (4.31) we get the coherence:

$$\gamma = \frac{\sigma_a \int_{-\Delta/2}^{\Delta/2} H_t(f) \cdot H_r(f) df}{\sqrt{\Delta \int_{-\Delta/2}^{\Delta/2} \sigma_a^2 \mid H_t(f) \mid^2 \cdot \mid H_r(f) \mid^2 + \sigma_{nr}^2 \mid H_r(f) \mid^2 df}} \tag{4.32}$$

where (σ_a, σ_{nr}) define the standard deviations of the processes $a(t), n_r(t)$.

The optimum compression filter, $H_r(f)$ is the one that maximizes the absolute value of the coherence:

$$\mid \gamma \mid^2 = \frac{\sigma_a^2 \mid \int H_t(f) \cdot H_r(f) df \mid^2}{\sigma_{nr}^2 \Delta \int_{-\Delta/2}^{\Delta/2} H_{snr}(f) \mid H_r(f) \mid^2 + \mid H_r(f) \mid^2 df} \tag{4.33}$$

In the above equation the ratio between the power spectral density of the received signal, and that of the received noise:

$$H_{snr}(f) = \frac{\sigma_a^2 \mid H_t(f) \mid^2}{\sigma_{nr}^2}$$

has been put in evidence. If this ratio is known, the value of the coherence (4.33) can be maximized to determine the optimum compression filter. We can do it, for example, for two different values of the signal to noise ratio:

1) $H_{snr} \gg 1$

2) $H_{snr} \ll 1$

In the first case (i.e. when the effect of thermal noise is negligible), the equation (4.33) can be approximated:

$$\mid \gamma \mid^2 \approx \frac{\mid \int H_t(f) \cdot H_r(f) df \mid^2}{\Delta \int \mid H_r(f) \mid^2 \cdot \mid H_t(f) \mid^2 df} \tag{4.34}$$

and the optimum filter is:

$$H_t(f) = 1/H_r(f)$$

that gives 100 % coherence.

In the second case (i.e. when the thermal noise power is comparable with the signal power), the equation (4.33) can be approximated:

$$\mid \gamma \mid^2 \approx \frac{\sigma_a^2 \mid \int H_t(f) \cdot H_r(f) df \mid^2}{\sigma_{nr}^2 \Delta \int \mid H_r(f) \mid^2 df} \tag{4.35}$$

In this case, an upper bound can be obtained by applying Schwartz inequality:

$$\mid \gamma \mid^2 \leq \frac{\mid \int H_t(f) df \mid^2 \cdot \mid \int H_r(f) df \mid^2}{(\sigma_n^2/\sigma_a^2) \Delta \int \mid H_r(f) \mid^2 df} \tag{4.36}$$

and this upper bound is reached for the matched filter:

$$H_t(f) = H_r(f)^*$$

that gives coherence:

$$|\gamma|^2 \approx \frac{\sigma_a^2/\Delta \, |\int H_r(f)df|^2}{\sigma_n^2} \qquad (4.37)$$

that is equal the noise to signal power ratio (measured after range compression).

As a conclusion, by combining expressions (4.35) and (4.37), we can conclude that the matched filter is the optimum, whatever the signal to noise ratio, when the transmitted replica has constant amplitude, as usually is. In this case the compression operator is a pure phase filter, and the absolute coherence is (see expression (4.33)):

$$\gamma = \frac{1}{\sqrt{1 + \sigma_n^2/\sigma_a^2}} \frac{1}{\Delta} \int_{-\Delta/2}^{\Delta/2} \exp(j\phi_d(f))df \qquad (4.38)$$

where $\phi_d(f)$ is the phase mismatch between the transmitted replica and the range focusing filter. It can be noted that, for constant amplitude replica (and compression filter), the input noise power input to the receiver is equal to the noise power in the compressed image, i.e. $\sigma_n = \sigma_{nr}$, and equation (4.38) gives, in the case of correct matched reference, the result found in the equation (4.2).

As an example, in the ERS-1 case, the quadratic phase coefficient of the replica should be carefully estimated. The effect of an incorrect estimate of this coefficient can be derived by a series approximation of the expression (4.38), that gives a result similar to the expression (4.28):

$$\gamma \simeq 1 - \frac{4}{9} k_2^2 \Delta^4 \qquad (4.39)$$

where the quadratic coefficient, k_2 of the replica spectrum $R(f)$, has been defined as:

$$\exp(j(k_2 f^2 + k_3 f^3 + \ldots))$$

and Δ the total bandwidth (18.96 MHz for ERS-1).

In the case of ERS-1 mission, it's subficient to evaluate the effect of second order mismatch in the reference filter, since the transmitted replica's third order contribute it's almost undectable, as figure 4.7 shows. However, the replica phase is not so stable with time to allow the use of a fixed replica for ERS-1 data: we have found in the replica contained in several ERS-1 raw data a drift of ±0.13% in the quadratic phase coefficient, with respect of its nominal value (7.52^{-12} rad/Hz^2). In this case, equation (4.39) predicts a maximum decorrelation of about 5% (noiseless case) if the nominal value is used.

The effect of departure of the replica phase from the parabolic approximation and of the variations in the spectrum amplitude have been estimated, for ERS-1, by numerically evaluating the expression (4.38). As a result, a decorrelation less than 0.5 % was computed, showing that a constant amplitude, quadratic phase replica represents a good choice for the ERS-1 case.

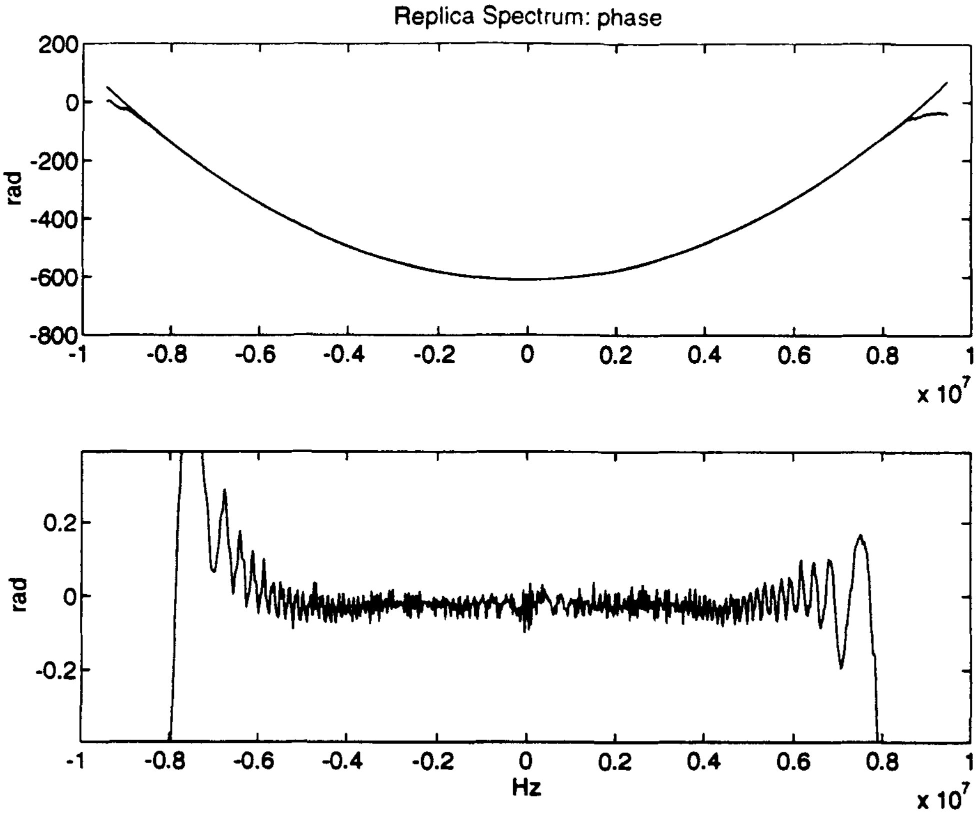

Figure 4.7: Replica phase, as a function of frequency, for the ERS-1. Above, unwrapped phase and second order polynomial fit. Below: phase error got from second order fit.

4.3.5 Suppression of the geometric decorrelation

The spectral shift principle plays an important role in the generation of the SAR interferogram to which problem this section is dedicated.

We begin with a few observation on the stochastic nature of the scattered radiation.

If we have an extended reflector, the backscattered radiation will be a random combination of the effects of all the scatterers within a resolution cell. The central limit theorem applies and the real and imaginary parts of the radar return will be Gaussian variates, independent from each other and from pixel to pixel; the variance, in general, will be space varying. The phase of the radar return will be uniformly distributed.

Therefore, in the case of an extended and spatially stationary target, the wavenumber spectrum of the reflectivity will be white, and its spectral components will be independent of each other.

In order to have a correlation of the returns in two passes, we need to illuminate the same wavenumbers of the reflectivity spectrum and therefore we need a "common band" as it was said before. Increasing the angle $\Delta\theta$, the common band will shrink and the spatial resolution of the interferogram decrease.

On the other hand, if we have a point target, the reflectivity will again be white but we lose gaussianity and therefore independence of the spectral components. These are approximately identical and the spectral shift will bear more limited effects. This means that the coherence of the point targets will be independent of the off nadir angle and this makes corner reflectors a very useful tool for registering images [24, 25]. A simpler way to arrive to the same conclusion is to remark that the spatial resolution of a corner reflector is practically unlimited, if parametric techniques are used that are aware of the nature of that specific scatterer.

If we indicate the two complex SAR images as v_1 and v_2, the interferometric phase ϕ is usually got from the phase of the product $v_1 v_2^*$, where the $*$ represents a complex conjugate. In fact $v_1 v_2^*$ is also a complex image (the interferogram) which has a phase ϕ given by the difference between the phases of v_1 and v_2.

It is well known that the sampled spectrum $R(k)$ of the sequence $v_1(n)v_2^*(n)$ is the circular cross-correlation of their sampled spectra $V_1(k)$ and $V_2(k)$. On the other hand, if the signals $v_1(n)$ and $v_2(n)$ are first interpolated by a factor of two, the interferogram's spectrum $R(k)$ is the linear cross-correlation of the two spectra $V_1(k)$ and $V_2(k)$. We consider a constant slope α for simplicity. The linear cross-correlation of the spectra shows three distinct contributions.

i - A spike at the frequency shift for which the common bands coincide (the "signal").

ii - A random sequence coming from the cross-correlation of the common bands other than in the peak position. This sequence is conjugate symmetric around the peak position and the phase of its inverse Fourier transform is linear. It cannot be considered signal; unless the symmetry is not broken by filtering the interferogram, that noise does not create disturbances.

iii - A second random sequence coming from the cross-correlation of the disjoint parts of the spectra ("noise").

As said in [6, 16, 7], it is clear that the noise contribution (iii) can be easily avoided by prefiltering the components of the two signals v_1 and v_2.

Coming to practical cases, the constant slope assumption is generally not respected and range varying filters have to be used. Their bandwidth and central frequency can be estimated from the fringes of a low quality interferogram generated without filtering.

Thus, the interferogram generation can be summarized in the following steps:

- 1 Interpolation of a factor of 2 in the slant range and azimuth directions of both the complex SAR images v_1 and v_2. This step can be accomplished by Fourier transforming the data in the slant range direction and zero padding (normally, no windowing of the spectra is required due to the presence of the on-board low-pass filter).
- 2 Registration of the images with an accuracy of at least 1/20th of a pixel.
- 3 Generation of a low quality interferogram by cross-multiplying the images v_1 and v_2^*.
- 4 Estimation of the local spectral shift $\Delta f(x,y)$ by computing the local frequency of the interferometric fringes.
- 5 Bandpass filtering of both the SAR images v_1 and v_2 accordingly to the measured $\Delta f(x,y)$.
- 6 Generation of a high quality interferogram by cross-multiplying the filtered images v_{1f} and v_{2f}^*.

Notice that a first significant improvement can be obtained if one considers that the noise, presumed white for simplicity, is present throughout the spectrum, whilst the useful signal i.e. the spectrum peak of the interferogram, is present (as always in the absence of layover) only in the half of the spectrum corresponding to the positive values of the spatial wavenumbers associated with the range (see figure 3.2).

Therefore it is convenient to eliminate half the band (and hence the power) of the noise by filtering before step 3, without touching the useful signal.

The example of figure 4.8 shows the interferogram SNR enhancement that is obtained in the ERS-1 case with a baseline of 600 meters (the still present noise is coming from other noise sources). The spatial resolution of the interferogram is reduced, but there is no reason for decorrelation.

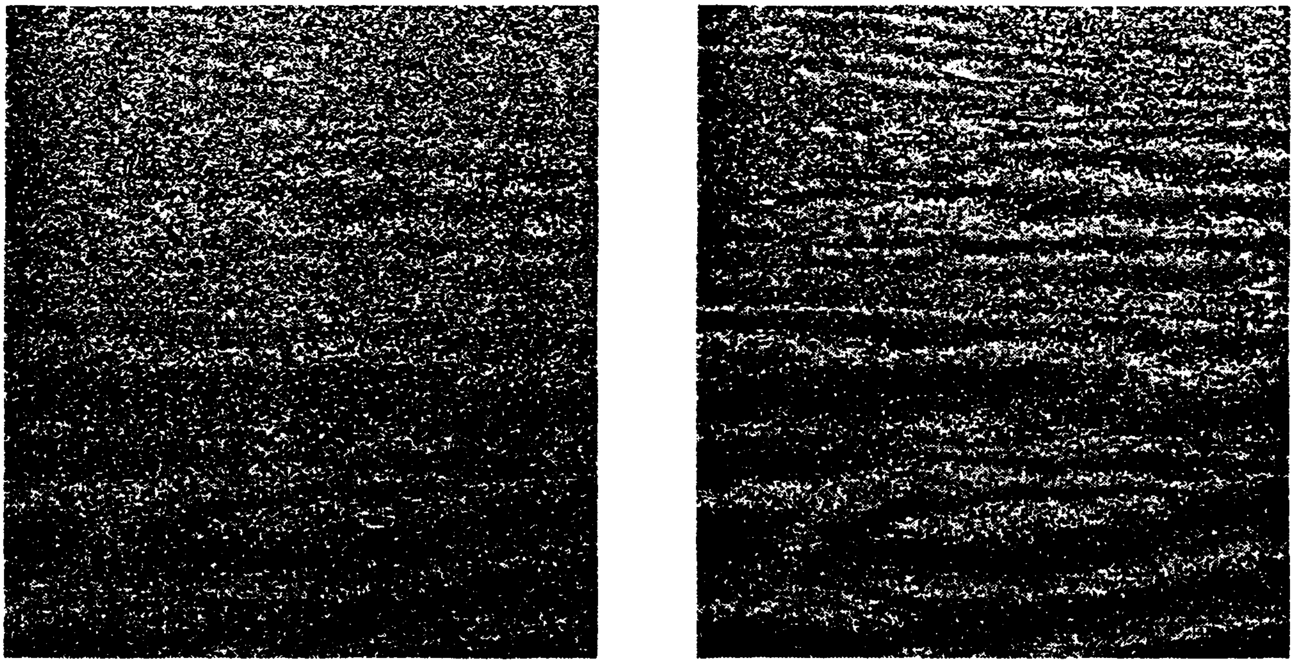

Figure 4.8: Interferogram SNR enhancement that is obtained in the ERS-1 case with a baseline of 600 meters: Bonn area.

Chapter 5

USES OF COHERENCE

In this section it is shown that SAR coherence, besides its role to achieve the best interferogram quality, is also an additional information with noticeable diagnostic power.

5.1 Estimation of the achievable elevation accuracy

The elevation error (σ_n) of maps generated by means of SAR interferometry will follow the value of $\mid \gamma \mid$ as (see equation 2.10):

$$\sigma_n = \frac{\lambda r_o \sin\theta}{2\pi n_s}\sqrt{\frac{1- \mid \gamma \mid}{2 \mid \gamma \mid}} \tag{5.1}$$

As an example, the coherence map of the area of Mt. Vesuvius in Italy observed from ERS-1 on August 27th and September 5th 1991 is shown in figure 5.1 (see also the fringes obtained with the same passes that are shown in figure 2.8).

In this example, no image segmentation has been performed. On the other hand, the sampled coherence has been computed on small rectangles 16 × 4 (azimuth, slant range) pixels large ($n = 64$) that reasonably belong to uniform areas.

By exploiting equation 5.1, the coherence map of figure 5.1 can be converted into an elevation error map (apart from systematic errors). If the ERS-1 parameters of that ERS-1 stereo pair are used, the correspondent coherence/elevation errors curve is shown in figure 5.2.

As expected, areas covered by thick vegetation (on the left side of Mt. Vesuvius) or water (the Tirrenian sea on the image bottom) or where foreshortening is close to the blind angle region (see figure 3.2) show an almost zero coherence and are not usable for SAR interferometric applications (e.g. DEM generation and super-resolution).

5.2 Hints for images segmentation

In this section a few examples are presented showing that coherence images can be exploited for images segmentation and identification of geological features. Of course, a definitive answer on the value of the coherence as an investigation tool could come only from a comparison of these maps with other information available to experts in the particular field of application.

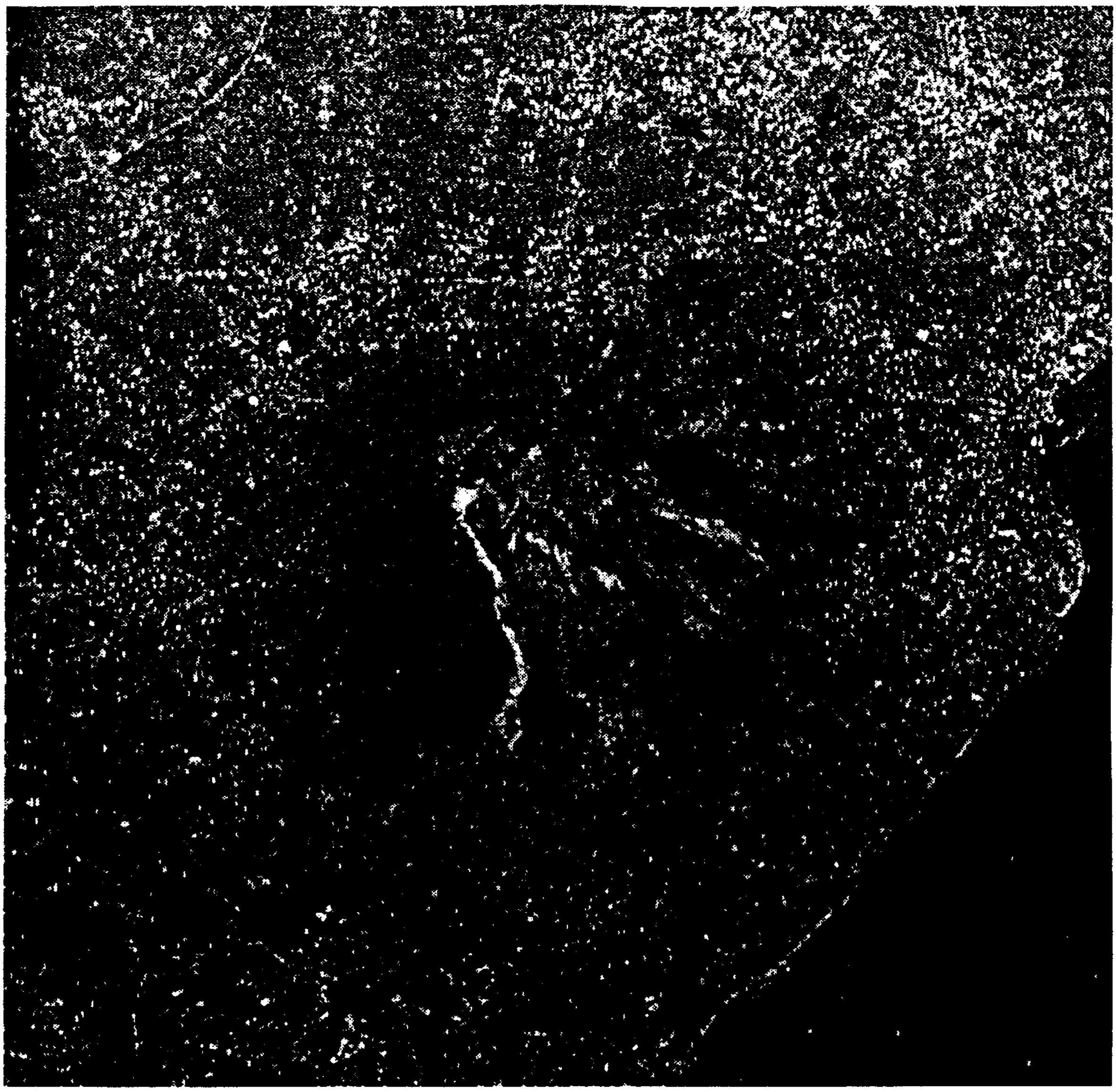

Figure 5.1: ERS-1 descending orbits - Mt. Vesuvius (Italy) August 27th and September 5th, 1991. - Coherence map.

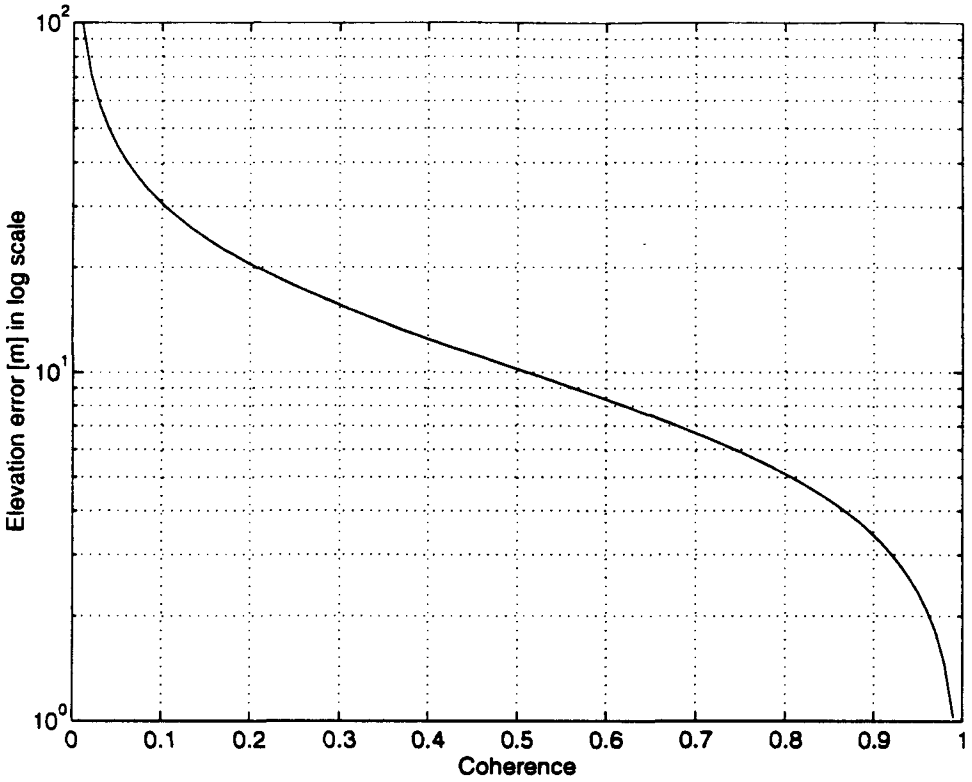

Figure 5.2: ERS-1 descending orbits - Mt. Vesuvius (Italy) August 27th and September 5th, 1991. - Elevation errors versus coherence.

- Identification of exposed rocks

The coherence image of Mt. Vesuvius (figure 5.1), shows interesting features that are not visible in the detected image of the same area (5.3).

Apart from the already mentioned zero-coherence areas, a very bright stripe (high coherence) is visible on the left hand side of Mt. Vesuvius. This area that is not identified on the absolute value image, has a geological peculiarity: it is an old lava flow (year 1944). Since exposed rocks are coherent even after many days, such areas can be easily identified by using SAR coherence. The same lava flow is visible on the coherence map of figure 5.4 (and it is not on the detected image of figure 5.5) generated from the ascending ERS-1 stereo pair taken 35 days apart on 21 March and 25 April 1993.

A further example is shown in figures 5.7 and 5.6. Here the coherence map and detected images of Mt. Etna in Sicily is shown. Again old lava flows are clearly visible on the coherence image and they are not on the detected one.

At the moment, a group of researchers at the Institute du Physique du Globe in Paris is working on the coherence image of Mt. Etna. Their first impression is that many geological features are clearly resembled in that map. Furthermore they noted that an unexplained loss of coherence is visible in one region where such a behaviour was not expected. Investigations are in progress.

- Ice dynamics studies

Coherence has been proposed as a qualitative tool for studies on ice dynamics [20]. A high level of coherence corrensponds to a near constant state of the surface and to a slow ice motion; a total lack of coherence has been shown to correnspond to superficial movements.

On the other hand, accumulation of cold snow without compactness is thought to generate only a slight lowering of the coherence, in the hypothesis of a high degree of transparency.

- Anthropogenic features and water basins identification

Another interesting example is represented by the coherence map achieved from two ERS-1 images of Bahia Bustamante along the coast of Patagonia (Argentina) taken more than 5 months apart in time (February 23rd and August 8th 1993). (SLC data have been kindly supplied by dr. H. Schwan - Freiburg University.)

The detected image, coherence map and fringes are shown in figures 5.8, 5.10 and 5.9. Notice that the average coherence even after such along time interval is high enough to allow the generation of meaningful fringes. Moreover, interesting details become visible on the coherence map only. Notice, for example, the black line (low coherence) that forms a neat angle in the upper right part of figure 5.10 (a clearly anthropogenic feature). Also notice how water basins and sea become well defined (low coherence).

- Vegetated areas identification

Finally the coherence map, achieved from interferometric quick-look processing, generated from two ERS-1 images of the Bonn area taken 3 days apart in time (March 23rd and March 26th 1992) is shown in figure 5.13. Notice the black curve (low coherence) that corresponds to Rhein river in the lower part of figure 5.13. For comparison, also the detected image and fringes are shown in figures 5.11 and 5.12. In figure 5.14 the histogram of coherence map of figure 5.13 is presented. The peak at coherence 0.225 corrensponds to vegetated and layover areas.

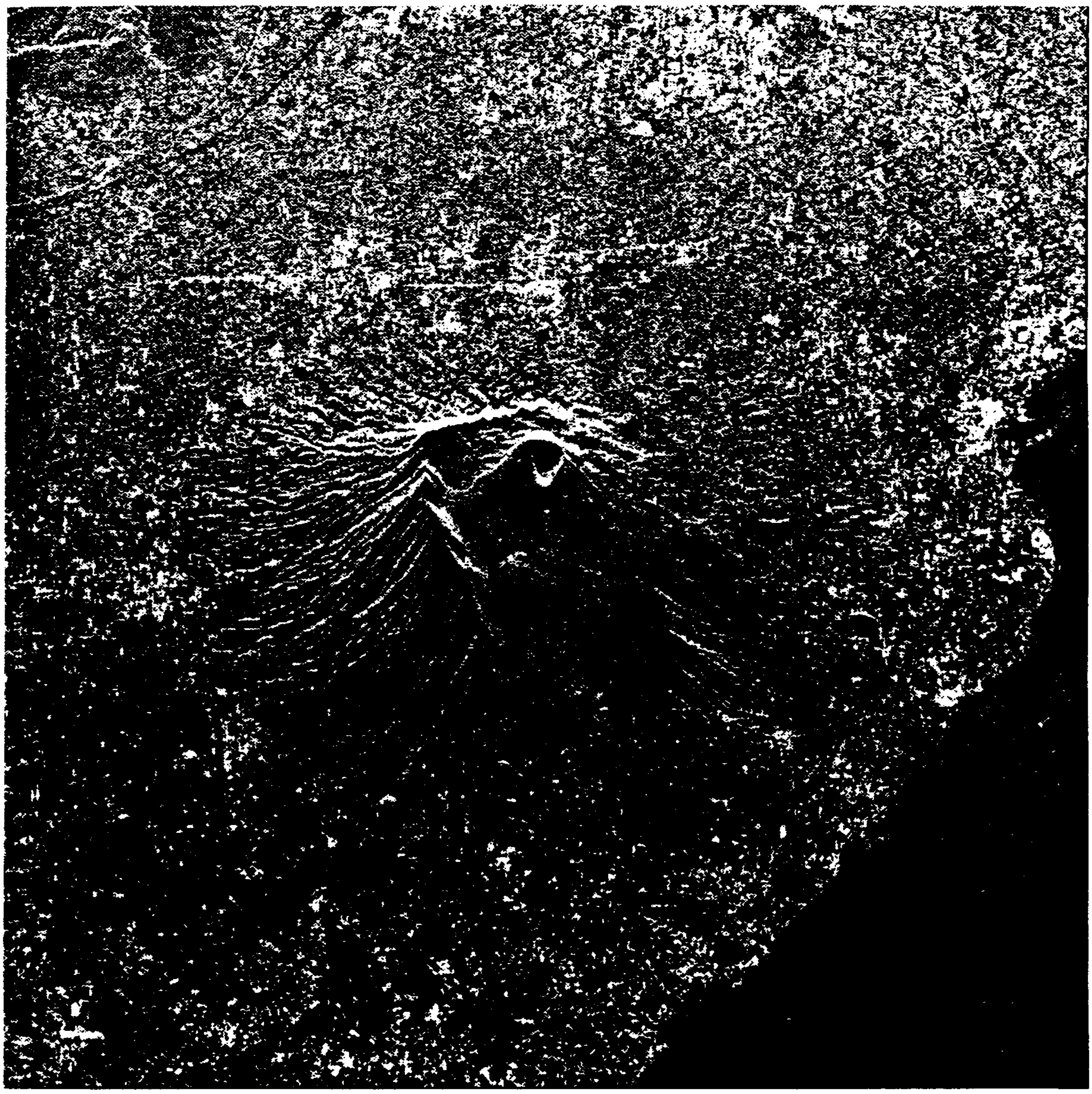

Figure 5.3: ERS-1 descending orbit - Mt. Vesuvius (Italy) August 27th and September 5th, 1991. - Detected image.

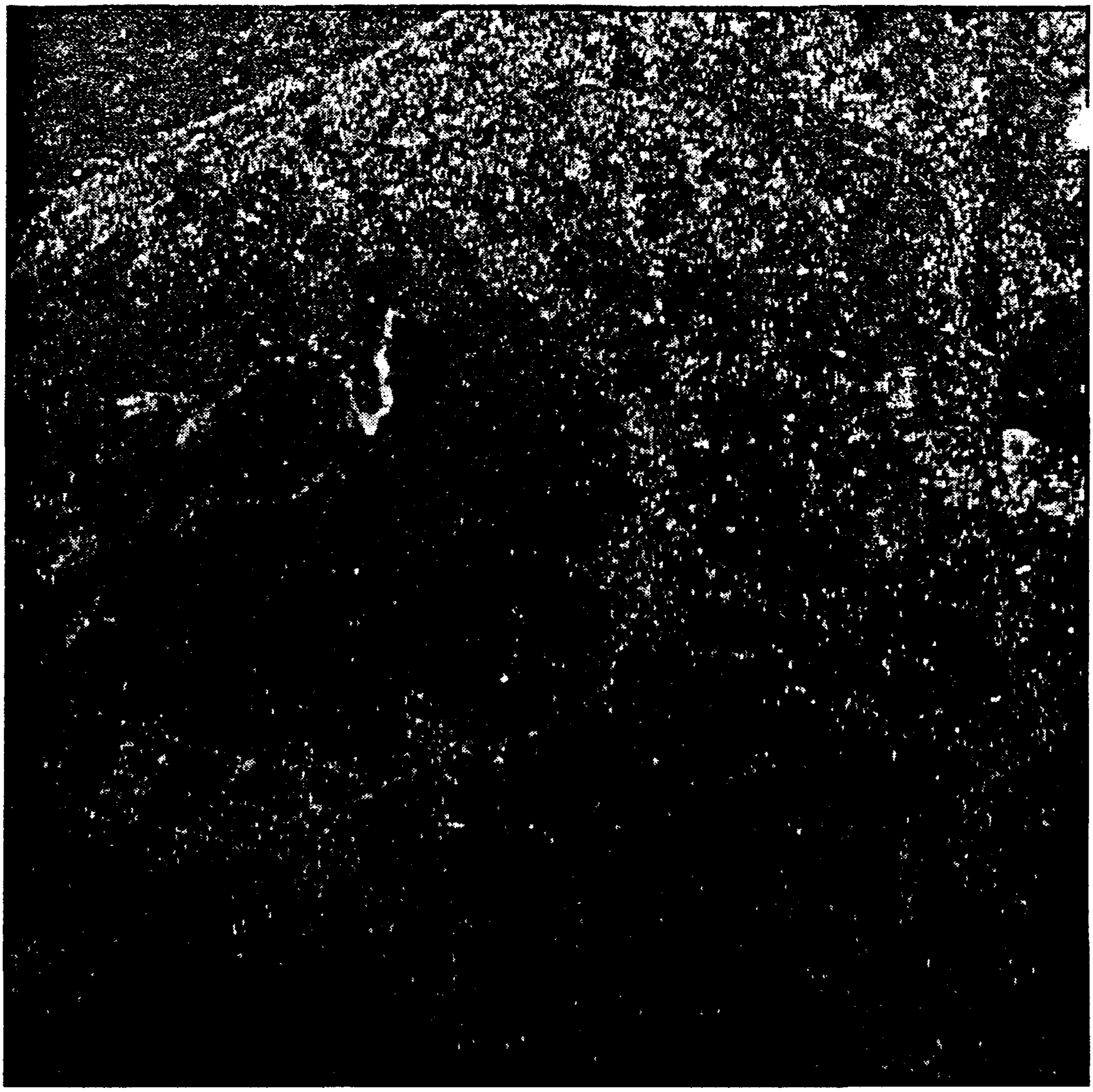

Figure 5.4: ERS-1 ascending orbits - Mt. Vesuvius (Italy) March 21st and April 25th, 1993. - Coherence map.

Figure 5.5: ERS-1 ascending orbits - Mt. Vesuvius (Italy) March 21st and April 25th, 1993. - Detected image.

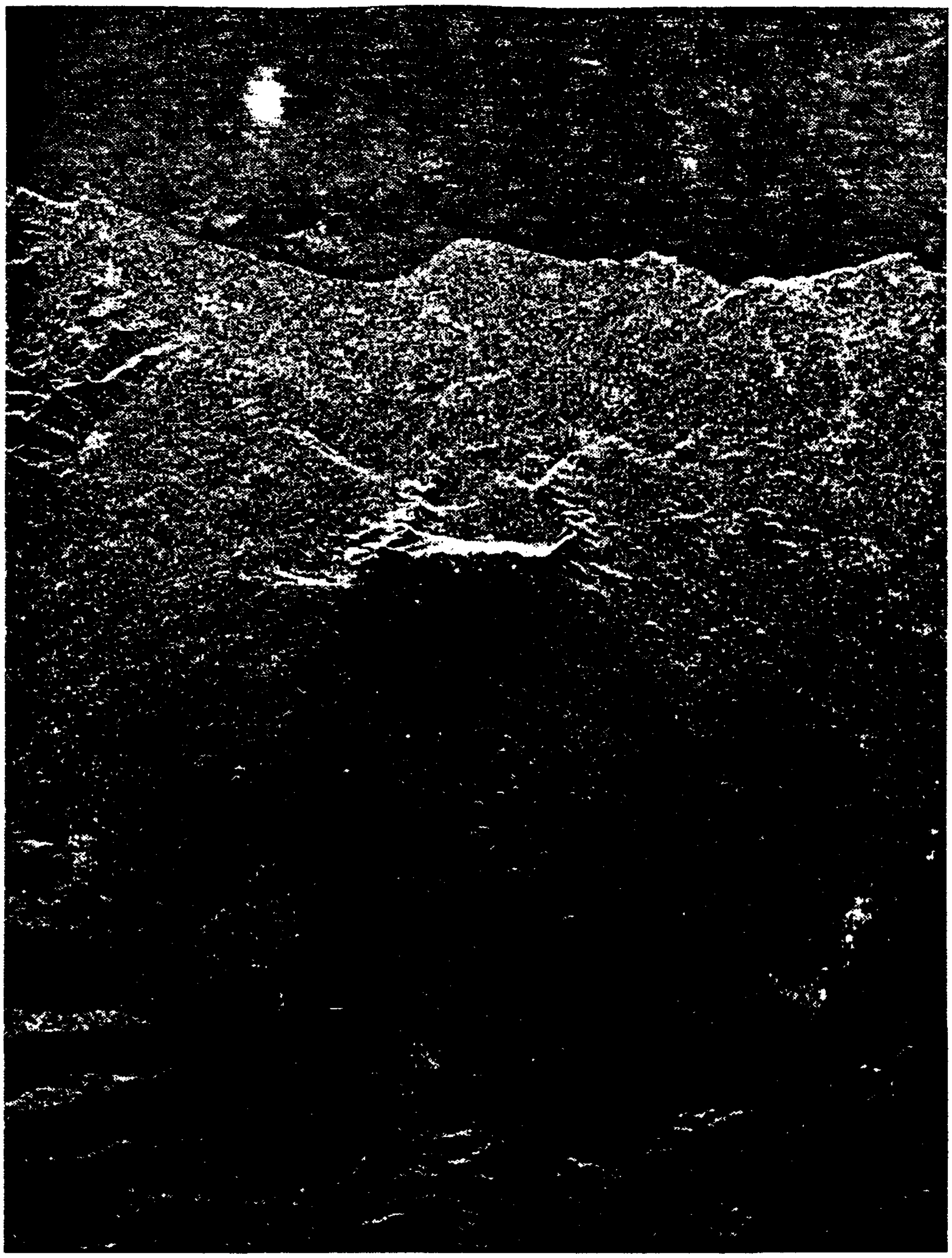

Figure 5.6: ERS-1 descending orbits - Mt. Etna (Italy) August 27th and September 5th, 1991. - Detected image.

Figure 5.7: ERS-1 descending orbits - Mt. Etna (Italy) August 27th and September 5th, 1991. - Coherence map.

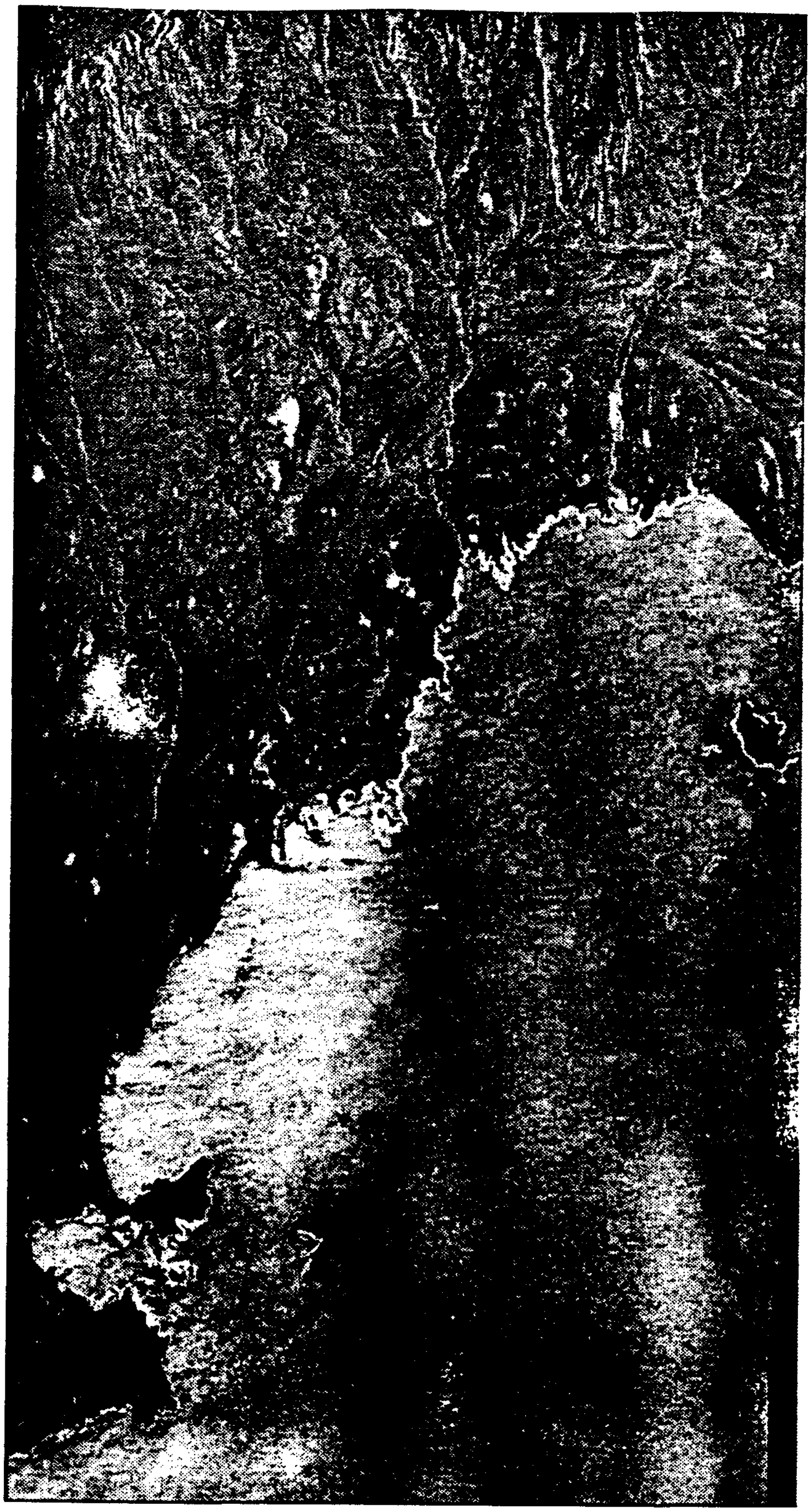

Figure 5.8: ERS-1 SAR. Detected image of Bahia Bustamante along the coast of Patagonia (Argentina). Dimensions: 75km in range (horizontal), 142km in azimuth.

Figure 5.9: ERS-1 SAR interferometry. Interferometric fringes of Bahia Bustamante along the coast of Patagonia (Argentina). The baseline is about 120 meters.

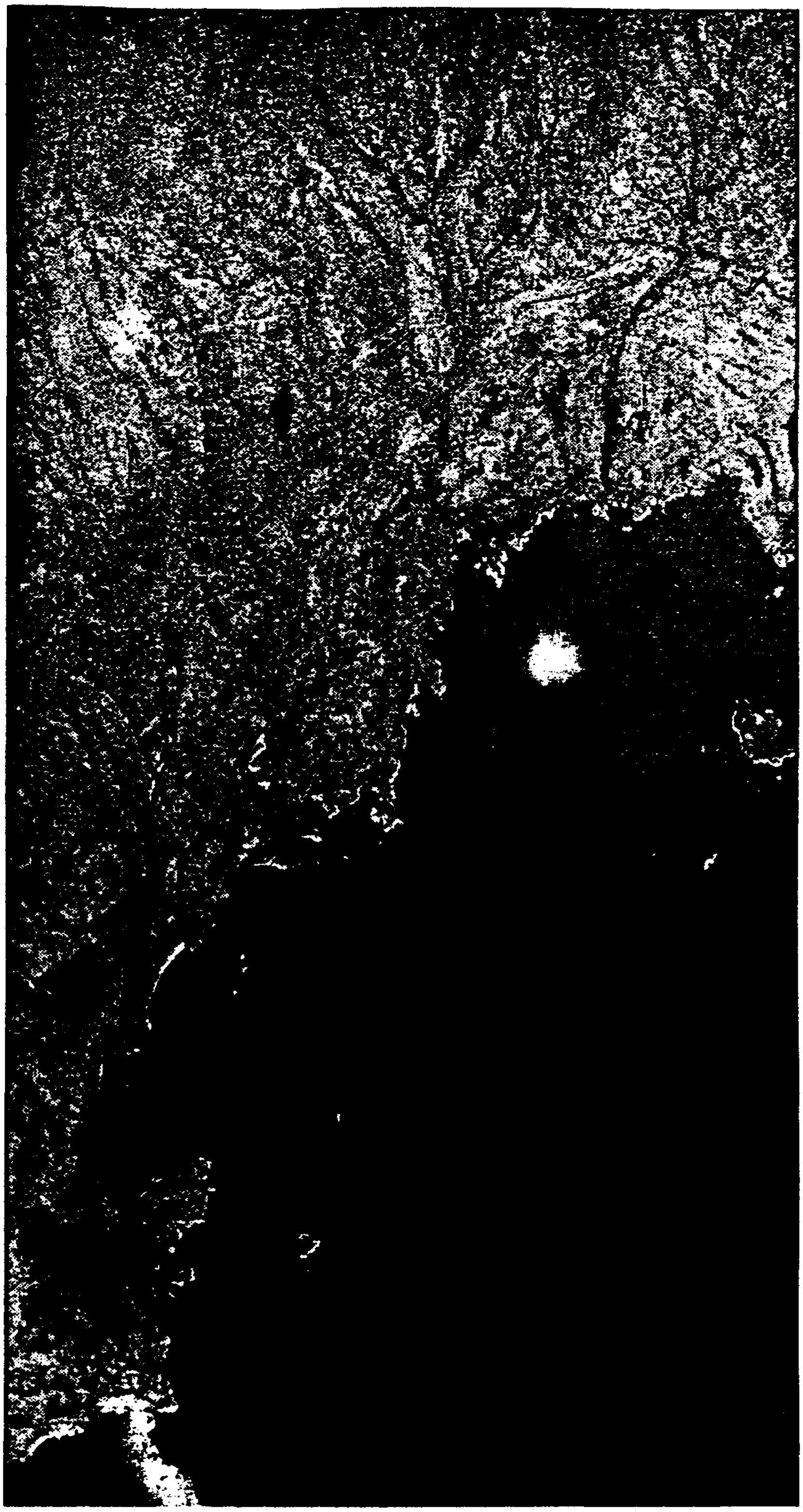

Figure 5.10: ERS-1 SAR interferometry. Coherence image of Bahia Bustamante along the coast of Patagonia (Argentina). Images taken more than 5 months apart in time (February 23rd and August 8th 1993).

Figure 5.11: ERS-1 SAR. Detected image of Bonn area (Germany). Dimensions: 80km in range (vertical), 40km in azimuth.

Figure 5.12: ERS-1 SAR interferometric quick-look. Interferometric fringes of Bonn area (Germany). The baseline is about 200 meters.

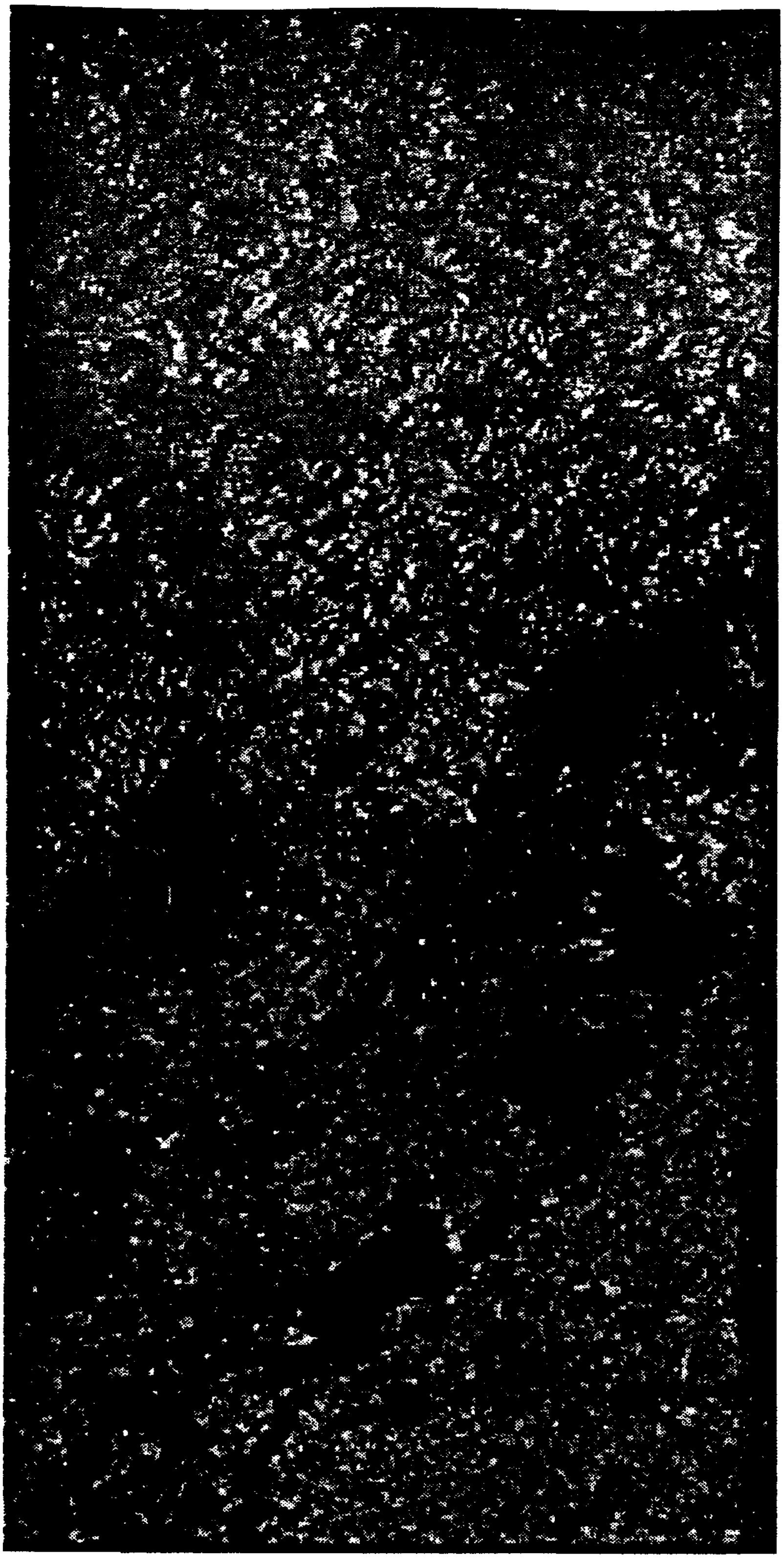

Figure 5.13: ERS-1 SAR interferometry. Coherence image of Bonn area (Germany). Images taken 3 days apart in time (March 8th and March 11th 1992).

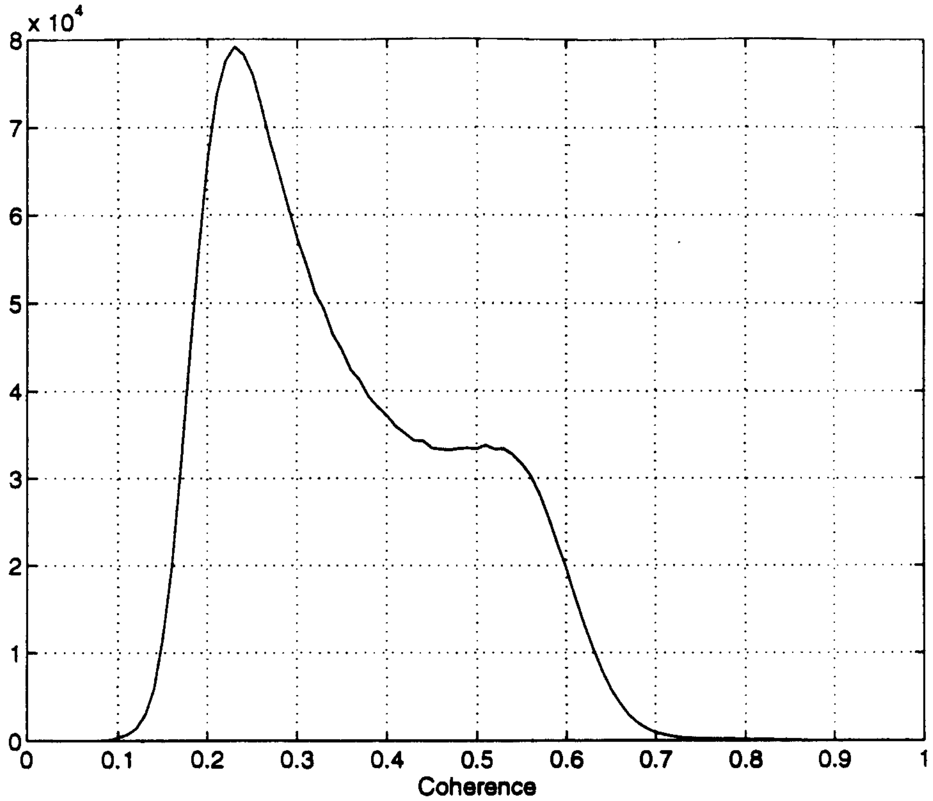

Figure 5.14: Histogram of coherence image of Bonn area (Germany).

5.3 Identification of volume scattering

Up to now, we have considered only surface scattering, neglecting the effect of volume scattering [9, 4]. However, when backscattering comes from targets with different elevation z within the resolution cell, volume effects cannot be ignored.

This case is shown in figure 5.15.a: the scatterers are contained in a box with dimensions $(\Delta y, \Delta z)$, (the problem can be assumed to be invariant with respect to the azimuth direction). The radar return is function of the complex reflectivity $a(y,z)$, the radio frequency $\omega = 2\pi f$, and the looking angle, θ:

$$A(\omega,\theta) = \iint a(y,z)\exp(-j\frac{2\omega}{c}(y\sin\theta - z\cos\theta))dydz \tag{5.2}$$

We consider the medium as semitransparent, in the usual first Born approximation, so that the scattered signal is a linear superposition of effects. Wavenumbers in ground range k_y and now in elevation too k_z have the following form:

$$\begin{aligned} \mid k_y \mid &= \frac{2\omega}{c}\sin\theta \\ \mid k_z \mid &= \frac{2\omega}{c}\cos\theta \end{aligned} \tag{5.3}$$

The following expression of the received signal holds:

$$A(k_y,k_z) = \iint a(y,z)\exp(-j(k_y y + k_z z))dydz \tag{5.4}$$

Thus, the received signal can be regarded as the 2D Fourier transform of the ground reflectivity measured at the wavenumbers given by equation 5.3.

Two SAR images from different angles (θ and $\theta + \Delta\theta$) represent different bands of the complex reflectivity spectrum. From figure 5.15, it is clear that, in order to observe the same k_y from the two acquisitions (i.e. the condition that allows coherent interferometry in case of surface scattering), the looking angle change $\Delta\theta$ should be compensated by the spectral shift $\Delta\omega = -\omega\Delta\theta/\tan(\theta)$ that is equivalent to the following k_z wavenumber shift
$\Delta k_z \simeq -2\Delta\omega/(c\cos\theta) = 2\omega\Delta\theta/(c\sin\theta)$.

The coherence of interferometric images depends on the degree of spectral correlation between the measurements in k_z and $k_z + \Delta k_z$. If we consider, as a special case, the flat box ($\Delta z = 0$), the signal is impulsive in the z domain and we have total correlation of the different spectral components and unitary coherence. In general, with a finite volume and a non zero value of Δz, we shall have the following expression of the spectral correlation function:

$$\frac{\sin(\Delta k_z \Delta z/2)}{\Delta k_z \Delta z/2}$$

So, we can state that whenever $\mid \Delta z \mid \ll 2\pi / \mid \Delta k_z \mid$, volumetric effects can be neglected. A useful expression can be found as a function of transmitted wavelength, normal baseline and satellite altitude:

$$\mid \Delta z \mid \ll \mid \frac{\lambda H \tan\theta}{2B_n} \mid = \mid \Delta z_o \mid \tag{5.5}$$

If we consider the case of $|\Delta z| \geq |\Delta z_o|$, we have spectral decorrelation and low coherence. In the ERS-1 case with a baseline of 250 meters decorrelation is expected for $|\Delta z| \geq 38$meters.

On the other hand, one might claim that this is not decorrelation but signal. One could reasonably consider usable the change of the two SAR images as a function of the baseline (difference of the complex samples) as signal.

For the sake of simplicity let us use the following approximation:

$$A(k_y, k_z + \Delta k_z) \simeq A(k_y, k_z) + \frac{\partial A}{\partial k_z} \cdot \Delta k_z =$$

$$= A(k_y, k_z) - \frac{j2\omega\Delta\theta}{c\sin\theta} \iint z \quad a(y,z)\exp(-j(k_y y + k_z z))dydz =$$

$$= A(k_y, k_z) - \frac{j4\pi B_n}{H\lambda\tan\theta} V(k_y, k_z) \tag{5.6}$$

Here, $V(k_y, k_z)$ is the result of the double integral. Thus, if we have many interferometric observations with different baseline, we can split each observation $A_i(k_y, k_z)$ into a "surface contribution" $A(k_y, k_z)$ and a "volumetric contribution" proportional to the baseline; this term is proportional to the moment of the reflectivity along the z axis.

$$A_i(k_y, k_z) = A(k_y, k_z) - \frac{j4\pi B_n}{H\lambda\tan\theta} V(k_y, k_z) \tag{5.7}$$

From those observations, it is then possible to derive a LMS estimate of the surface and the volumetric contribution. As an example, six ERS-1 images of the area of Bonn have been exploited for this goal after registration in space and frequency. The estimated surface and volumetric contributions are shown in figure 5.16.

They are not represented with the same scale since the average amplitude of the surface contribution is roughly 20 times that of the volumetric one. No definitive conclusions have been derived from this example, yet. For one, it can be noted that the volumetric contribution shows side lobes extended in the range direction (vertical in the image). This feature comes from side lobes of strong point scatterers laying on adjacent range bins. Due to the spectral shift compensation, the sidelobes are phase shifted with respect to the main lobe, proportionally both to the baseline and to their distance from the main lobe. Hence, they tend to be cancelled from the surface contribution. Less so from the volumetric contribution, as far as the linear dephasing approximates a linear change proportional to the baseline. Different results could be obtained by regressing with the baseline phase and modulus instead of real and imaginary parts as it has been done in this example. These concepts have been checked with synthetic examples not reported here for brevity and could be further tested by means of controlled experiments (e.g. by exploiting the new anechoic chamber available at JRC-EMSL [5]).

Furthermore, we notice that if the volumetric contribution is subtracted from the images, their coherence increases. This effect is shown in figure 5.17. Here histograms of coherence between two ERS-1 images of Bonn are plotted. The first one has been derived from the original images; the second, after subtraction of the volumetric effect. Their difference is shown in figure 5.17. Please notice that about 25% of the pixels have been moved from lower to higher coherence. However, it should be noted that such a big coherence improvement is only partly due to volume effects subtraction. In fact, volume estimation is affected by temporal changes T_i with respect to the

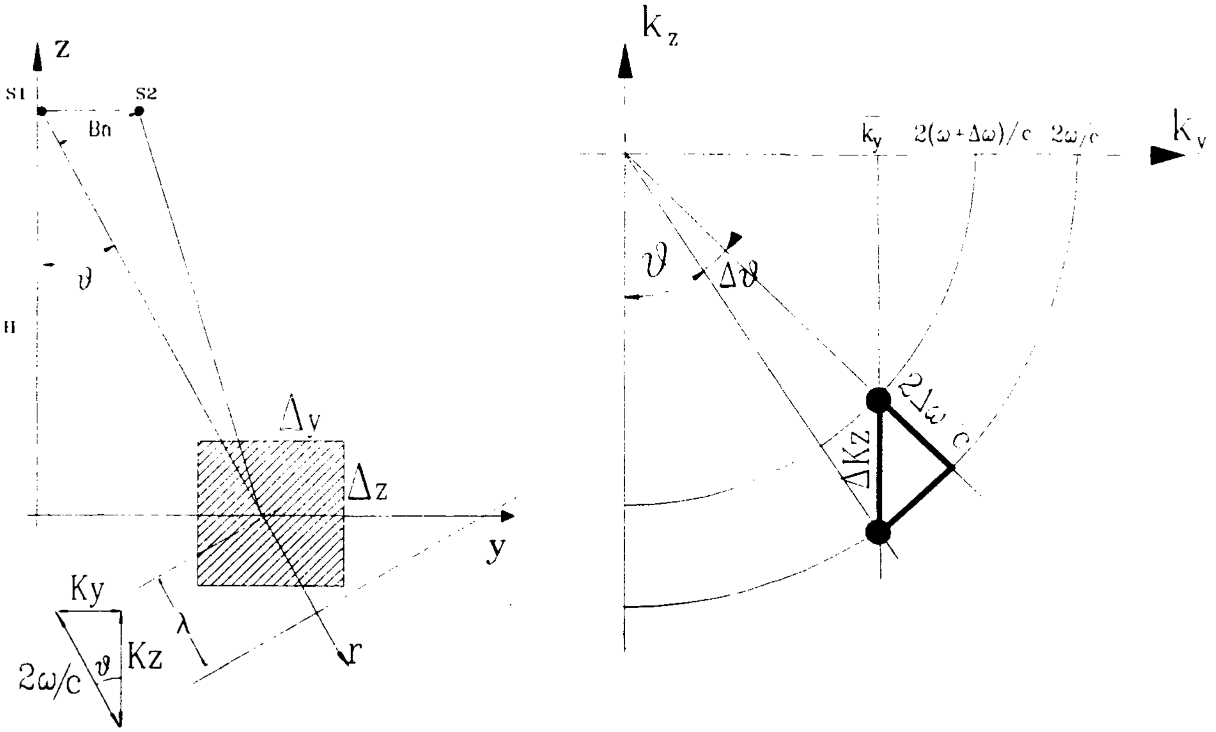

Figure 5.15: Volumetric scattering. Left: geometry. Right: wavenumbers representation.

reference (time independent) image $A(k_y, k_z)$. The actual model we have to face with is, thus, the following:

$$A_i(k_y, k_z) = A(k_y, k_z) + T_i - j\Gamma_i \cdot V_1 - \ldots \tag{5.8}$$

The LMS estimate of A and V_1 is derived from the minimization of the following expression with respect to A and V_1:

$$E\left[(A_i(k_y, k_z) - A(k_y, k_z) + j\Gamma_i \cdot V_1)^2\right] = E\left[(T_i)^2\right]$$

It is then clear that if just a few images are available, part of the temporal change component will contaminate the volumetric estimate. This estimation technique appears to be reliable on areas where temporal changes are not relevant.

Figure 5.16: Volume scattering. Six ERS-1 images (area of Bonn) have been processed to separate surface and volumetric contributions. Left: one of the six images. Middle: estimate of the surface contribution. Right: Estimate of the volumetric contribution. Image size: 1 km, azimuth (horizontal) x 2 km, range (vertical).

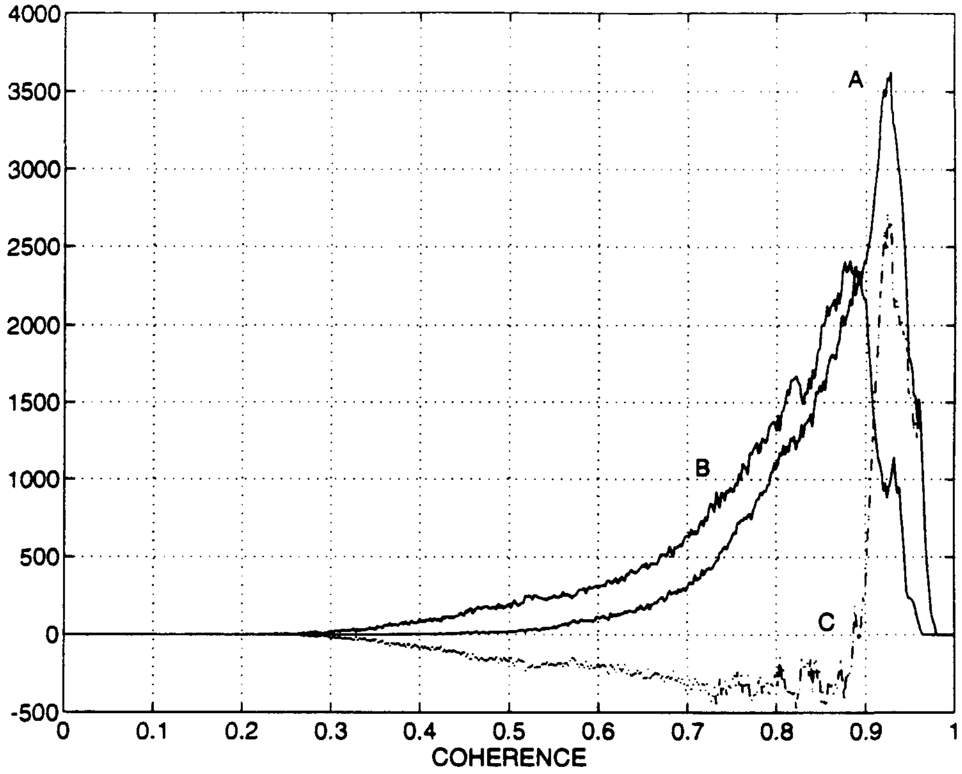

Figure 5.17: Coherence before and after volumetric effects subtraction. A: coherence histogram after volumetric effects subtraction. B: coherence histogram of the original images. C: histogram difference.

Chapter 6

PHASE UNWRAPPING

In section 2.3 we have noted that the real phase values are " wrapped" around a 2π interval and that they can be derived by unwrapping the principal phase values (interferometric fringes).

Phase unwrapping is one of the most delicate steps in the generation of elevation maps using SAR interferometry. It becomes a particularly tough problem for low phase to noise ratioes (low coherence).

Thus, before going into a detailed description of phase unwrapping techniques, it is worth to derive methods to improve the signal to noise ratio at the cost of a reduction of the interferogram spatial resolution.

6.1 Estimation of the phase of the interferogram

Let us first consider the case of a constant interferometric phase corrupted by noise (the general case will be developed in the next section). For areas that can be considered statistically uniform, we derive the Maximum Likelihood estimate of the interferometric phase ϕ.

The phase of the products of the two images v_i's is corrupted by noise.

$$v_i = \rho_i e^{j\phi} + n_i \qquad\qquad i = 1, 2, ..., N \tag{6.1}$$

If we suppose that the amplitudes ρ_i are known, the best estimation, in the least mean square sense, of ϕ can be found as:

$$\hat{\phi} = \arg\left(\frac{1}{N}\sum_{i=1}^{N}\rho_i v_i\right) \tag{6.2}$$

Thus, the best phase estimate is the phase of the average of the complex pixels, weighted by their known amplitude ρ_i. In practice, however, the pixel's amplitude is unknown and it can only be described by its probability density that, assuming the terrain reflectivity to be a complex Gaussian random variate, is Laplacian:

$$p(\rho) = \frac{e^{\frac{-\rho}{\rho_m}}}{\rho_m} \quad , \tag{6.3}$$

where ρ_m represents the expected value of ρ.

Noise is present separately in each image:

$$v_1 = \sqrt{\rho} + n_1 \quad (6.4)$$
$$v_2 = \sqrt{\rho}e^{j\phi} + n_2 \quad (6.5)$$
$$(6.6)$$

It is reasonable to consider n_1 and n_2 as complex Gaussian white noises with the same variance σ_0^2.

If we compute the product $V = v_1 v_2^*$, we basically obtain noise with variance σ_n^2 that, as a first approximation, can be considered proportional to the amplitude ρ whenever $\rho \gg \sigma_0^2$. We obtain:

$$\sigma_n^2 = 2\rho\sigma_0^2 \quad (6.7)$$

In this case too it is possible to define the maximum likelihood estimate of the interferometric phase ϕ. Starting from N independent measurement v_i,$i = 1, \ldots, N$ of $V = v_1 v_2^*$ we can define a *likelihood function* in terms of conditional density of the measured interferogram and the true interferometric phase :

$$p(V \mid \phi) = p(v_1, \ldots, v_i, \ldots, v_N \mid \phi) = \prod_{i=1}^{N} p(v_i \mid \phi) \quad (6.8)$$

The value $\hat{\phi}$ of ϕ that maximises $p(V \mid \phi)$ is the *maximum likelihood* estimate of ϕ.

We can exploit equation 6.8 as:

$$p(V \mid \phi) = \int_0^{+\infty} p(V \mid \phi, \rho)p(\rho)d\rho \quad (6.9)$$

We have:

$$p_{v_i}(v_i \mid \phi, \rho) = p_n(v_i - \rho e^{j\phi} \mid \rho) \quad (6.10)$$

where $v_i - \rho e^{j\phi}$ is the noise added to the interferogram, that can be assumed to be a zero mean complex Gaussian variate with variance described by equation 6.7.

By substituting equation 6.3 in equation 6.9, we obtain:

$$p(V \mid \phi) = \int_0^{+\infty} \prod_{i=1}^{N} p_n(v_i - \rho e^{j\phi} \mid \rho)p(\rho)d\rho \quad (6.11)$$

Since we assumed that the noise variance is proportional to ρ, this equation can be re-written as:

$$p(V \mid \phi) = C \exp\left(\sum_{i=1}^{N} r_i \cos\phi + \sum_{i=1}^{N} s_i \sin\phi\right) \int_0^{+\infty} \mathcal{F}(\rho)d\rho \quad (6.12)$$

where C is a constant, $v_i = r_i + \jmath s_i$ and

$$\mathcal{F}(\rho) = \exp\left(\frac{-\sum_{i=1}^{N} r_i^2 - \sum_{i=1}^{N} s_i^2}{2\rho\sigma_n^2} - \frac{\sum_{i=1}^{N} \rho}{2\sigma_n^2} - \frac{\rho}{\rho_m}\right)$$

does not depend on ϕ.

Setting the first derivative of equation 6.12 with respect to ϕ equal to zero, after some calculations it is possible to derive the expression of $\hat{\phi}$:

$$\hat{\phi} = \arctan\left(\frac{\sum_{i=1}^{N} s_i}{\sum_{i=1}^{N} r_i}\right) = \arg(< V >) \tag{6.13}$$

Therefore, the maximum likelihood estimate of ϕ can be derived from equation 6.2 with constant weights.

Again the best estimate is obtained by averaging the complex values, retaining the interferogram amplitude (i.e. low-pass filtering of the interferogram). The lower quantiles might be suppressed if we remember the approximation made neglecting the component of the superimposed noise not proportional to ρ.

6.2 Slope driven smoothing of the interferogram

Up to now we have assumed the case of a constant interferometric phase corrupted by noise. In practice, however, the interferometric phase changes proportionally to the terrain elevation. Thus, before averaging the complex interferogram values, the actual interferometric phase should be estimated and compensated. Likewise, the interferogram should be band-pass filtered around the estimated local frequency of the fringes (proportional to the local terrain slopes). The search of the local frequency can be carried out with widely differing techniques of spectrum estimation, both parametric and non-parametric. As far as the filter bandwidth is concerned, it depends on the required signal to noise ratio and spatial resolution.

As an example, the phase of two interferograms before and after the slope driven smoothing are shown in figure 6.1. They have been obtained from the ERS-1 stereo pair of Mt. Vesuvius already shown in section 4. The used bandwidth is 1/5 of the Nyquist frequency both in azimuth and range directions.

A schematic description of the software for interferograms generation is presented in appendix B.

6.3 Deterministic unwrapping method

We have pointed out that the phase unwrapping problem can be usefully approached as the problem of the integration of the estimated local slopes of the terrain.

In the following, the unwrapped phase map (or equivalently the elevation map) will be indicated with $\phi(x, y)$ and its first derivatives with respect to the azimuth and slant range directions (proportional to the local terrain slopes) with $\phi_x(x, y)$ and $\phi_y(x, y)$ respectively.

From the interferometric principal phase $\phi_p(x, y)$ we estimate the first derivatives of the unwrapped phase $\phi(x, y)$ in azimuth and slant range. We shall call them $\phi_x^e(x, y)$ and $\phi_y^e(x, y)$ respectively. The simplest estimation of $\phi_x^e(x, y)$ and $\phi_y^e(x, y)$ can be obtained as follows[1].

---

[1] More accurate estimation techniques can be used with a big benefit of the quality of final result at the cost of a longer computation time

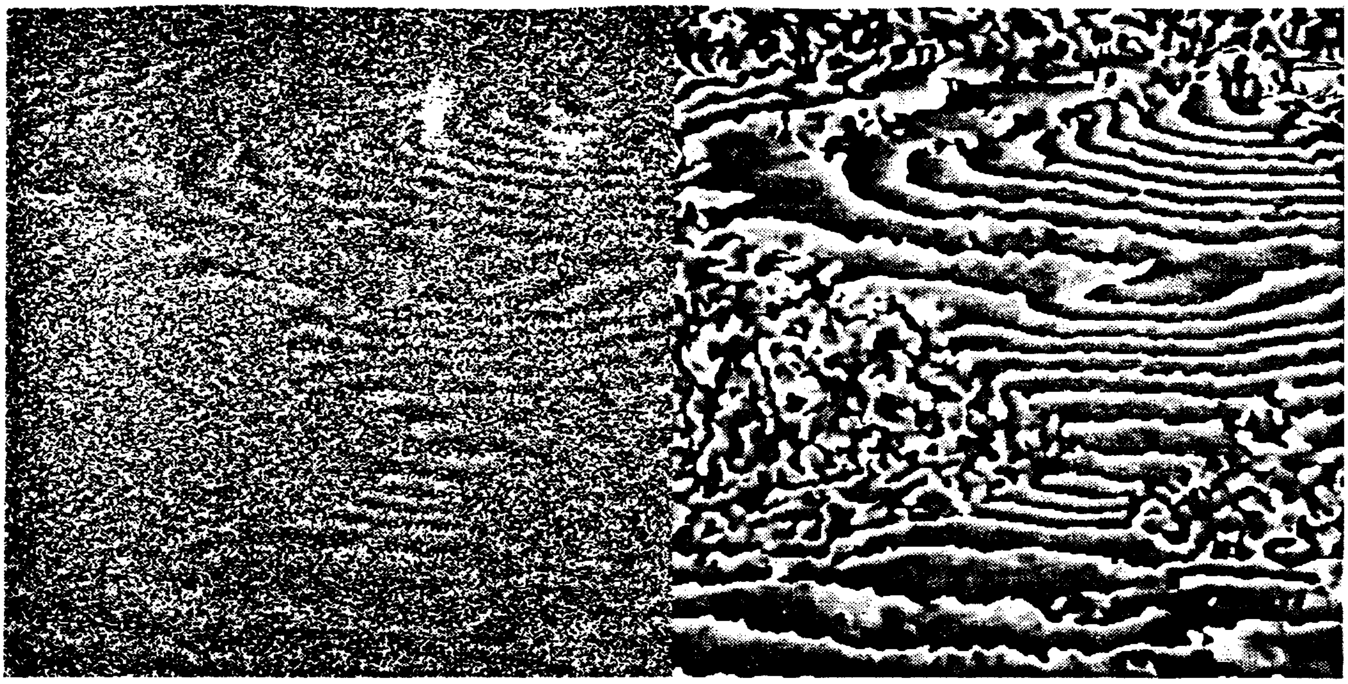

Figure 6.1: ERS-1 descending orbit - Mt. Vesuvius (Italy) August 27th and September 5th, 1991. Left: Original interferogram phases. Right: smoothed interferogram phases.

Let $\Delta\phi_x = \phi_p(x+\delta x, y) - \phi_p(x,y)$ and $\Delta\phi_y = \phi_p(x, y+\delta y) - \phi_p(x,y)$ be the difference between the principal phase values of the adjacent samples in azimuth and slant range respectively. The sampling rate in azimuth and range have been indicated as δx and δy respectively.

Since, for hypothesis, the phase difference between adjacent samples is supposed to be smaller than π (no phase aliasing),

- if $\mid \Delta\phi_x \mid < \pi$ then $\phi_x^e(x,y) = \Delta\phi_x$;
- if $\Delta\phi_x \leq -\pi$ then $\phi_x^e(x,y) = \Delta\phi_x + 2\pi$;
- if $\Delta\phi_x \geq \pi$ then $\phi_x^e(x,y) = \Delta\phi_x - 2\pi$.

The same is done for $\phi_y^e(x,y)$.

The phase unwrapping can then be performed by integrating the phase derivatives $\phi_x^e(x,y)$ and $\phi_y^e(x,y)$ along an arbitrary path which passes through all the image samples. A check of the results is quite simple: in fact, if the above assumption is correct there will be no variations greater than π between adjacent points in the unwrapped phase. Furthermore, apart from a constant that depends on the starting point, the unwrapped phase will not be affected by any change of the integration path.

Unfortunately, with real data this assumption remains unsatisfied due to different effects:

- small or zero terrain backscatter that randomizes the image phases;

- noise superimposed on the images, or on the image correlation (due to decorrelation between the two SAR images);

- volumetric effects

- actual changes in terrain topography that cause a phase difference greater than π. This aliasing effect must be carefully considered during the unwrapping process as it can affect the results quite dramatically.

In fact, a local error that occurs during phase difference detection is propagated along all the points in the integration path and causes a global error; as a consequence, the unwrapped phase can present typical "2π jumps", their distribution depending on the integration path.

These are unacceptable results; error propagation is particularly troublesome.

In practice, the interferometric phase may have values greater than π along lines *(ghost lines)*; if these lines are crossed by the integration line, cycle skips are generated, that will propagate. To get a correct result, the integration path must avoid crossing the ghost lines. Thus the problem lies in the identification of the ghost lines location. There is no simple solution to the ghost line identification problem unless information on the topography is available for instance from another interferometric path with different (shorter) baseline. However, it will be demonstrated that ghost lines can be approximated quite well, thus limiting error propagation to a small area around the phase discontinuities: wide propagation of phase error will be avoided.

The end points of the ghost lines can be detected by integrating (summing since we are dealing with a sampled field) the interferometric fringes derivatives $\phi_x^e(x,y)$ and $\phi_y^e(x,y)$ on an arbitrary enclosure c. If the enclosure c does not cross the ghost line or crosses it twice, the phase field inside the enclosure is irrotational and the result of the sum is zero. On the contrary, if the enclosure crosses the ghost line once the field inside the enclosure is rotational and the result of the sum is 2π. Furthermore, its algebraic sign (+ or $-$) depends on the crossing direction. The enclosure c can then be shrunk to the smallest allowed width (four adjacent points) and the phase derivatives summation performed over all the minimal enclosures contained in the image. In this way, the end points of the ghost lines are associated with the minimal enclosures which produce a non-zero summation: these end points are called *"singular points"* [21]. Knowledge of the singular point position does not imply knowledge of the ghost line; if no other information is available, any line connecting two end points of different algebraic sign is an admissible ghost line. However, if the correct ghost line is substituted by a straight line connecting two singular points, the phase error propagation will be limited to the area outlined by the straight line itself and the real ghost line, thus avoiding larger error propagation.

For the sake of simplicity, the ghost lines can be approximated by straight lines (cuts) between pairs of singular points of opposite algebraic sign [2]. If there are only a few well spaced ghost lines it is easy to obtain a fairly correct result; however, with real SAR data there are a lot of singular points and it is difficult to determine which points should be connected. In fact, if no a priori information or assumption is available, sets of ghost lines can be an admissible solution to the phase unwrapping problem, each set being composed by lines connecting singular points of opposite algebraic sign and covering all of the points.

To solve this point-connecting problem for large numbers of singular points a clusterization strategy is adopted: the closest singular points are collected in clusters which are in turn connected by ghost lines representing the shortest distances between the clusters. In this way, the disposition of the estimated ghost lines depends only on the distance between the singular points. Note that the error propagation remains limited, even if some ghost lines are poorly approximated.

---

[2] More sophisticated techniques have been developed in [2, 15, 21]. Moreover, a new approach that uses the lowest coherence lines connecting two end points as the most probable ghost lines has been developed.

The proposed technique can be summarized in the following points:

1. Grouping of all the singular points into "clusters":
   a point belongs to a specified cluster if its distance from at least one member of that cluster is less than a given threshold. In practice, all the points of the same cluster are so close that it is impossible to determine the true disposition of the individual ghost line.
2. Connection of all the members of the same cluster:
   given that it is impossible to determine which singular points must be connected, all of them are linked. However two singular points are directly connected only if their algebraic enclosure signs are different.
3. Connection of the points of different clusters:
   a search is made for the set of minimal distances connecting all the clusters. The cuts are performed as described in point 2 and cannot generate an enclosed path; the distance between the end points of the approximated ghost line can be less than a given maximum value.

This last condition of minimal distance cuts is meaningful as the elevation discontinuities of the observed area cannot be too widespread.

An example of deterministic phase unwrapping is shown in figure 6.2.

6.4 Multi-baseline deterministic phase unwrapping

Large fringes maps (e.g. 50×50 km^2) obtained from ERS-1 repeated passed generally contain regions of very low coherence. The interferometrical phase can be correctly integrated in high coherence areas only. Thus, regions with low coherence are found and then separated from the rest of the interferometrical image (this step avoids to draw many useless ghost lines). Given that, many isolated regions are generally produced (see the example in figure 6.2). Consequently there is a constant difference between the unwrapped phase values obtained in the different regions: this constant depends on the phase values of the first point of the integration path. In order to obtain a good elevation map the constant phase shifts between the blocks must be recovered. If the phase unwrapping process has been correctly carried out, the phase shifts are integer multiples of 2π.

In fact if, in accordance with the first point of the integration path, the principal value of the unwrapped phase is assigned to this phase, the value of the first point can differ from the real value only in multiples of 2π. Thus all the points of the same region, obtained by integrating the phase differences, are shifted by the same 2π multiple. It is then obvious that the phase shift may be different for points belonging to disconnected regions, since the unwrapped phase values were obtained in separate integrations. Consequently, to level the regions, only the correct multiple of 2π must be identified. This can be done in two ways: manually, if a map and reference points are available; automatically, if more than two interferometric images are available. The manual procedure exploits the relationship between unwrapped phases and relative elevations. It needs no detailed explanations.

More interesting comments can be made for the second possibility. Let us refer again to section 5.3 and, in particular to equation 5.4 that is written here as a function of ω instead of k_y and k_z.

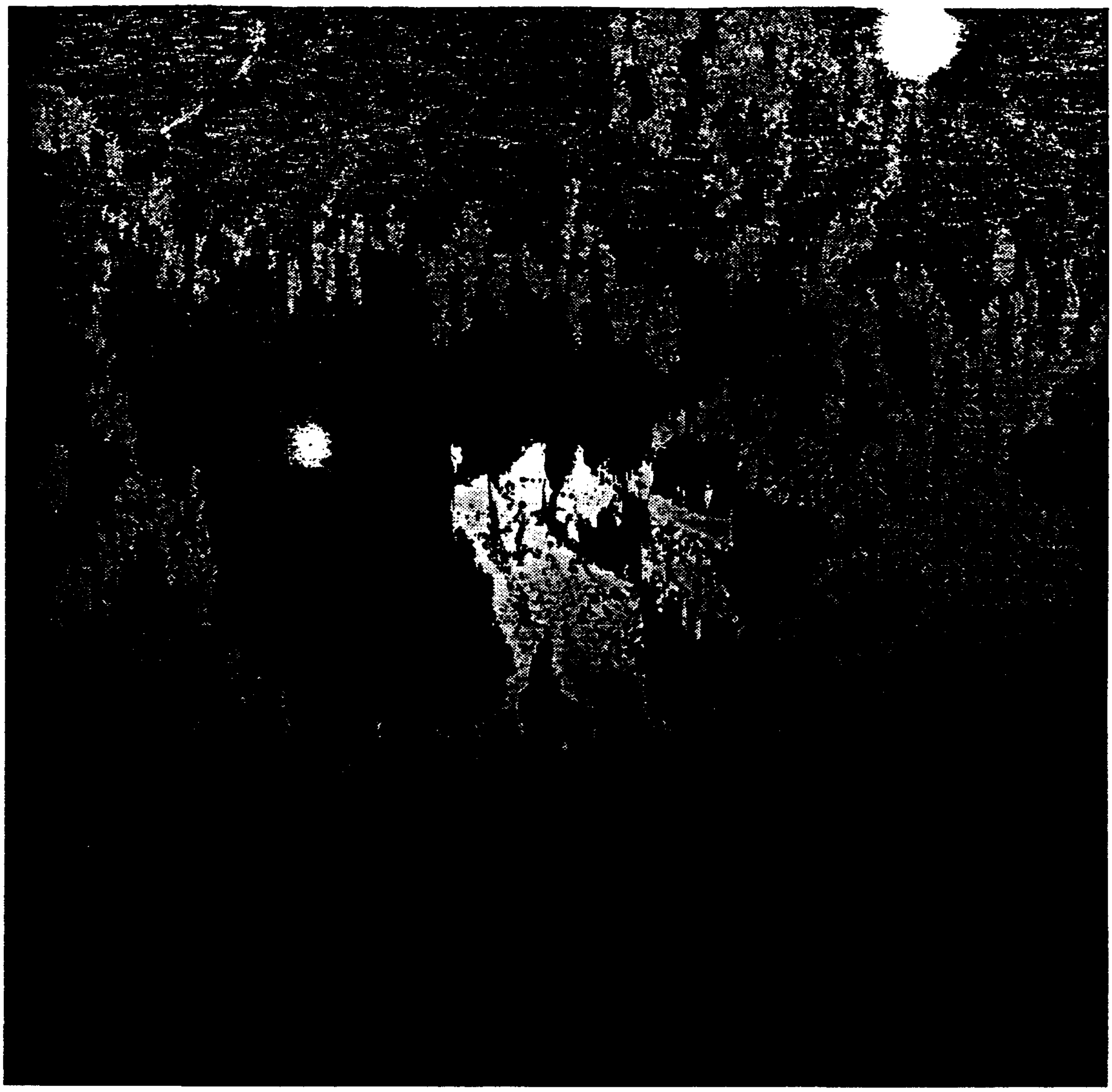

Figure 6.2: Unwrapped phase values of the area of Mt. Vesuvius. Inside the regions where phase unwrapping was impossible (no coherence) the phase unwrapping has not been performed (black regions).

$$A(\omega,\theta)=\iint a(y,z)\exp\left(j\frac{2\omega}{c}(y\sin\theta - z\cos\theta)\right)dydz \tag{6.14}$$

Let us now suppose to have no volume effect. That is the ground reflectivity $a(y,z)$ can be written as follows:

$$a(y,z) = a(y)\cdot\delta(z-z_o) \tag{6.15}$$

With such an assumption, equation 6.14 (the received signal) takes the following form:

$$A(\omega,\theta)=\exp\left(-j\frac{2\omega}{c}z_o\cos\theta)\right)\int a(y)\exp(j\frac{2\omega}{c}y\sin\theta\right)dy \tag{6.16}$$

By changing the looking angle from θ to $\theta+\Delta\theta$ and the frequency from ω to $\omega+\Delta\omega$ (i.e. following the spectral shift principle), we get a different signal:

$$A(\omega+\Delta\omega,\theta+\Delta\theta)=\iint a(y,z)\exp\left(j2\frac{\omega+\Delta\omega}{c}(y\sin\theta - z\cos\theta)\right)dydz \tag{6.17}$$

By substituting the expression of $\Delta\omega$ induced by the looking angle change $\Delta\theta$, the following result holds:

$$\begin{aligned} &A(\omega+\Delta\omega,\theta+\Delta\theta)= \\ &=\iint a(y,z)\exp\left(j2\frac{\omega-\omega\Delta\theta/\tan\theta}{c}(y\sin\theta - z\cos\theta)\right)dydz= \\ &=\iint a(y,z)\exp\left(j\frac{2\omega}{c}(y\sin\theta - z\cos\theta)\right)\exp\left(j\frac{2\omega\Delta\theta z}{c\sin\theta}\right)dydz \end{aligned} \tag{6.18}$$

Finally, assuming the surface reflectivity of equation 6.15, we get the following:

$$\begin{aligned} &A(\omega+\Delta\omega,\theta+\Delta\theta)= \\ &=\exp\left(-j\frac{2\omega}{c}z_o\cos\theta)\right)\exp\left(j\frac{2\omega\Delta\theta z_o}{c\sin\theta}\right)\int a(y)\exp\left(j\frac{2\omega}{c}y\sin\theta\right)dy= \\ &=A(\omega,\theta)\exp\left(j\frac{2\omega\Delta\theta z_o}{c\sin\theta}\right)=A(\omega,\theta)\exp\left(j\frac{4\pi B_n}{H\lambda\tan\theta}z_o\right) \end{aligned} \tag{6.19}$$

The phase difference between the first and second images is linear with the baseline B_n and with the elevation z_o. Thus, in principle, if multi-baseline images are available, the absolute elevation of each pixel of the SAR image could be derived by measuring the phase slope as a function of the baseline.

In practical cases (e.g. ERS-1), however, also the radial position of the satellite changes (not only its angular position as it has been assumed to derive equation 6.19). A constant phase, different for each image, should be included in the model. The signal received from the i_{th} image has the following expression:

$$A_i(\omega_i,\theta_i)=A(\omega,\theta)e^{j\phi_i}\exp\left(j\frac{4\pi B_n}{H\lambda\tan\theta}z_o\right) \tag{6.20}$$

Since the phase ϕ_i is not known, absolute elevations cannot be derived. Nonetheless, if the phase of a reference pixel (just one on the whole image) of known elevation z_r is subtracted to all the other pixels of the SAR image (i.e. in such a way that the phase of the reference pixel is set to zero for all the images), then the received signal in correspondence of a pixel of elevation z_o, becomes:

$$A_i(\omega_i, \theta_i) = A(\omega, \theta) \exp\left(j \frac{4\pi B_{ni}}{H\lambda \tan\theta}(z_o - z_r)\right) \tag{6.21}$$

Again, for each pixel of the SAR image, the phase slope as a function of the baseline can be exploited to derive their elevation relative to that of the reference pixel.

Coming to our original problem, it is clear that this multi-baseline technique can be usefully exploited to derive the relative elevation (as well as the relative phase) of the isolated blocks already unwrapped by means of the deterministic method.

6.5 LMS unwrapping in the frequency domain: rectangular regions

An alternate way of integrating the local terrain slopes (phase derivatives) will be described in this section. The main advantage of this method is that no strategy of ghost lines connection is required. An automatic DEM generator from SAR interferometry could benefit of such a technique.

By transforming the phase derivatives $\hat{\phi}_x(x, y)$ and $\hat{\phi}_y(x, y)$ into the wavenumber domain (from x, y into k_x, k_y), we get the two functions $\hat{\Phi}_{kx}(k_x, k_y)$ and $\hat{\Phi}_{ky}(k_x, k_y)$.
Then, we form the estimated solution in the wavenumber domain

$$\hat{\Phi}(k_x, k_y) = a\hat{\Phi}_{kx}(k_x, k_y) + b\hat{\Phi}_{ky}(k_x, k_y) = a(\Phi_{kx}(k_x, k_y) + n_1) + b(\Phi_{ky}(k_x, k_y) + n_2)$$

where n_1 and n_2 are the measurements noises (see section 4) supposed to be independent and with the same variance ϵ^2.
We indicate the error between the actual unwrapped phase and the estimated solution as

$$E = \Phi(k_x, k_y) - \hat{\Phi}(k_x, k_y)$$

The coefficients a and b minimize the LMS difference. The following relations hold:

$$\langle (\Phi - a(\Phi_{kx} + n_1) - b(\Phi_{ky} + n_2)) (\Phi_{kx} + n_1)^* \rangle \tag{6.22}$$

$$\langle (\Phi - a(\Phi_{kx} + n_1) - b(\Phi_{ky} + n_2)) (\Phi_{ky} + n_2)^* \rangle \tag{6.23}$$

Here the symbol $< \cdot >$ means an average and the $*$ a complex conjugate. After some tedious algebra the following expression of the coefficients a and b are found:

$$a = \frac{-jk_x}{k_x^2 + k_y^2 + \epsilon^2} \tag{6.24}$$

$$b = \frac{-jk_y}{k_x^2 + k_y^2 + \epsilon^2} \tag{6.25}$$

Eventually, the estimate of the unwrapped phase in the Fourier transformed domain is:

$$\hat{\Phi}(k_x, k_y) = a\hat{\Phi}_{kx}(k_x, k_y) + b\hat{\Phi}_{ky}(k_x, k_y) = \frac{-jk_x\hat{\Phi}_{kx}(k_x, k_y) - jk_y\hat{\Phi}_{ky}(k_x, k_y)}{k_x^2 + k_y^2 + \epsilon^2} \tag{6.26}$$

This equation corresponds in the space domain to the following partial differential equation:

$$\frac{\partial^2\hat{\phi}(x,y)}{\partial x^2} + \frac{\partial^2\hat{\phi}(x,y)}{\partial y^2} + \epsilon^2\hat{\phi}(x,y) = \frac{\partial\hat{\phi}_x(x,y)}{\partial x} + \frac{\partial\hat{\phi}_y(x,y)}{\partial y} \tag{6.27}$$

Notice that the effects of the damping factor (measurements error power) ϵ^2 are largest for low wavenumbers. This means that low frequency components (as, for example, constant slopes in azimuth and range) are not reliable and must be determined exploiting GCP's.

The main steps of this phase unwrapping technique can be summarized as follows:

- 1 The local interferometric phase derivative maps (local terrain slopes) both in azimuth and slant range are computed from the interferogram.
- 2 These maps are Fourier transformed both along x and y.
- 3 The partial differential equation 6.26 is solved.
- 4 The result is back transformed.

The first step is critical. Particular care must be taken in Fourier transforming the phase derivatives maps in order to avoid edge and periodicity effects.

The main drawback of the wavenumber unwrapping method is that whenever large areas of low coherence are present in the interferometric fringes map, even the results outside those areas might be affected by large errors. In fact, no estimation of the terrain slope is possible there. Thus, without other information available, these slope values are set to zero. Since the method operates in the transformed domain, there is no way to separate these areas from the rest of the image (on the contrary this is always possible with the ghost lines method). Then, the best solution to this problem is that of using other available data (essentially the available DEM derived by means of other techniques or even by different interferometric SAR data) in order to derive an estimation of the terrain slopes in problematic areas. However, those data are not always available and, even if available, may not be registered to SAR images with high accuracy.

Additional tests must be added in order to check if the final result is consistent with the original data. The difference between the obtained result and the original interferometric phase is taken. From now on we shall call this the residue $\eta(x, y)$ of the phase unwrapping:

$$\eta = (\hat{\phi} - \phi)_p \tag{6.28}$$

Now, there are two possibilities.

A) The residue η outside the low coherence areas is smaller than 2π (its principal values do not show fringes discontinuities if a proper phase constant is added). In such a case, the solution consistent with the original fringes (that is the best we can recover from the data themselves) can be directly found by adding the residue to the estimated unwrapped phase $\hat{\phi}$.

B) The residue shows fringes discontinuities; then, further processing steps are required.

The local terrain slopes in the low coherence areas are computed from the first estimation of the unwrapped phase $\hat{\phi}$. The processing steps from 2 to 4 are repeated. This procedure is iterated until the residue is stationary (in general $4-5$ iterations are enough). Finally, if the residue shows fringes discontinuities, it is unwrapped by means of the ghost lines method (which allows to avoid the low coherence areas).

6.6 LMS phase unwrapping in the spatial domain: irregular regions

From what we have seen in the previous section, the phases can be unwrapped in the least square sense using the Fourier domain technique, provided that the region where the data are available is fit to be Fourier transformed, i.e. is rectangular. This is never the case, though, and in general we can expect the region to be quite complex, with disconnected regions and in general complicate boundaries.

Therefore, we have to move to the spatial domain, abandoning the wavenumber domain, unless more sophisticated techniques, now being studied, will be implemented.

The LMS unwrapping in the spatial domain goes as follows:

- the deterministic unwrapping is carried out in a disconnected set of regions;

- each region is unwrapped relative to the others using either GCP's, coarse topography, or multiple baselines and some variation of the chinese remainder theorem. In fact, a periodicity with respect to unrelated periods can be removed comparing the residuals with different moduli of periodicity. Another solution, possible if many baselines are available, has been described in section 6.4. In that case, a regression along the baseline axis is used to derive a **direct and pointwise estimate** of the elevation, without 2Dunwrapping.

- the partial differential equation 6.27 linking local slopes to unwrapped phases is solved in the spatial domain, using relaxation techniques. In this stage, boundaries like coasts, railways, rivers etc. can be used without unnecessary complexity. The deterministically unwrapped regions appear as boundaries. In the following of this section, we shall detail this procedure.

The values of the phase where the deterministic technique could not work can be determined by interpolating the available values of the unwrapped phase, say in the wavenumber domain, as we have seen in the previous sections. However, to better understand what happens when the integration of the partial differential equation of the slopes is carried out in a least square sense in the spatial domain, we summarize here the analysis made in [27, 29].

The phase is considered as a potential field, the sum of rotational and irrotational components [27, 28].

The irrotational part is unique and independent of the aliasing effects, whereas the rotational part depends on the singular points and the unknown ghost line disposition. If no ghost lines are present the results of the deterministic and LMS techniques are the same.

In order to further explain this unwrapping method, in presence of ghost lines, let us consider the principal value of the differences of the principal phase values

$$\begin{aligned}\Delta_i\psi &= [\psi(i+1,j)-\psi(i,j)]_p\\ \Delta_j\psi &= [\psi(i,j+1)-\psi(i,j)]_p\end{aligned} \tag{6.29}$$

where the differences are estimated as the "true phase differences" defined in section 6.3. In other words, when the phase difference is greater or lower than π, 2π is added or subtracted.

The notation $[\cdot]_p$ means the principal value of the argument.

Thus, we can define the *gradient of the principal phase values* as follows:

$$\vec{\nabla}\psi_p(i,j) = \Delta_i\psi(i,j)\,\vec{\mathrm{i}} + \Delta_j\psi(i,j)\,\vec{\mathrm{j}} \tag{6.30}$$

where $\vec{\mathrm{i}}$ and $\vec{\mathrm{j}}$ are the unit versors in the azimuth and slant range direction, respectively.

When no phase aliasing effect appears, the phase differences estimated in 6.29 coincide with the unwrapped phase differences; as a consequence the gradient of the principal values is identical to the unwrapped phase gradient.

In general, the phase field generated by the phase gradient follows the expression:

$$\vec{\Psi}(i,j) = \vec{\nabla}\psi_p(i,j) \tag{6.31}$$

Now, since the principal phase value gradient is solely determined from the gradient of a scalar function (the unwrapped phase), the corresponding field is irrotational.

On the contrary, when phase aliasing occurs, the principal values and the unwrapped phase differences are not the same, and the phase field is no longer irrotational.

However, we can decompose the field into an irrotational component ($\vec{\Psi}_I$) and a rotational component ($\vec{\Psi}_R$):

$$\vec{\Psi} = \vec{\Psi}_I + \vec{\Psi}_R \tag{6.32}$$

Exploiting a well-known mathematical property,

$$\mathrm{div}\,\vec{\Psi}_R = 0 \tag{6.33}$$

$$\mathrm{rot}\,\vec{\Psi}_I = 0 \tag{6.34}$$

From 6.33, it follows that

$$\begin{aligned}\mathrm{div}\,\vec{\Psi} &= \mathrm{div}\,\vec{\Psi}_I\\ \mathrm{div}\,\vec{\nabla}\psi_p &= \nabla^2\psi_p = \nabla^2\psi_I\end{aligned} \tag{6.35}$$

where ∇^2 is the Laplace operator. Notice that this equation is identical to equation 6.27 derived in the frequency domain, apart from the term proportional to ϵ^2 used to combat additive noise.

The discrete expression of 6.35 is:

$$\begin{aligned}&(\psi_I(i+1,j)-\psi_I(i,j))+(\psi_I(i-1,j)-\psi_I(i,j))+\\&\quad(\psi_I(i,j+1)-\psi_I(i,j))+(\psi_I(i,j-1)-\psi_I(i,j))=\\&[(\psi_p(i+1,j)-\psi_p(i,j))]_p+[(\psi_p(i-1,j)-\psi_p(i,j))]_p+\\&\quad[(\psi_p(i,j+1)-\psi_p(i,j))]_p+[(\psi_p(i,j-1)-\psi_p(i,j))]_p\end{aligned} \tag{6.36}$$

This expression relates the irrotational phase component to be determined with the known principal phase values. Thus, exploiting equation 6.36, the irrotational component of the phase field is recovered.

The integration of the finite difference equation 6.36 requires boundary conditions. At the edge of the interpolation domain the unwrapped phase values are well known since they were computed at the previous unwrapping step. Thus, these values fix the boundary conditions.

The differential equation 6.36 can be integrated using relaxation techniques, usually exploited for electrical and magnetic field problems (Dirichlet problems).

The rotational phase field remains ambiguous; in fact, from the difference between the original phase and the irrotational component only its principal value can be determined:

$$[\psi_R]_p = [\psi_p - \psi_I]_p \tag{6.37}$$

In the following, we shall refer to this term as to the rotational residue of the LMS phase unwrapping technique.

6.6.1 Singular points and ghost lines in the LMS unwrapping

The rotational residue depends only on the singular points disposition. Moreover, it contains 2π phase discontinuities along lines connecting the singular points. These lines are not necessarily an estimate of the ghost lines described earlier in section 6.3.

The amplitude of the rotational residue tends to zero, moving away from the discontinuity lines, though the decrease is fairly slow: for example it can be shown [27, 28] that in the case of a single rectilinear ghost line, the maximum value is:

$$[\psi_R(x)]_{MAX} = 2\tan^{-1}\left(\frac{L}{2x}\right) \tag{6.38}$$

where L is the line length and x the normal distance from the line; no border effect has been considered.

Three possible situations can be identified on which LMS should be compared with deterministic unwrapping.

Case 1: Topographic phase aliasing and small irrotational residue.

If, due to the topography, there are a few singular points charged with a $\pm 2\pi$ curl, then the rotational residue shows only one line with a 2π phase discontinuity between a pair of singular points of opposite sign (charge). This discontinuity may approximate the ghost line.

If the irrotational component and the rotational residue are simply added, the result will approximately coincide with that obtained by the deterministic phase unwrapping technique

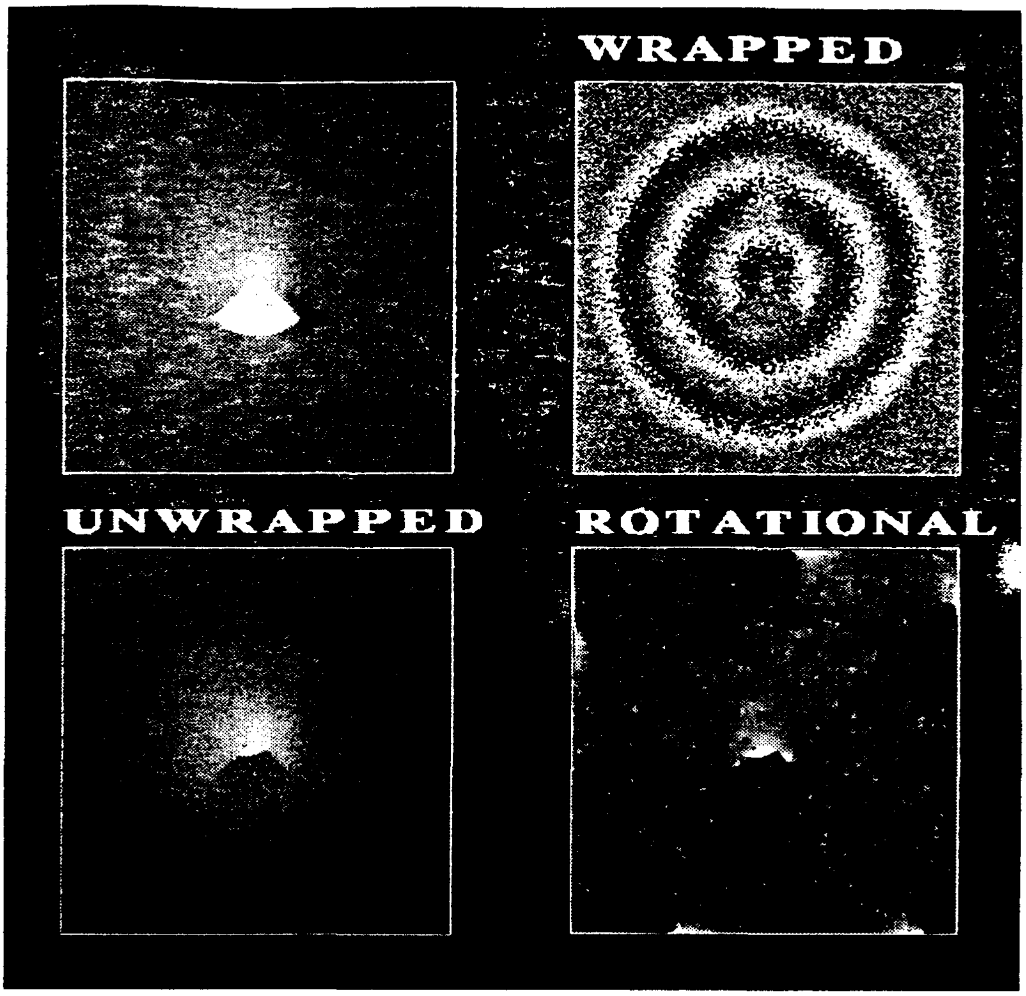

Figure 6.3: Up Left: Synthetic topography. Up Right: Corresponding phase values corresponding. Down Left: Sum of rotational and irrotational components. Down Right: Principal values of the rotational phase component. (Courtesy of U. Spagnolini)

derived in section 6.3 (LMS and deterministic unwrapping lead to the same result). As an example, figure 6.3 shows the decomposition of a synthetic phase image into rotational and irrotational components.

Case 2: Topographic phase aliasing and large irrotational residue.

When singular points charged with a $\pm 2n\pi$ curl appear, the amplitude of the rotational residue is larger than 2π in correspondence to the ghost line and tends to zero moving away from it. Thus, the rotational residue (that it is known in principal value only) shows n distinct lines with a 2π phase discontinuity between the same pair of singular points. In this case the rotational residue should be deterministically unwrapped before its summation to the irrotational component. So, as far as the computational time is concerned, the deterministic unwrapping is preferable.

Case 3: Many close singular points (low coherence regions).

Even if the topography is smooth (no topographic aliasing), phase noise (see section 4) gener-

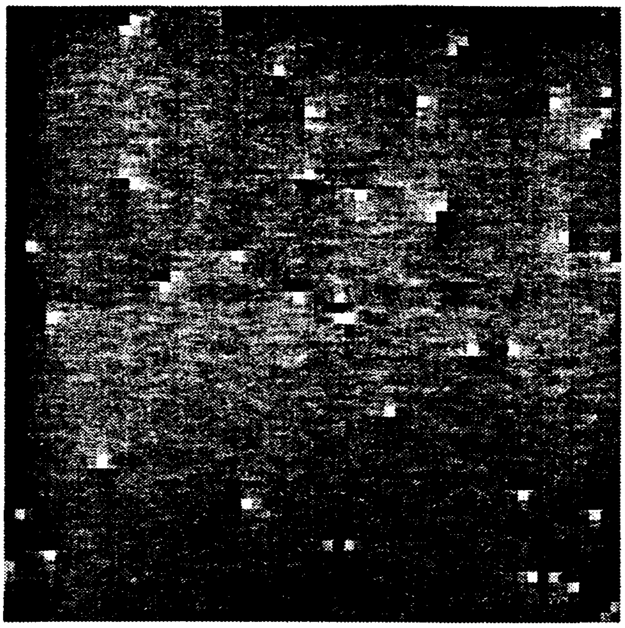

Figure 6.4: Rotational residue of a synthetic interferogram showing dipoles. They are visible as couples of black and white dots.

ates **couples of singular points** of opposite sign (dipoles) that are not related to physical ghost lines[3]. An example of dipoles generation is shown in figure 6.4 where a detail of the rotational residue of a synthetic interferogram (the used coherence is $\gamma = 0.8$) is drawn. The number of singular points depends on the stereo pair coherence. At zero coherence the number of singular points is approximately 1/3 of the total number of pixels and decreases as the coherence increases accordingly to the experimental curve shown in figure 6.5.

Thus, in case of low coherence, the rotational residue shows many short discontinuities that have no physical relation with the actual topography. On the other hand, the irrotational component of the LMS technique can be usefully exploited. In fact, if the unwrapped phase is replaced by its irrotational component only, the result will be a smoothed (and noisy) version of the actual topography. Notice that in this case also the deterministic unwrapping will fail due to the large number of singular points. Nonetheless, we remember now that coherence is improved (and the number of singular points decreased) if the interferogram is band-pass filtered as described in section 6.2. For the sake of simplicity let us suppose to deal with a constant interferometric phase corrupted by noise (the general case can thus be analyzed in the same way if we suppose to remove from the interferogram the smooth version of the topography, supposed to be a priori known). The signal to noise ratio Ξ increases linearly with the number N of averaged pixels (i.e. as a first approximation, a 2-D low pass filter with a normalized cut-off frequency of $1/\sqrt{N}$) and coherence changes accordingly. From equation 4.2 the following relation holds:

---

[3] In general, either single points or dipole can be generated by phase noise. However, the probability of having dipoles is much higher than that of single points especially with high signal to noise ratio. This is an important consideration since the rotational residue decreases with the square of the distance from dipoles and just with the distance from single points.

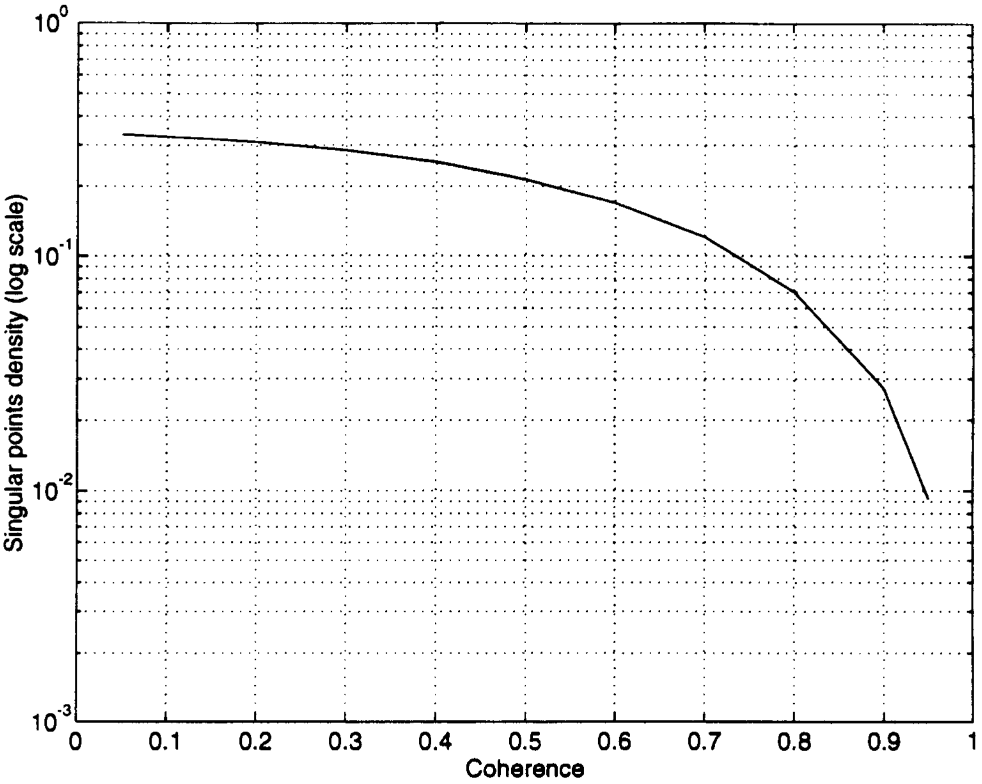

Figure 6.5: Number of singular points versus coherence: experimental curve

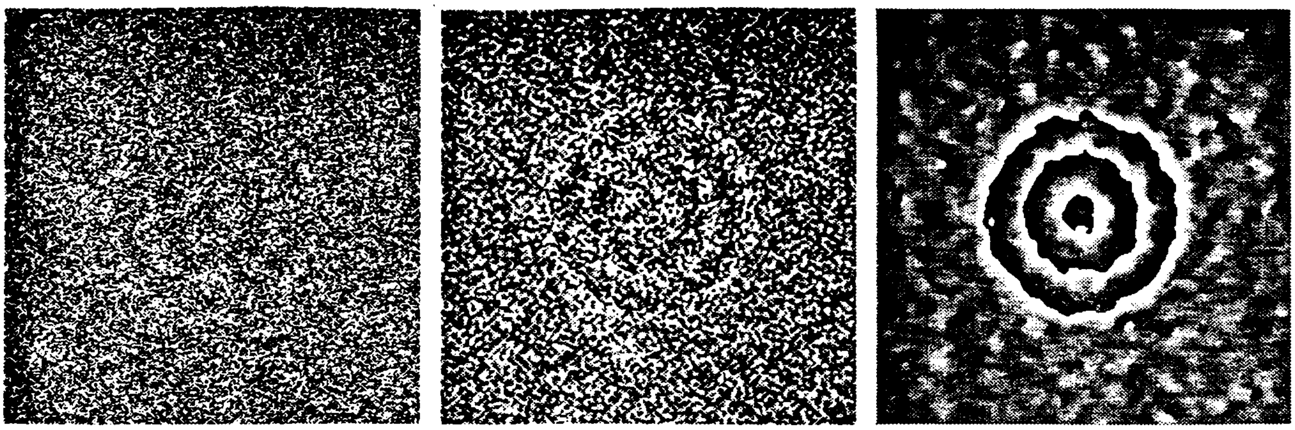

Figure 6.6: Synthetic interferometric fringes ($\gamma = 0.15$). Left: no filter. Middle: half band filter. Right: one tenth of band filter.

$$\gamma = \frac{\Xi}{1+\Xi} \tag{6.39}$$

By subsampling ($1 : N$) the filtered image, we get again samples affected by uncorrelated noise and we can refer again to the curve of figure 6.5 (i.e. the expected singular points density as a function of coherence). Thus, we can quantify the reduction of singular points induced by filtering:

i - The singular points density is reduced due to the coherence enhancement shown in figure 6.5;

ii - The number of singular points is further reduced by a factor of N due to subsampling.

However, in case of low coherence, **large errors could appear if too narrow filters are used**. Their central frequency, derived from local slopes (that are very noisy), might be wrong and meaningless fringes (generally with high spatial frequency) might be created.

A few examples will make this point clear. Let us suppose to deal with a given topography. Let us also suppose that the interferometric phase generated with an ERS-1 like geometry and a baseline of 193meters (i.e. the same baseline estimated for the descending Mt. Vesuvius image shown in figure 2.8) is corrupted by noise. A coherence $\gamma = 0.15$ is considered. The interferogram is then band-pass filtered with two different bandwidths (referred to the sampling frequency): 0.5 and 0.1. Please notice that in these examples the correct central frequency of the filters have been used.

Interferometric fringes before and after the two types of filtering are shown in figure 6.6.

The topography derived from the irrotational component only is then compared with the original one. Their difference is shown in figure 6.7.

The RMS elevation errors are reported below:

$$\begin{cases} \sigma_n = 30m & \text{if no filter is used} \\ \sigma_n = 12.5m & \text{if an half band is used} \\ \sigma_n = 3.3m & \text{if a 1/10 band filter is used} \end{cases}$$

The deterministic unwrapping can be used in practice only if the 1/10th band filter is used,

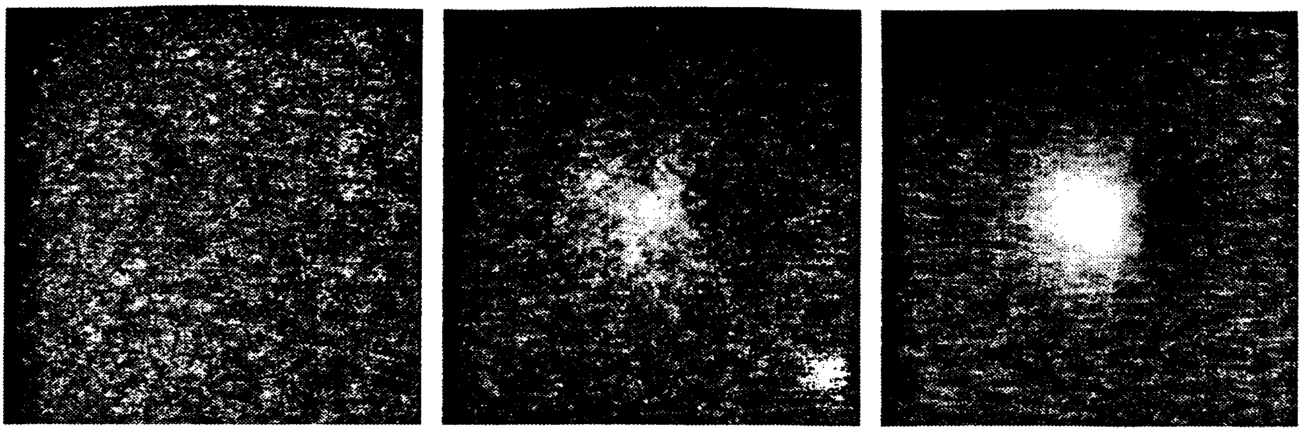

Figure 6.7: Topography derived from the irrotational component of the fringes shown in figure 6.6. Left: no filter. Middle: half band filter. Right: one tenth of band filter.

since in other cases too many isolated regions are created by the points connection algorithm. Furthermore, if we try to estimate the central frequency of the filter from the fringes themselves, the filtered fringes show many errors (wrong local frequencies) as shown in figure 6.8.

Thus, a case where the use of a LMS algorithm shows advantages with respect to the deterministic one has been identified. It should be usefully exploited in those low coherence regions where there are too many singular points for the deterministic technique to be applicable and where narrow band-pass filtering would lead to local frequency errors.

The combination of deterministic phase unwrapping in high coherence regions and LMS phase unwrapping in low coherence regions with a moderate band-pass filtering, leads to the best results we have achieved up to now.

Just as an example, the very first result of this techniques blending is shown in figure 6.9. Here, the fringes of Mt. Vesuvius already shown in figure 2.8 have been unwrapped and presented with a circular gray scale (200meters per cycle). Please notice that an approximate topography has been reconstructed in correspondence to low coherence regions ($\gamma < .26$) too. More accurate results are expected from a better tuning of the described procedure.

6.7 Rectification of the elevation map

The elevation map derived from SAR interferometry lies on a plane where the reference axes correspond to the azimuth and slant range directions. Such a coordinates system is completely different from the reference systems in the azimuth-ground range plane used in the usual elevation maps.

Thus it is necessary to transfer the unwrapped phase from the slant range coordinates system to the ground range system; the obtained values must be interpolated and resampled in terms of uniform ground range cells.

From Figure 6.10 it is evident that the horizontal position of a backscatterer depends on both the slant range coordinate and the elevation. Through simple geometrical expressions the relation between these three parameters can be found. The ground range coordinate with respect to the initial point, indicated by y, is the sum of two components: the first is the horizontal displacement

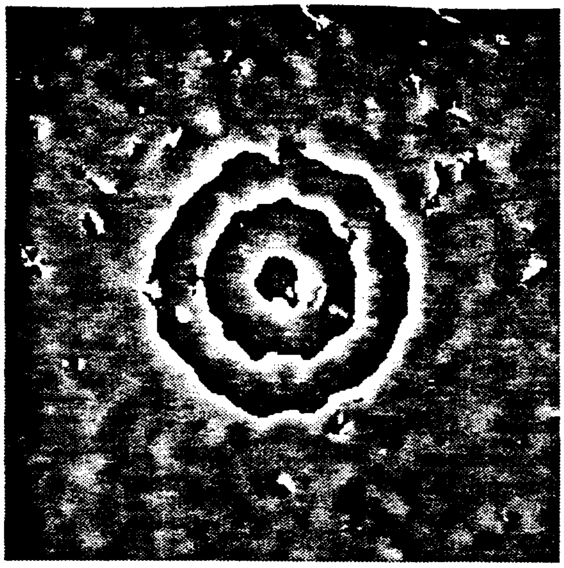

Figure 6.8: Synthetic interferometric fringes ($\gamma = 0.15$) filtered with an 1/10th band filter. Here, the filter central frequency has been estimated from the unfiltered fringes.

in the case of flat terrain, the second caused by a non-zero elevation drop.

$$y(r,q) = y_r(r) + \Delta y(q) \tag{6.40}$$

where

$$y_r = \frac{r}{\sin\theta}$$

$$\Delta y(q) = \frac{q(r)}{\tan\theta}$$

Since the position of the points depends on its elevation, the correspondence between ground range and slant range is quite irregular. In fact, the well known foreshortening effect causes a compression of the areas with ascending slope and a spread of the descending areas.

As a consequence the ground difference, corresponding to a constant slant range displacement, will be much larger in the case of ascending slopes. Furthermore, when layover effects occur several areas of the earth's surface can disappear from the SAR image.

In a ground range reference system the obtained elevation map will have a quite uneven sampling interval. Thus to obtain a regular sampled map the elevation values must be interpolated. For our purposes a linear interpolation is quite adequate. In fact, in flat or descending areas the interpolating points are fairly close, whereas with an ascending slope the foreshortening effect produces such a large slant range compression that the interpolating points lie much further away and no interpolator would suffice.

For example, for geometrical parameters like the ERS-1 mission, a slant range sampling $\delta r \simeq 8$m corresponds to a ground range step $\delta y = \delta r / \sin\theta \simeq 20$m for flat terrain; on the contrary for a terrain slope $\alpha = 15°$, the ground range step is

Figure 6.9: ERS-1 interferometry. Unwrapped phase of Mt. Vesuvius presented with a circular gray scale (200meters per cycle).
An approximate topography has been reconstructed in correspondence to low coherence regions too (see figure 2.8).

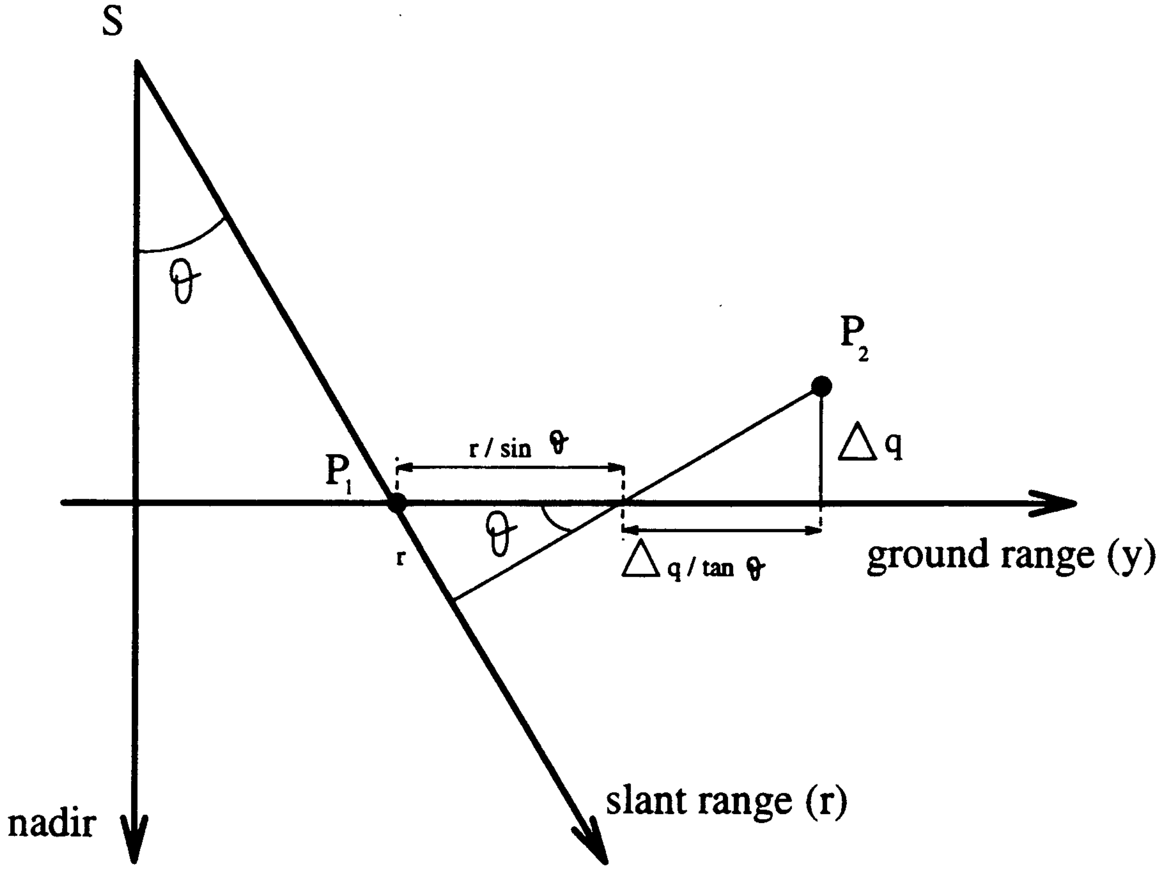

Figure 6.10: Cross-section of the SAR system geometry normal to the azimuth direction. The ground range coordinate depends on both the range position and the point elevation.

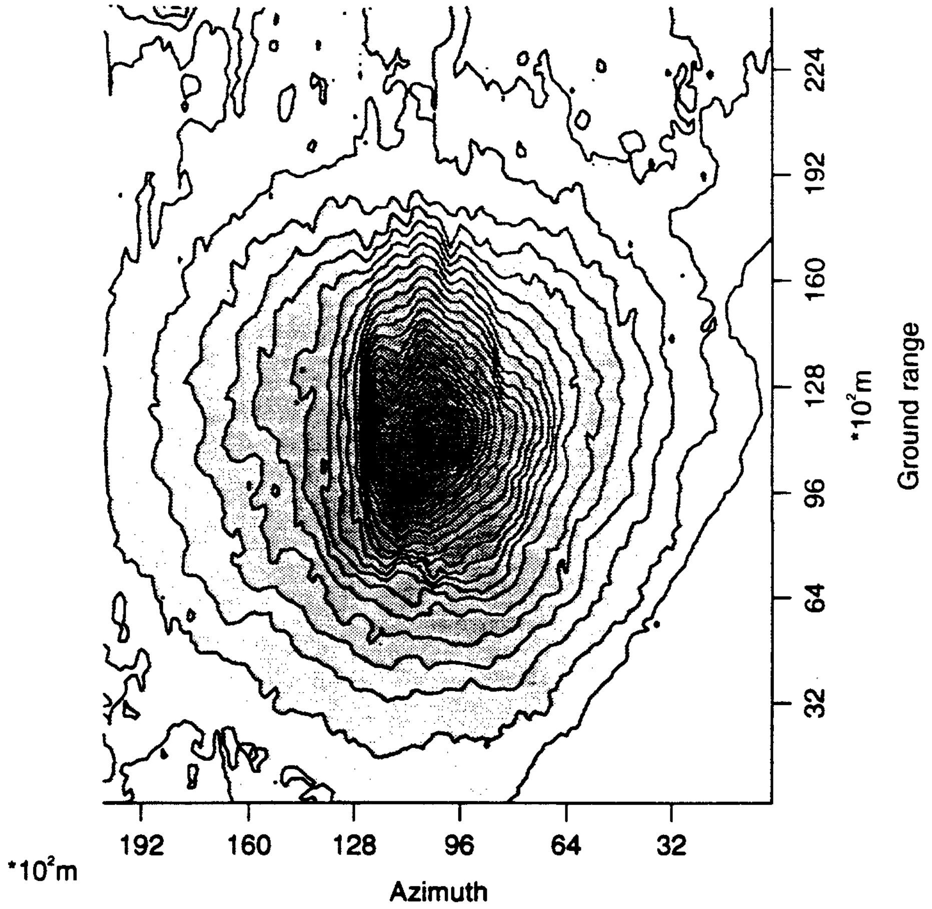

Figure 6.11: A topographic map of the area of Vesuvius obtained from the unwrapped and rectified phase, shown in the previous pictures.

$\delta y = \delta r \cos\alpha / \sin(\theta - \alpha) \simeq 60\text{m}$

The result of the rectification process, performed for the SAR image of the area near the Vesuvius is shown in Figure 6.11. Contour lines correspondent to descending orbits are shown. The following picture 6.12 shows a 3-D representation of the results.

6.8 A theme for future activity: optimum combination of different baselines and of data from ascending and descending orbits

Any current DEM estimate is very useful for unwrapping. In fact, data from different takes and therefore with different baselines can be combined, but only if properly positioned in space; in the case of a flat region, uninteresting for the unwrapping problem, the coregistration can be carried out using ephemerides. Not so in complex topography situation, where the registration is DEM

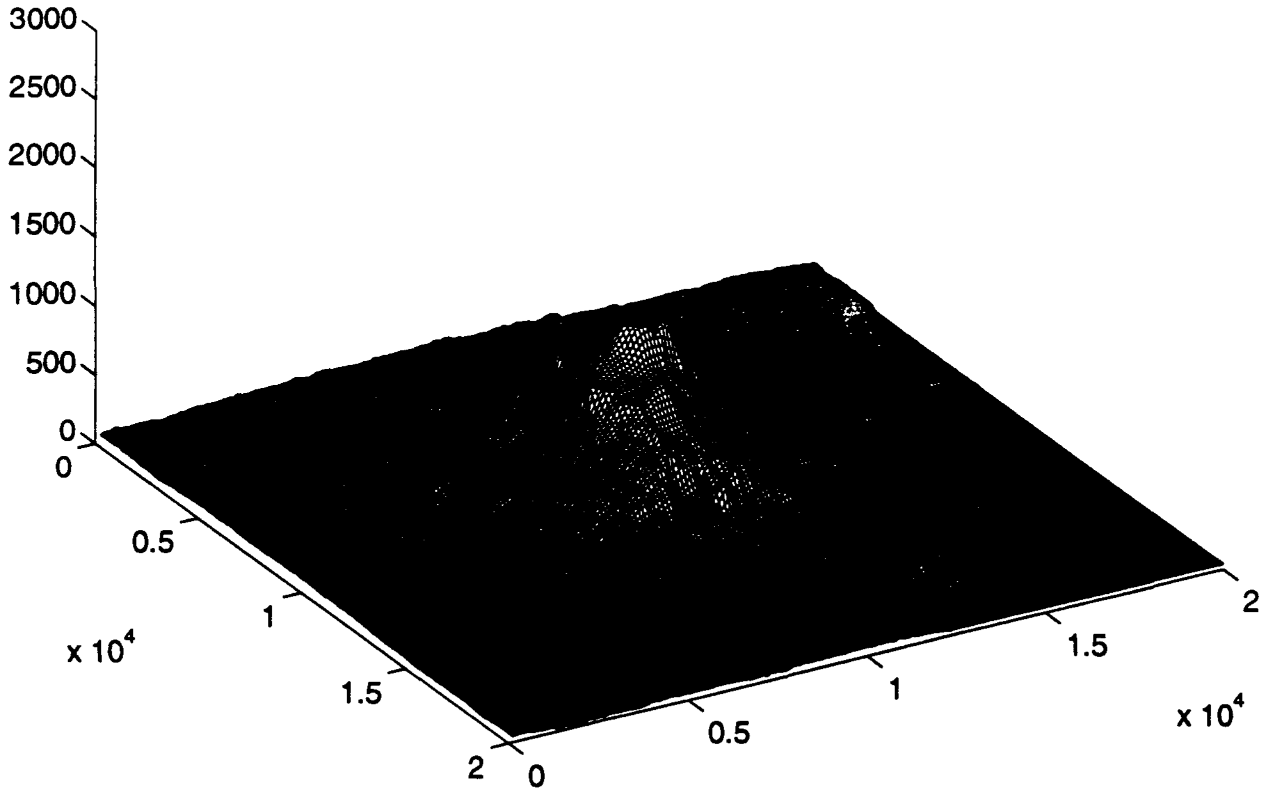

Figure 6.12: A 3-D representation of the map, presented in Figure6.11 .

dependent.

We arrive to an iterative procedure where the available data are combined in such a way to achieve a progressive improvement of the DEM.

In this operation, the combination of data from ascending and descending orbits, as discussed in [32], could be very helpful. First, to unravel the layover areas, that, if not in shadow, may appear well behaved with the other orbit. Second, and equally relevant, the combination of the two views is only possible if the DEM is correct; hence, it is a powerful check of its quality, to remove blunders, reduce the elevation dispersion, etc.

The activity in this direction is in progress and in it the georeferentiation part will be as relevant as unwrapping.

Once the data are approximately georeferentiated using the current DEM, each further data set improves somewhere the DEM, and therefore improves the quality of the product. However, it is not clear yet if the complete recalculation of the DEM of the area will be necessary or if the improvement will be less expensive than that.

The result of the rectification process, performed for the SAR image of the area near the Vesuvius using both ascend[illegible] the map is shown in figure 6.13) and descending orbits (the map is shown in figure 6.11) da[illegible]s shown in figure 6.14.

Since no existing DEM was available to us, other than a 1:25000 map, the consistency of the results have been checked by considering elevation differences in high coherence areas of both ascending and descending images. The map of elevation differences from white (−40m) to black (+40m) is shown in figure 6.15. It can be noted a large systematic error.

This effect depends on the estimation error of geometric parameters probably due to the inaccuracy of the used ground control points. This systematic error can be appreciated by considering the dispersion of elevation differences versus coherence shown in figure 6.16.

Three almost elliptical clusters (plus a fourth one at high coherence that will be considered later) can be identified in figure 6.16 vertically separated by a few tens of meters. The center of mass of these clusters indicates the systematic error still present in the generated elevation maps. The dispersion of each cluster, shows the actual elevation differences deviation that could be obtained by correcting systematic errors. In figure 6.17 the elevation differences histogram is shown for coherence $\gamma = 0.5$. Please notice the 3 almost gaussian curves with comparable deviations and different mean values.

Systematic errors have been estimated from the elevation differences map by fitting a quadratic function of the 3 spatial coordinates. After systematic errors subtraction the elevation differences versus coherence are shown in figure 6.18. Notice that now the elevation differences dispersion has been strongly reduced (from 28 to about 12 meters). This means that the expected elevation error (i.e. not the elevation differences) should be smaller than 6 meters.

In figure 6.19 the correspondent elevation differences histogram is shown for coherence $\gamma = 0.5$.

However, even after detrending, figure 6.18 shows some outliers at very high coherence. It is interesting to note that the location of these outliers is concentrated in a small region of Vesuvius as shown in figure 6.20.

That error could have been generated by a wrong phase unwrapping or (a much more suggestive hypothesis) by a small terrain motion. In conclusion it should be noted that, if outliers are not considered, the theoretically predicted elevation differences versus coherence are not so far from measurements as shown in figure 6.21.

As a final result, figure 6.22 shows the combination of the detected images after geometric

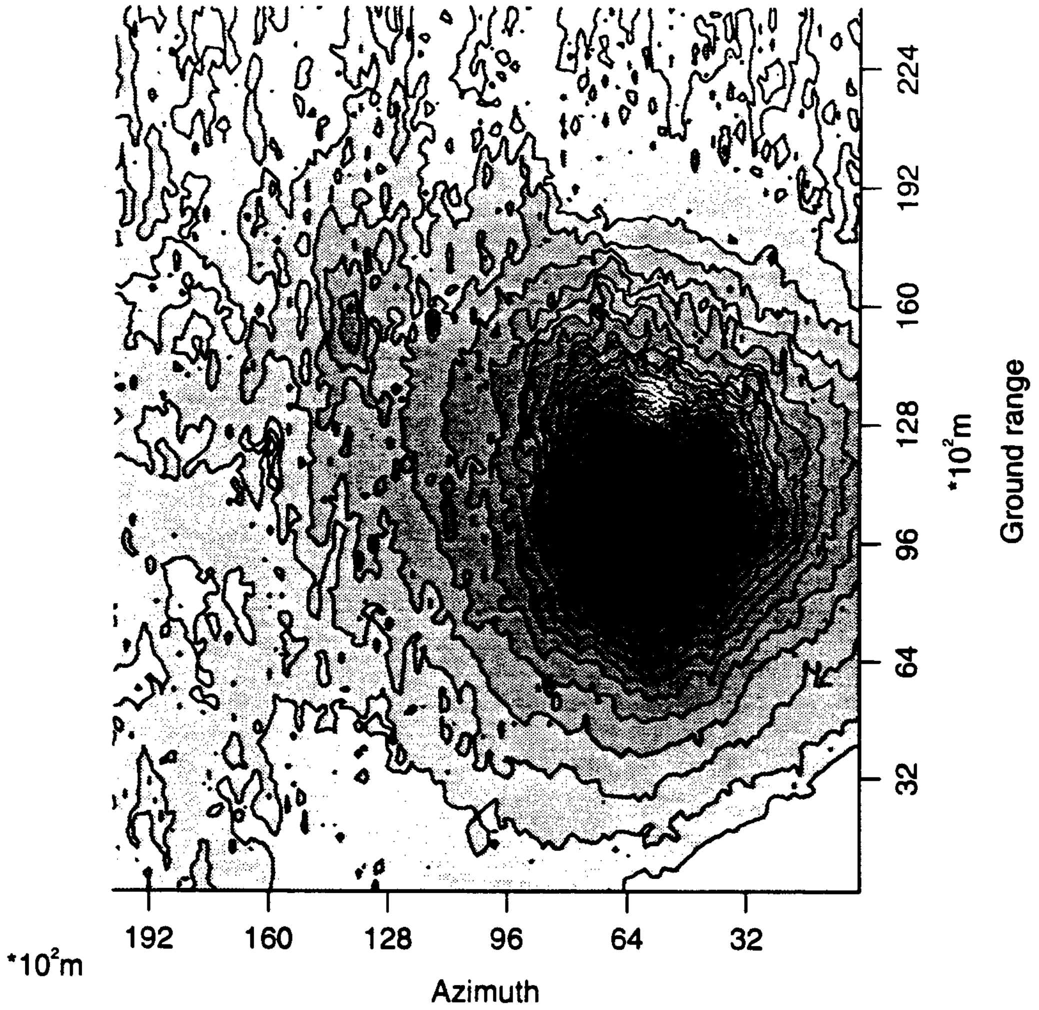

Figure 6.13: A topographic map of the area of Vesuvius obtained from the unwrapped and rectified phase using ascending orbits.

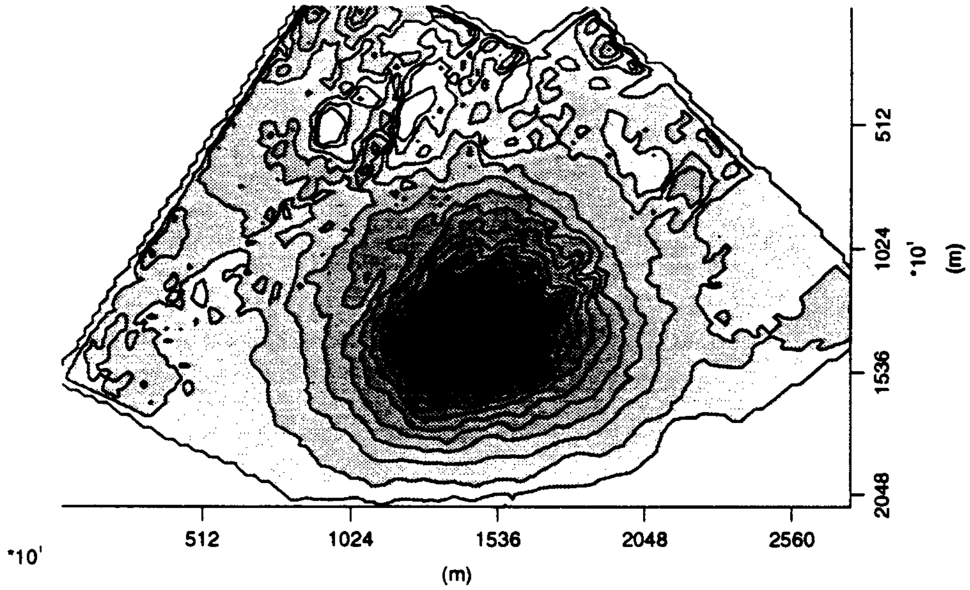

Figure 6.14: A topographic map of the area of Vesuvius obtained from the unwrapped and rectified phase using both ascending and descending orbits.

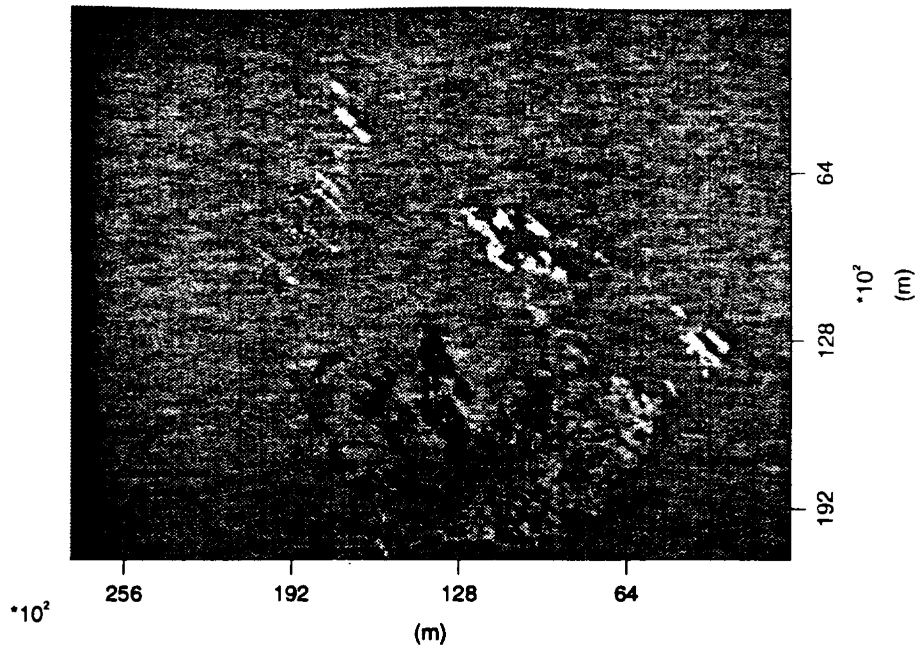

Figure 6.15: Elevation differences in high coherence areas between ascending and descending images (Black=40m, White=−40m).

rectification and reflectivity compensation. By a comparison with figures 5.3 and 5.5, it can be noted how the image intensity is now less dependent on terrain slopes [22, 23].

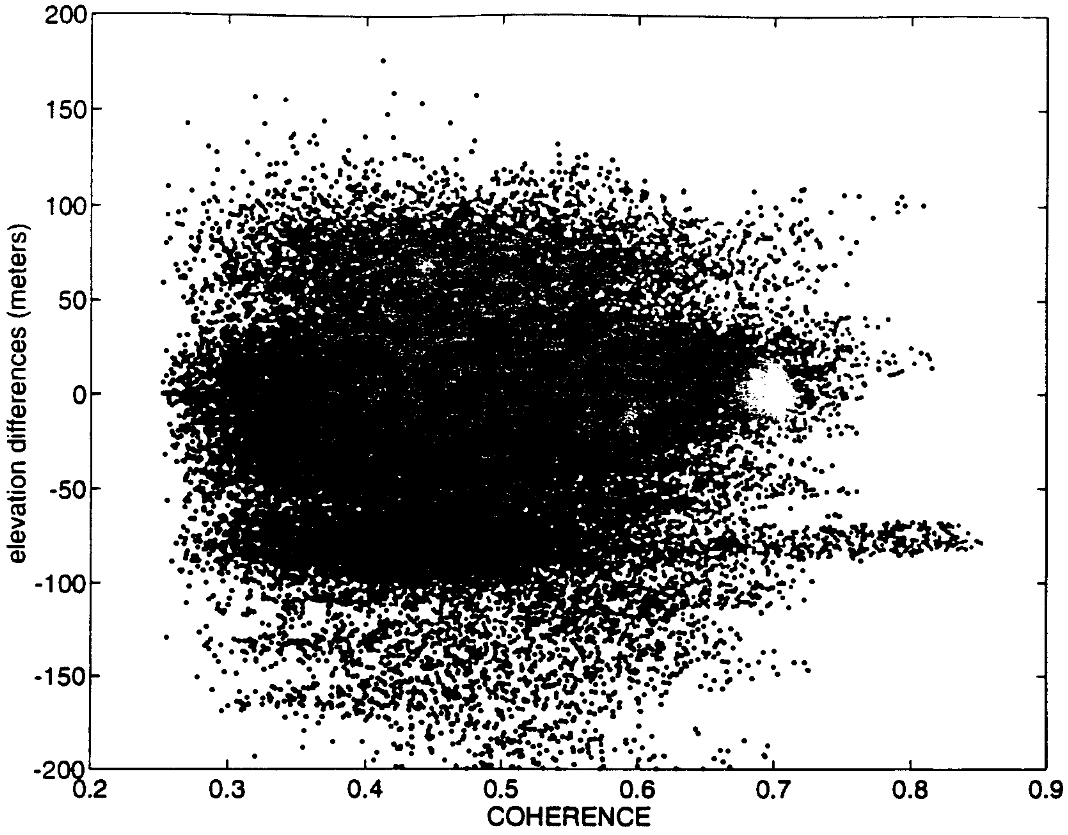

Figure 6.16: Elevation differences versus coherence

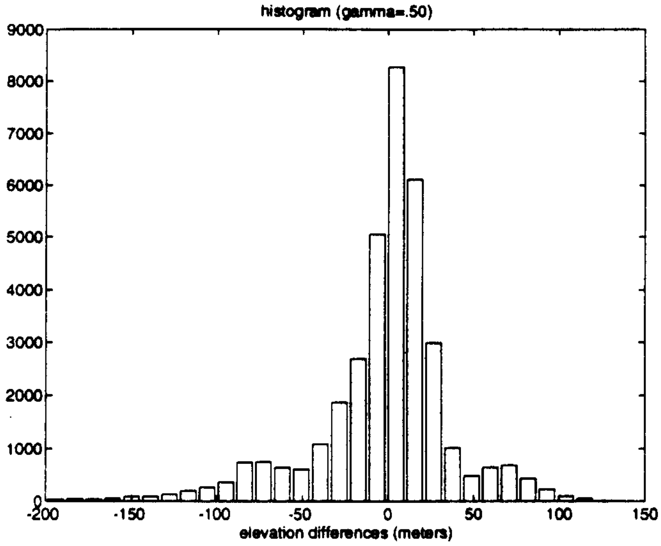

Figure 6.17: Histogram of elevation differences ($\gamma = .5$).

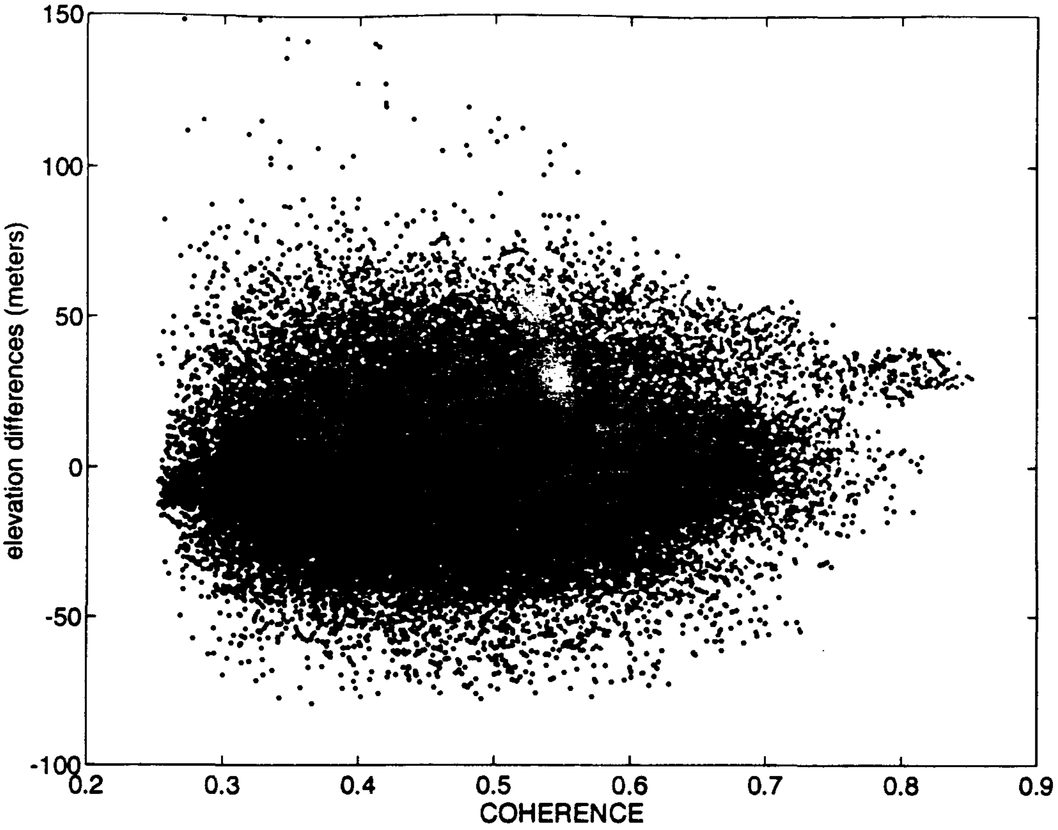

Figure 6.18: Elevation differences versus coherence after detrend.

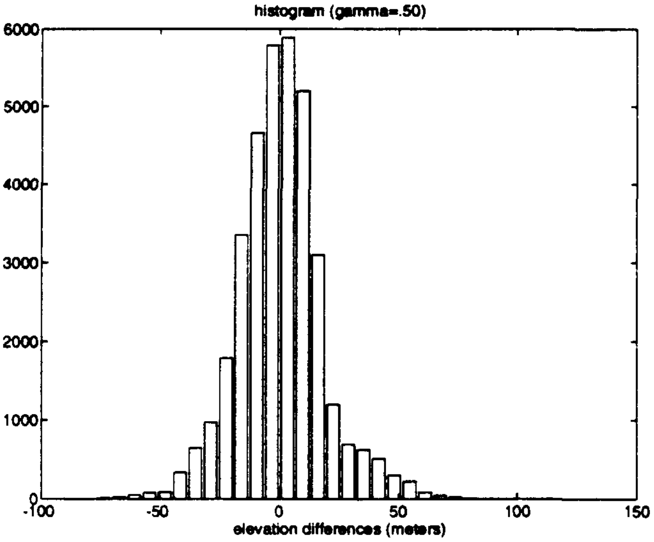

Figure 6.19: Histogram of elevation differences ($\gamma = .5$) after detrend.

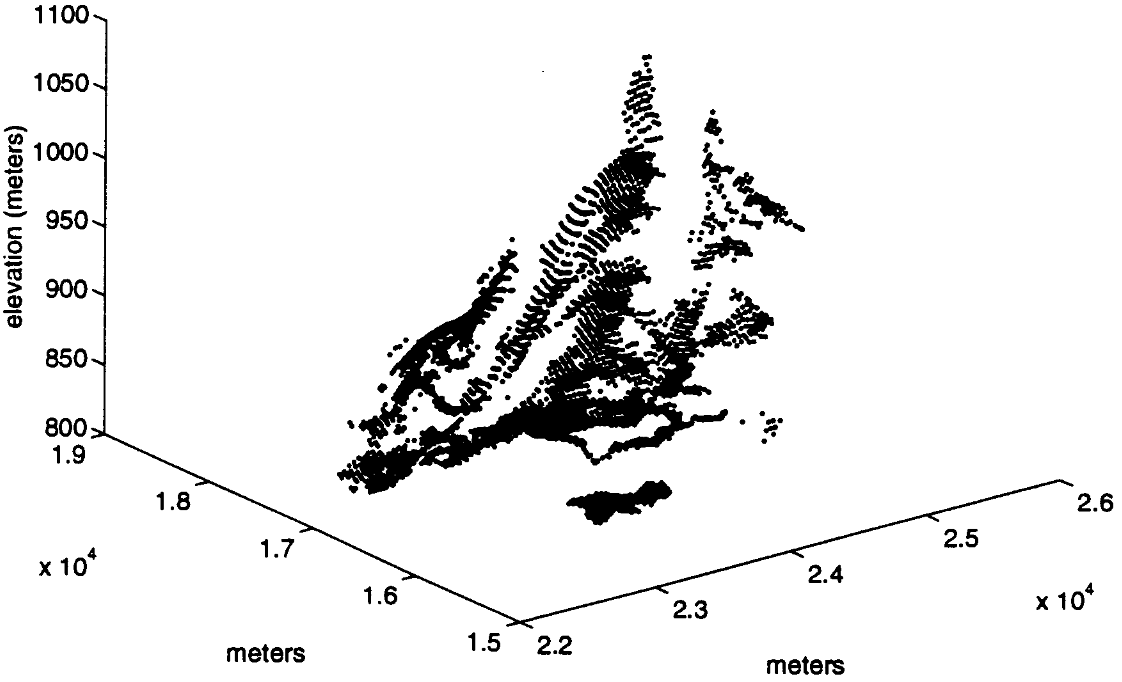

Figure 6.20: Perspective view of one side of Vesuvius. The area where outliers are concentrated has been highlighted by shifting it in elevation. The actual outliers location is the white almost rectangular hole close to the crossing of the horizontal axes.

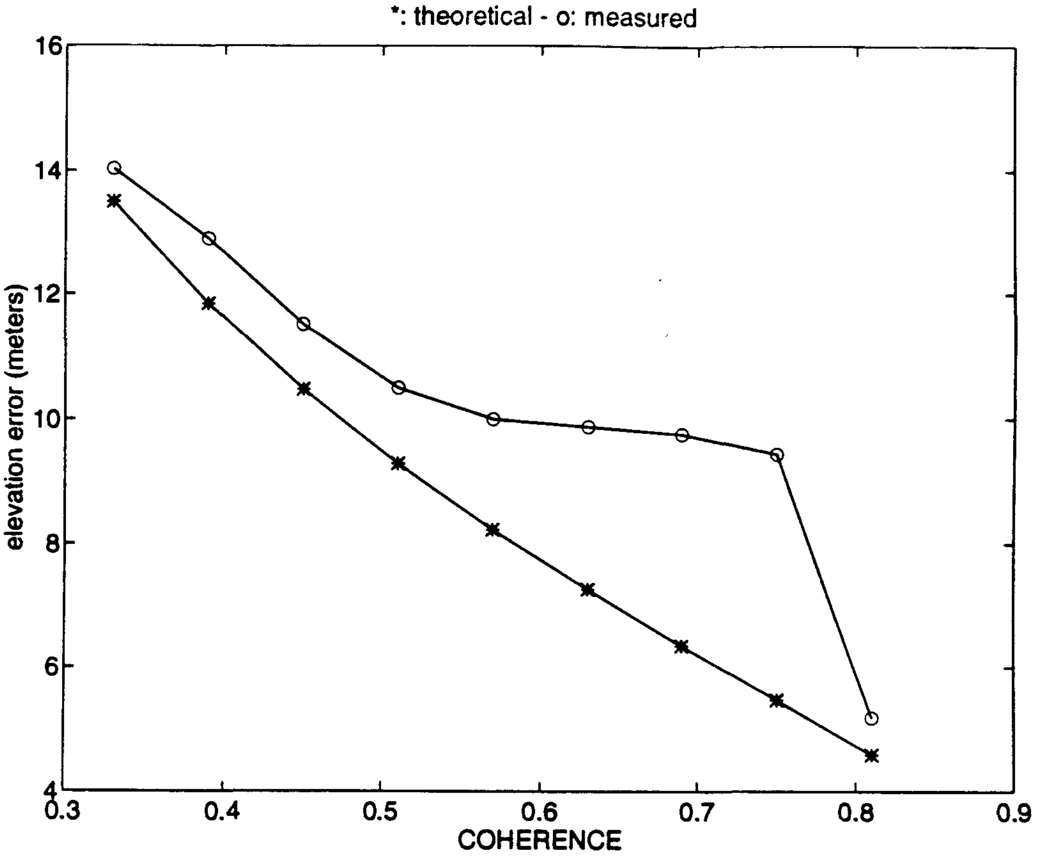

Figure 6.21: Elevation differences as a function of coherence: teoretical and measured values.

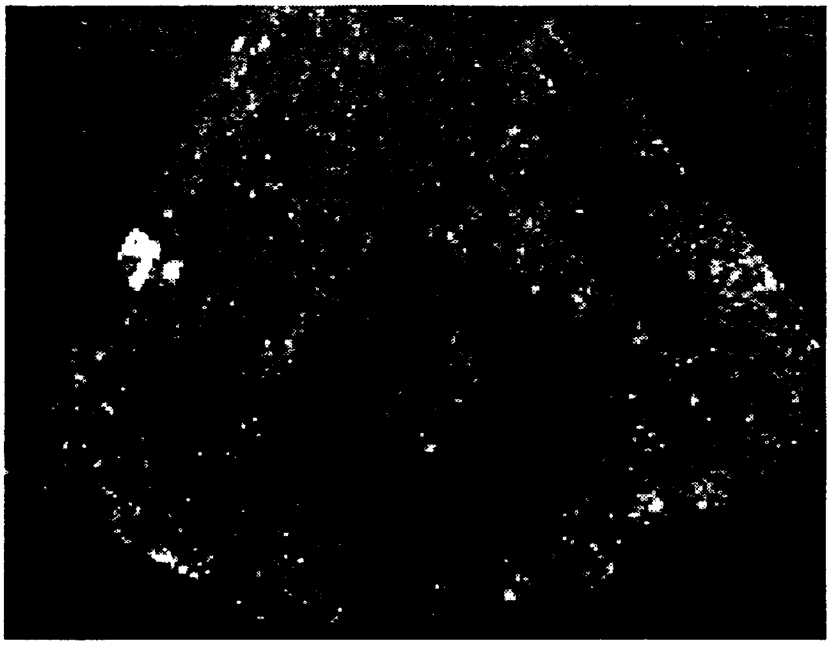

Figure 6.22: Combination of the detected images after geometric rectification and reflectivity compensation.

Chapter 7

MONITORING TERRAIN CHANGES

If the SAR acquisitions are not simultaneous, the interferogram phases (*fringes*) are also affected by the possible terrain changes.

Two types of temporal terrain evolution can be identified by means of multitemporal interferometric SAR images: decorrelation changes and small terrain motions.

Decorrelation changes. A random change of the position and physical properties of the scatterers within the resolution cell can be detected as low coherence of the images and it has been dealt with in section 4.

Small terrain motions. Centimetric slant range relative motions of local areas that occur between two SAR acquisitions, generate large local phase shifts in the interferogram. The phase difference $\Delta\phi_s$ generated by small terrain relative motions is governed by a mathematical relation completely different from that of the interferometric fringes (that, in order to avoid any confusion we shall indicate with $\Delta\phi_t$) described by equation 2.7. It is, in fact, proportional to the ratio between the relative motion Δs along the slant range direction and the transmitted wavelength λ:

$$\Delta\phi_s = \frac{2\Delta s}{\lambda} \tag{7.1}$$

Thus, if we have a non simultaneous interferometric SAR pair with a given baseline $B_n = n_s$ and a small terrain relative motion occurs between the two acquisitions, the following expression of the interferometric phase difference holds:

$$\Delta\phi = \Delta\phi_t + \Delta\phi_s = \frac{4\pi B_n n_p}{\lambda r_o} + \frac{2\Delta s}{\lambda} \tag{7.2}$$

From equation 7.2, it is clear that the two terms $\Delta\phi_t$ and $\Delta\phi_s$ should be separated in order to recover the terrain relative motion.

The simplest way to estimate small motions consists of choosing an image pair with a very small baseline (zero or a few meters would be sufficient in the case of ERS-1) so that the first term is much smaller than the second. An interesting example of such a solution is shown in figure 7.1. Two ERS-1 images of the area of Nice on the border between France and Italy, with a time interval of 9 days and a baseline $B_n = 6$m, have been used to generate an interferogram. In figure 7.1 the interferometric fringes are shown. Due to the very small baseline the fringes do not show rapid variations (even if the topography of that area is not flat at all) but for a small area close to the center of the map. In that area a very active landslide has being monitored by the group of the Institute de Physique du Globe (IPG) in Paris. From the ERS-1 interferometric data, an average landslide velocity of about 1cm per day has been estimated. The result is in good agreement with the data provided by the IPG group. Moreover, the ERS-1 interferometric SAR image provides a set of measurements of the landslide relative motion on a very dense grid (4×20 meters) at a cost that is much smaller than that of any other traditional techniques.

The accuracy of the motion measurement offered by such a technique has been recently tested with an ERS-1 experiment (the "Bonn experiment"), where elevation change as small as 9 mm of a few artificial radar targets (corner reflectors) has been detected with no ambiguity [24, 25, 26].

If a stereo SAR pair with a very small baseline is not available, the topography contribution to the interferometric phase ($\Delta\phi_t$) must be subtracted from the fringes. It can be accomplished in two different ways. If a topographic map of the area of interest is available, it has to be transformed in the azimuth slant range coordinates and scaled proportionally to the baseline of the interferometric pair in order to have an estimate of the phase component $\Delta\phi_t$. Then, it should be subtracted from the fringes (an impressive example of this technique has been shown at CNES [30] for the Landers earthquake).

As an alternative, an additional SAR image can be exploited in order to have an interferometric SAR pair with no terrain changes [31]. For the sake of simplicity, let us label the three SAR images with 1, 2 and 3 with no regard to their time consecution. Let us also assume that during the first two images no terrain changes occur. Thus, the fringes generated from the first two images will be proportional to the the phase $\Delta\phi_t$ to be subtracted from the fringes generated either from the couple $1-3$ or $2-3$. From equation 2.7, it is clear that the proportionality coefficient is given by the ratio of the two baselines B_{n12} and B_{n13} (or B_{n23}). However, since the proportionality holds on the phases and not on their principal values, the fringes obtained from the couple $1-2$ must be first unwrapped and then scaled.

Figure 7.1: ERS-1 SAR interferometry. Fringes generated from two images of the area of Nice on the border between France and Italy, with a time interval of 9 days and a baseline $B_n = 6\text{m}$.

Chapter 8

RANGE RESOLUTION IMPROVEMENT

The range resolution achievable from a single SAR complex image is limited by the system bandwidth:

$$\rho_r = \frac{c}{2W},$$

However, we will show how the image bandwidth (and so the resolution) can be enhanced by combining multiple surveys from different view angles. As an example, in the case of two surveys, a change in the view angle of $\Delta\theta$ causes a spectral shift (see section 3)

$$\Delta\omega = \frac{\omega}{\tan(\theta - \alpha)}\Delta\theta, \tag{8.1}$$

in this case, the coherent superposition of the two surveys could give one image with an enhanced bandwidth: $W_e = W + \Delta\omega/(2\pi)$. This is shown in figure 8.1: it can be noted that the parts not common to the two range spectra, that were filtered out in the interferometric processing, now represent the innovation present in one image with respect to another. If properly taken advantage of, this innovation can increase the signal band and hence the resolution in slant range. It's worth to note that the resulting band expansion, and hence the improvement of resolution in slant range is not constant in all the image points, but it is a function of the baseline and of the local slope angle of the ground α. In the points where α is positive, the spectrum shift and the obtainable improvement are maximum.

The processing required to get the super-resolution image, i.e. the coherent superposition of the surveys, requires the compensation for each scatterer, of the phase rotation due to the travel path distance between the scatterer and the couple of interferometric sensors. If we refer to the interferometric geometry of figure 1.1, we can express the super-resolution survey $s_{sup}(y)$ as follows:

$$\begin{aligned} s_{sup}(y) &= s_1(y) + s_2(y)\exp(-j\psi(y)) \\ \psi(y) &= 2\frac{\omega_0}{c}(r_{o2}(y) - r_{o1}(y)) \end{aligned} \tag{8.2}$$

being (s_1, s_2) the two complex surveys, and ψ the phase compensation term, that is a function of the target location and so changes with range.

It must be noted that, due to the bandwidth increase, the complex surveys (s_1, s_2) must be properly oversampled prior to computing the coherent superposition (8.2), in order to avoid aliasing.

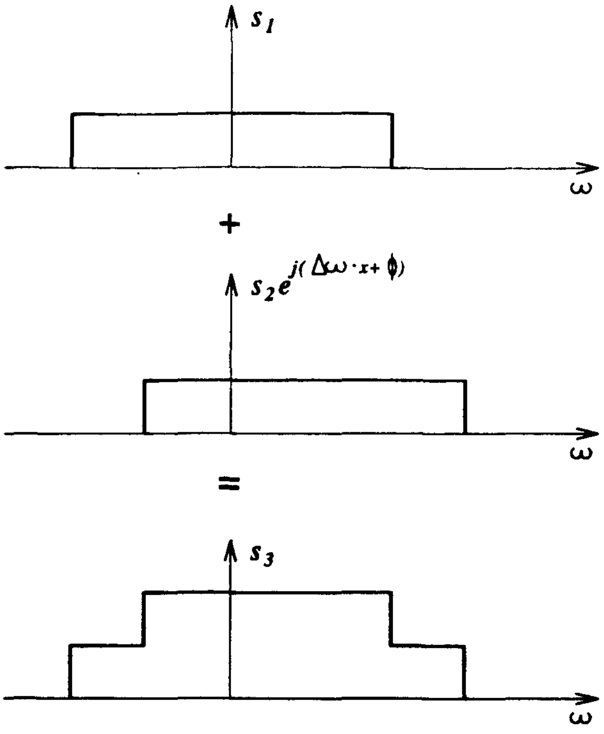

Figure 8.1: Modulation and correct summation

The required phase compensation $\psi(y)$ contained in the expression (8.2) is indeed the interferometric phase:

$$\psi(y) = E[s_1(y) \cdot s_2^*(y)],$$

and can be estimated using the techniques shown in section 3, provided that the surveys' spectra partially overlap. It's clear that the larger the frequency shift, the greater the resolution improvement; meanwhile the phase estimation is less robust.

8.1 Amplitude equalization

The coherent combination of the two surveys (8.2), that gives the super resolution image, must be amplitude equalized in order to give constant spectrum response. The fact is shown in figure 8.1: it can be noted that if no equalization is performed, the band common to the two spectra doubles its amplitude after the summation (if we hypothesize total correlation), whereas the innovative parts remain unaltered. The required equalization can be implemented by means of a proper surveys' filtering performed either before or after the coherent summation (8.2), as figures 8.2 and 8.3 show. However it will be shown that the approach explained in figure 8.2 (i.e. amplitude equalization performed prior to coherent superposition) leads to a simplified filter design.

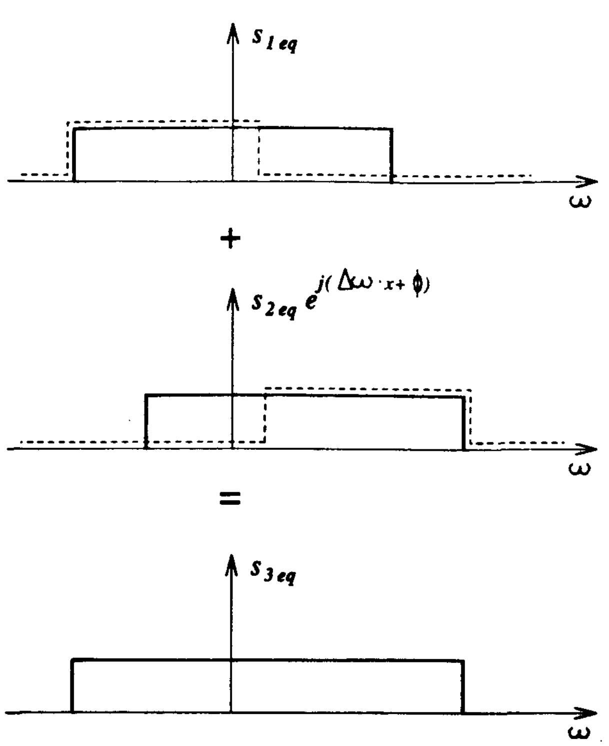

Figure 8.2: Equalization before the coherent summation

The spectral amplitude equalization is range variant, since it depends upon the local spectral shift, $\Delta f(y)$ and it is implemented in the space domain. The filters used to equalize spectrum amplitude should fulfill the following constraints:

1) Constant amplitude (all-pass) for the spectral components that represents innovation, i.e.:

$$\begin{array}{rclr} H_1(f) & = & 1 & f_{ny} - \Delta f < f < f_{ny} \\ H_2(f) & = & 1 & -f_{ny} < f < f_{ny} - \Delta f \end{array} \tag{8.3}$$

being $H(f)$ the filters to be designed, f_{ny} the Nyquist frequency and $\Delta f = \Delta\omega/(2\pi)$ the spectral shift.

2) Complementary transfer function in correspondence of the common spectral components:

$$H_1(f) + H_2(f) = 1 \qquad f_{ny} - \Delta f < f < f_{ny} - \Delta f \tag{8.4}$$

3) Zero phase, in order to allow the coherent superposition in equation (8.2)

These constraints can be satisfied by using bandpass symmetric FIR filters whose bandwidth and central frequencies depend on the local spectral shift: $\Delta f(r)$. The local slopes information obtained during the interferometric processing (i.e. for surveys filtering) are here exploited to derive the spectral shift.

A simplified filter design results if the amplitude equalization of the is performed on the interpolated surveys - a factor 2 interpolation both in azimuth and range is required to compute

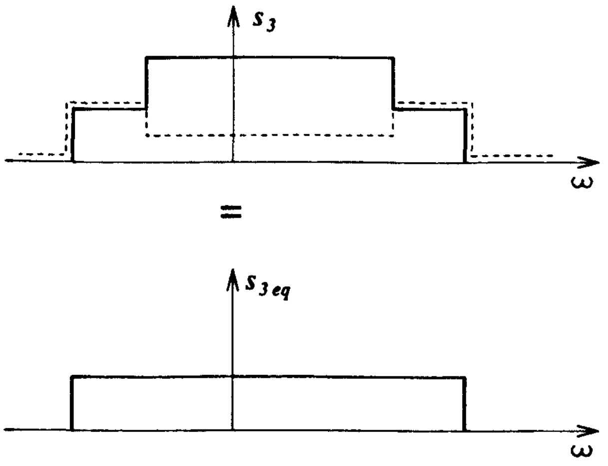

Figure 8.3: Equalization after the coherent summation

the interferogram. Moreover, this approach is required for the case of multiple surveys, that will be presented in the following. In this case, the conditions (8.3,8.4) can be relaxed, since the bandpass filter can be assumed fixed to half the total band (parts of the signal spectral components will be zero due to interpolation). Therefore a couple of fixed filter is designed, and a space variant modulation by a frequency of $\pm\Delta f/2$ is applied to fulfill the constraints. When modulating the filters, care should be taken in order to avoid phase shift between the two filters.

A correct amplitude equalization requires, besides a careful design of the filters, that the two surveys' energies are equalized as well, prior to computing their coherent superposition. The scaling factor can be applied, for example, when interpolating both surveys.

8.2 Super Resolution Algorithm

The algorithm used to get the superresolution image from two or more complex surveys is detailed in the figure 8.4. The requested steps have been discussed in the previous section, the generalization to the multiple surveys comes straightforward, by iteratively applying equation 8.2. The final image, s_{sup} can be obtained by the N step iteration (in the case of $N+1$ surveys):

$$s_{sup}^{n+1}(r) = s_{n+1}(r) * h_1(y) + e^{j\psi_{n,n+1}(y)} s_{sup}^{n}(y) * h_2(y) \tag{8.5}$$

, where $\psi_{n,n+1}(y)$ identifies the interferometric phase derived from the couple (s^n, s^{n+1}). In this way the innovative components of the spectra of the starting images are progressively added one to the other ("stack") and the band of the spectrum of the generated image increases with each step. It is necessary to check that with growth the band does not go beyond $2f_{N_y}$, resulting in aliasing; interpolation will avoid this.

Equalization is carried out at each step before making the coherent summation. In this case it is not possible to use only a filter as the spectrum band of the high resolution image increases by different quantities from point to point. The filters used are monodimensional FIR computed by means of an Hamming window.

An experimental example of the super-resultion technique exposed has been performed on ERS-1 data. In 1992, this satellite flew over an area that included the city of Bonn 10 times

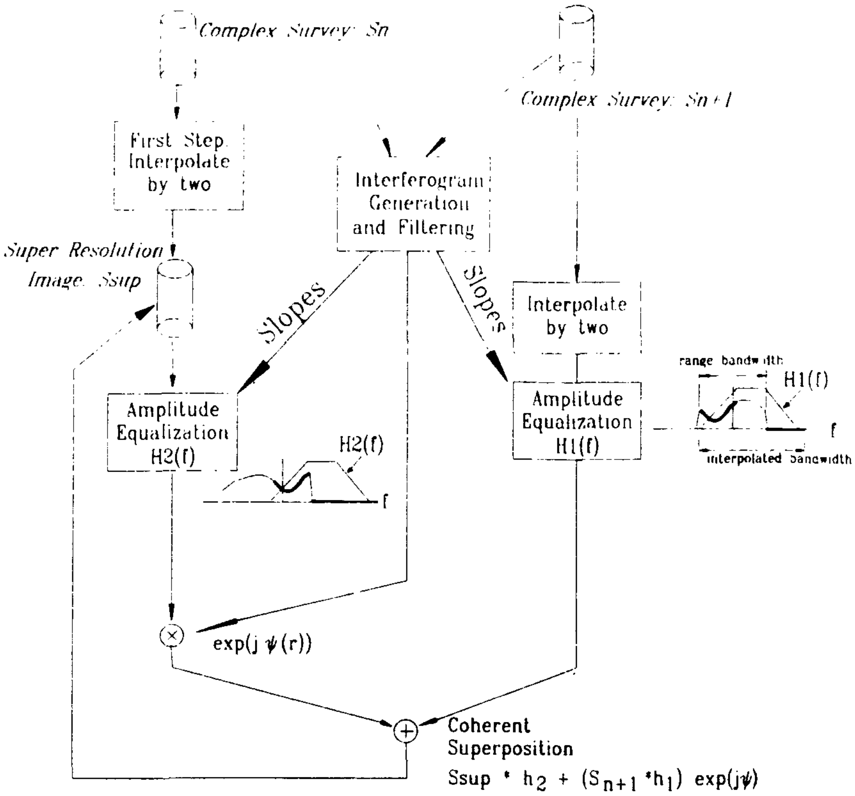

Figure 8.4: Super Resolution algorithm for multiple surveys

between the 2 and 29 March, i.e. once every three days.

The images have been ordered respecting the spatial position of the passings in such a way that, on going from the first to the last, the off-nadir angle θ always increases (or decreases). The sequence chosen was one of decreasing off-nadir angles. The minimum normal baseline of the sequence is 12 meters, whilst the maximum is about 427 meters. Considering that in the case of ERS-1 the critical baseline is about 1100 meters for level ground ($\alpha = 0$), decorrelation does not occur along the sequence, though the first image and the last, having a normal baseline equal to 1418 meters, are themselves totally uncorrelated.

In reality not all the images were used in the experiment; several couples showed very short horizontal baselines, so there was only a small gain for quite a marked computational load. For the sake of speed several sequence images were skipped, taking care, however, that there was no decorrelation along the new sequence.

For level ground the spectrum can be widened by adding 22.4 MHz. With respect to the original band of 16 MHz, the improvement obtained is 140%; the resolution in slant range is more than doubled.

The images of the sequence were focussed and aligned and the interferogram generated for each consecutive pair of images in the sequence. The experiment of super-resolution was carried out on images of 512 × 256 samples (azimuth×slant range) of part of the city of Bonn.

Estimated from the interferograms was the local spectrum shift according to the periodogram technique with an estimation cell of 17 × 9 samples (azimuth×slant range) filled with zeros to give a window of 64 × 64 samples on which the FFT was calculated. The estimated values were needed for the "cleaning" operation of the original images, from which the "cleaned" interferograms were generated. Following this, each "cleaned" interferogram was locally pass-band filtered to obtain the phase ψ_f needed for the rephasing.

Figures 8.7 and 8.8 show the original interferogram phases "cleaned" and that pass-band filtered for one of the pairs of the sequence. The filter used has a passing band equal to 2/10 of the Nyquist frequency.

Figure 8.10 shows one of the images of the sequence. The coherent superposition of all the images, that is the final result of the experiment, is shown in figure 8.11: numerous details are much more distinguishable cleanly cut, like the railway (from the upper right to the bottom of the image) and the highways (from left to right half-way up the image). It should also be noted that the river, at the top of the image, appears darker than in the original image, whilst the buildings appear clearer: this is due to the effect of the coherent mean highlighted earlier.

Figure 8.9 is a map of the area.

The improvement in the resolution obtained can be better appreciated in figures 8.5 and 8.6, that represent the course of the module of the interferometric signal in correspondence with two natural reflectors (two buildings) before and after the super-resolution procedure.

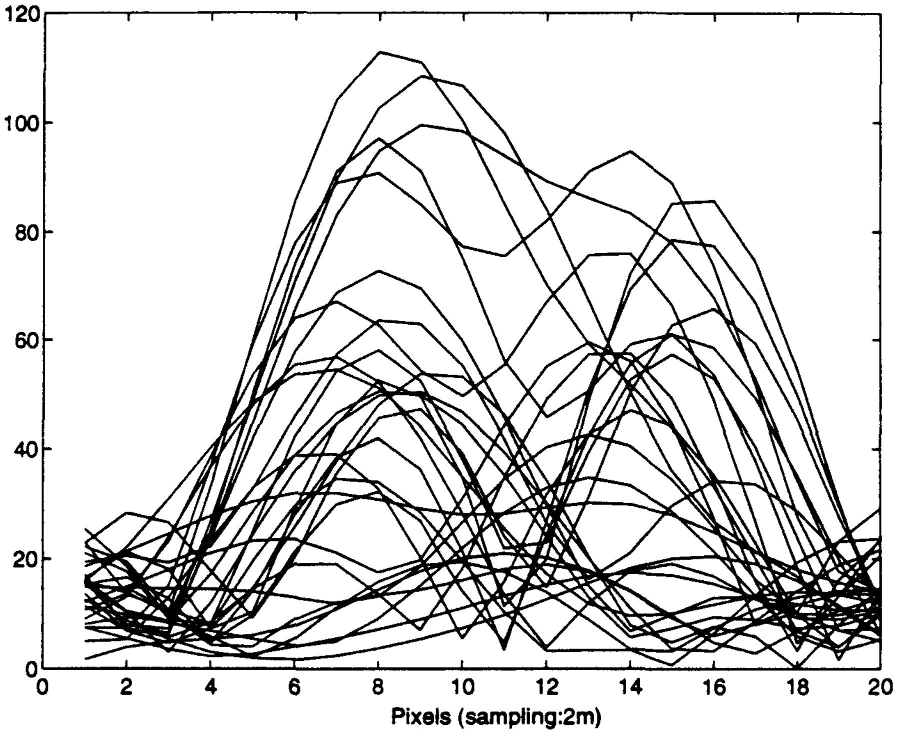

Figure 8.5: Plot of the original natural reflectors

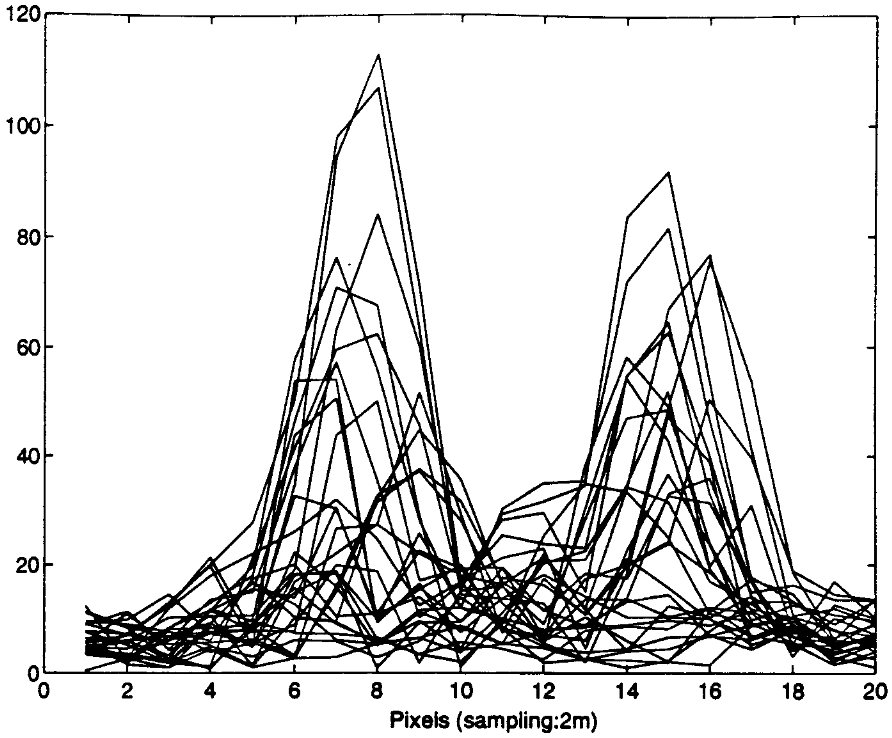

Figure 8.6: Plot of the same natural reflectors in the image at super-resolution

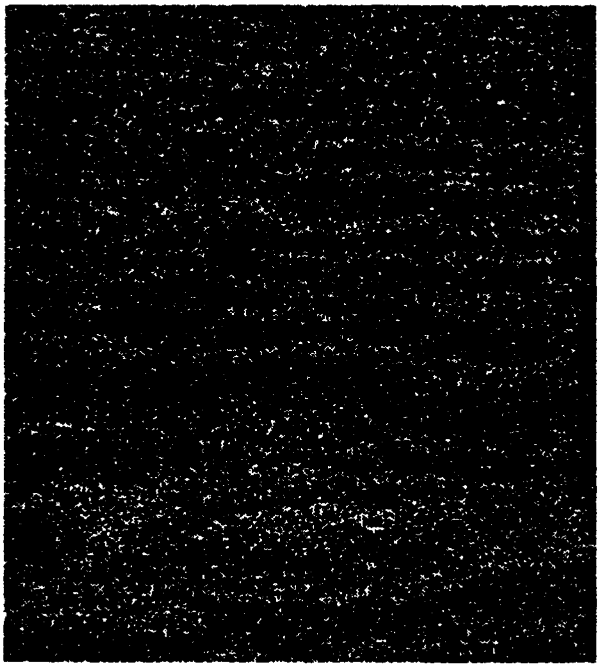

Figure 8.7: Original Phase

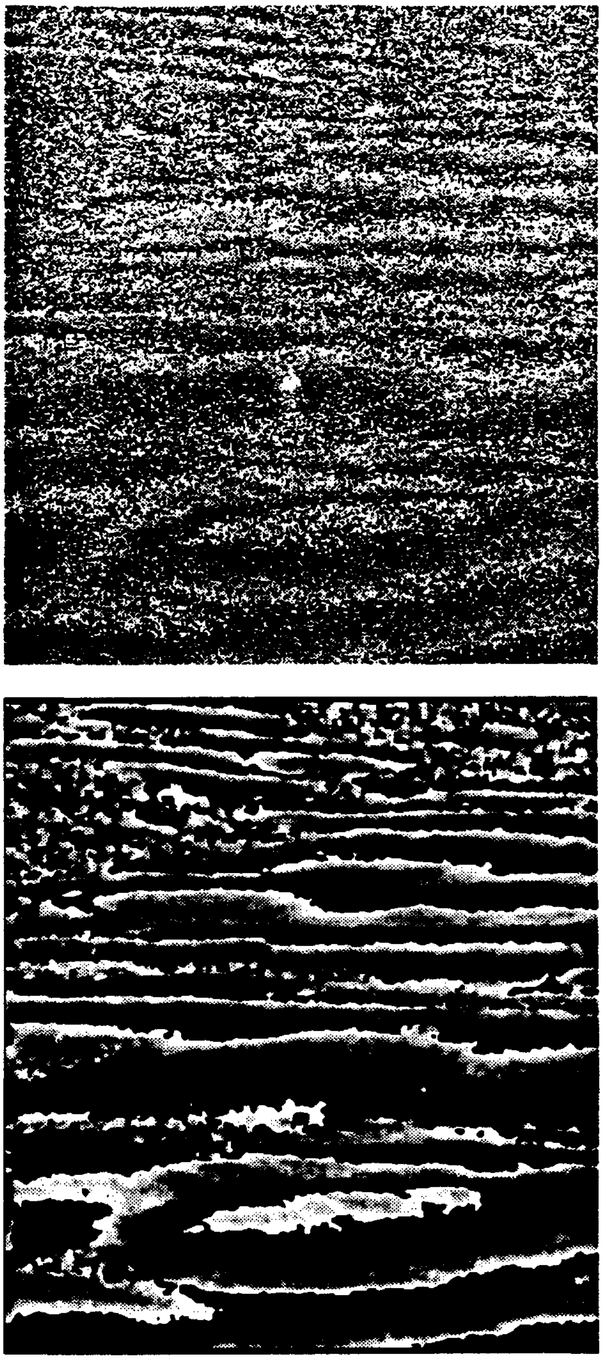

Figure 8.8: Phases “cleaned” (upper) and pass-band filtered locally (lower)

Figure 8.9: Map of Bonn area

Figure 8.10: Single image of Bonn

Figure 8.11: Image of Bonn at super-resolution

Chapter 9

CONCLUSIONS

In this report, processing techniques finalized to SAR interferometry have been analyzed and several applications presented. Some techniques have been studied in detail and no significant improvements are expected in the future. Others have been considered but they should be further investigated. As far as applications are concerned, only stimulating examples have been shown here. The applications need to be further tested and developed in a multi-disciplinary environment.

In the following we summarize the techniques discussed and the related applications with a short comment on their possible development.

- **Interferogram and coherence map generation.** A code has been developed. It includes automatic images registration (up to 1/100 of a pixel), prefiltering and slope driven smoothing (maps of terrain slopes in azimuth and range are produced as part of the processing). These steps, together with differential focusing, are finalized to get the best achievable fringes and coherence. No significant modifications are expected apart from a sensible speed up of the software. Interferogram and coherence maps can be considered final as well as intermediate products. They can be used for classification, segmentation and terrain slope compensation of backscattering; applications that need to be further investigated. On the other hand, both coherence and fringes are used as a starting point for DEM generation. The quality of the final result depends on the achieved degree of coherence.

- **Phase unwrapping with two images.** Phase unwrapping is a crucial step for DEM generation. It has been shown that automatic phase unwrapping is not an easy goal to deal with. What we think to be the best strategy can be summarized in three steps:

  i - Deterministic unwrapping of high coherence regions. It is based on the already published "ghost lines" algorithm [2, 29].

  ii - Consistent alignment of the resulting isolated regions. and removal of a multiple 2π phase difference between the isolated regions introduced during the first step. This can be done in two ways: manually, if a map and reference points are available; automatically, if more than two interferometric images are available (see next point).

  iii - LMS unwrapping of the rest of the image. It is a technique suitable for approximate phase unwrapping in low coherence area.

A prototype has been developed at Polimi.

- **Phase unwrapping with multiple baselines.** If more than two images are available the alignment of isolated regions can be done automatically. It is shown that after an accurate registration in space, frequency and phase of the images, the phase of each pixel is linear with the baseline. The slope of the line is proportional to the pixel elevation. Encouraging results come from simulations. However, the technique has to be further validated with large scale experiments.

- **DEM generation.** Unwrapped phase can be exploited for DEM generation. A problem derives from the image deformation due to SAR geometry. As the terrain slope along range approaches the off-nadir angle (foreshortening areas), no elevation information can be extracted. However, if ascending and descending passes are considered, terrain coverage is increased. Those areas affected by foreshortening in one image are well covered (if not in shadow) in the other image. After a precise georeferentiation the elevation maps obtained from ascending and descending passes can be combined to generate a DEM. Then, the combination of multiple images would allow the desired vertical resolution (as it has been shown in in the Bonn experiment [25] where an elevation accuracy of 2 meters has been achieved). No operative software is available yet. However, an experiment with ERS-1 data of Vesuvius has been carried out. An elevation map of Vesuvius has been generated with the combination of interferograms taken from ascending and descending passes of ERS-1. The first estimate of the baselines has been obtained from the ancillary data. Then, the coastline has been exploited to improve the accuracy of the estimates. Since no existing DEM was available to us, other than a 1:25000 map, the consistency of the results have been checked by considering elevation differences in high coherence areas of both ascending and descending images. A large systematic error (ranging from -40 to $+40$ meters) proportional to the estimated elevation (from 0 to 1200 meters) has been measured. This effect depends on the estimation error of geometric parameters probably due to the inaccuracy of the used ground control points. In the next future the systematic inconsistencies will be used as an information to get a better estimate of the unknown parameters.

- **Range resolution improvement.**

  The range resolution achievable from a single SAR complex image is limited by the system bandwidth. However, the image bandwidth (and so the resolution) can be enhanced by combining multiple surveys from different view angles. The technique has been demonstrated with the combination of six ERS-1 images. A SAR image of Bonn have been obtained with twice the range resolution usually allowed by ERS-1 showing many interesting features not visible in the single image. An operative software has been developed at Polimi.

- **Volumetric effects.** It is an important field of investigation. When backscattering comes from targets with different elevation within the resolution cell, volume effects arise affecting the images coherence. It has been demonstrated that from multi-baseline observations, it is possible to derive a LMS estimate of the surface and volumetric scattering contributions. As an example, six ERS-1 images of the area of Bonn have been exploited for this goal after registration in space and frequency. The volumetric contribution has been subtracted from the images and their coherence increased. However, it should be noted that the coherence improvement is partly due to volume effects subtraction being also affected by temporal changes. If just a few images are available this estimation technique appears to be reliable where temporal changes are not relevant. Further studies are needed.

- **Terrain motion measurements.** Differential interferometry has been validated as a unique tool to measure centimetric terrain motion on a large scale. A few dramatic examples have been presented in [30, 25, 32]. For one, the average velocity of a landslide close to the border between Italy and France has been measured (i.e. 1 cm/day). This result is in a good agreement with other available data confirming the potentiality of this technique.

Appendix A

COHERENCE ESTIMATION

We have seen that coherence can be regarded as an estimate of the achievable elevation accuracy on a pixel by pixel basis. For convenience, we shall here recall briefly some results on coherence estimation. The key parameter (n) is the so called "degrees of freedom" [18]. As a first approximation, in the case of SAR images, it can be computed as the ratio between the pixel size of the coherence and that of the full resolution image, if the baseline is small. With increasing baselines, though, the common band shrinks, the pixels become correlated and the coherence estimates biased towards 1; in our example the degrees of freedom is 64. The absolute value of the measured coherence (g) given the true coherence (γ) and the degrees of freedom (n), follows the Goodman density function [19]:

$$P(g/\gamma,n) = \frac{2(1-\gamma^2)^n}{\Gamma(n)\Gamma(n-1)} g(1-g^2)^{n-2} \sum_{k=0}^{\infty} \frac{\gamma^{2k}\Gamma^2(n+k)}{\Gamma^2(k+1)} g^{2k} \tag{A.1}$$

As an example this density function is shown in figures A.1 and A.2 for $n = 16$ and $n = 64$ respectively.

Foster and Guinzy[18], derived the posterior probability of γ from equation A.1, by exploiting the Bayes theorem with the assumption of a uniform prior density for γ:

$$P(\gamma/g,n) = \frac{P(g/\gamma,n)}{\int_0^1 P(g/\gamma,n)d\gamma} \tag{A.2}$$

From this equation the maximum likelihood estimate of the true coherence (that value of γ for which the posterior probability is a maximum) as well as the associated confidence intervals can be computed.

As an example, the posterior density functions for $n = 16$ and $n = 64$ (i.e. our example) are plotted in figures A.3 and A.4. Notice that it is not symmetric and that its dispersion increases for small values of coherence as well as for small degrees of freedom.

However, as a rule of thumb, we can define a threshold of coherence $\overline{g}$ below which the "maximum likelihood" estimate of the coherence is zero. That is the largest value of coherence in correspondence of which the posterior density function shows the largest value in the origin (see figure A.3 for $g = 0.2$). It depends on the degrees of freedom only and is approximately:

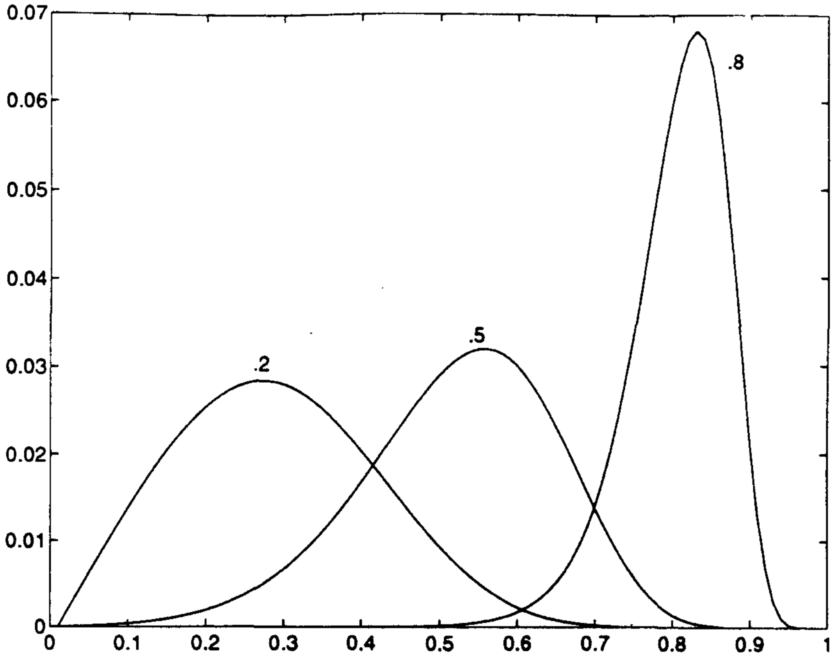

Figure A.1: Goodman density function. Degrees of freedom: 16.

$$\overline{g} = \frac{1}{\sqrt{n}} \tag{A.3}$$

In our example, $\overline{g} = 0.125$.

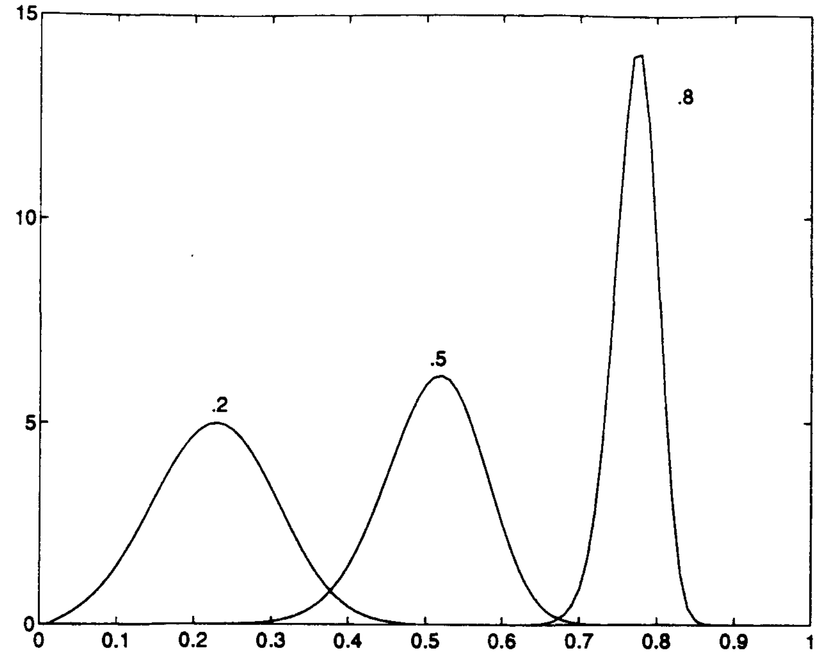

Figure A.2: Goodman density function. Degrees of freedom: 64.

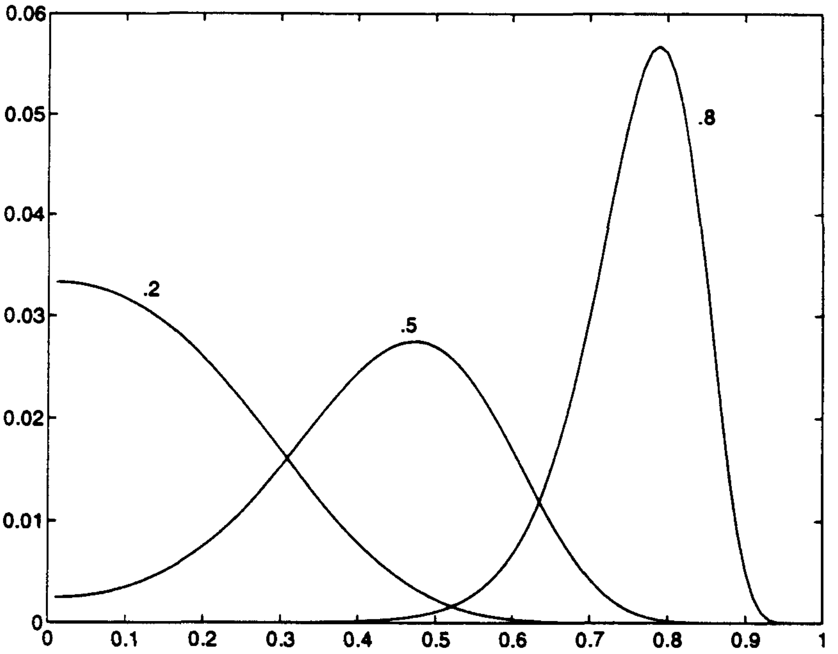

Figure A.3: Goodman posterior density function (Foster and Guinzy). Degrees of freedom: 16.

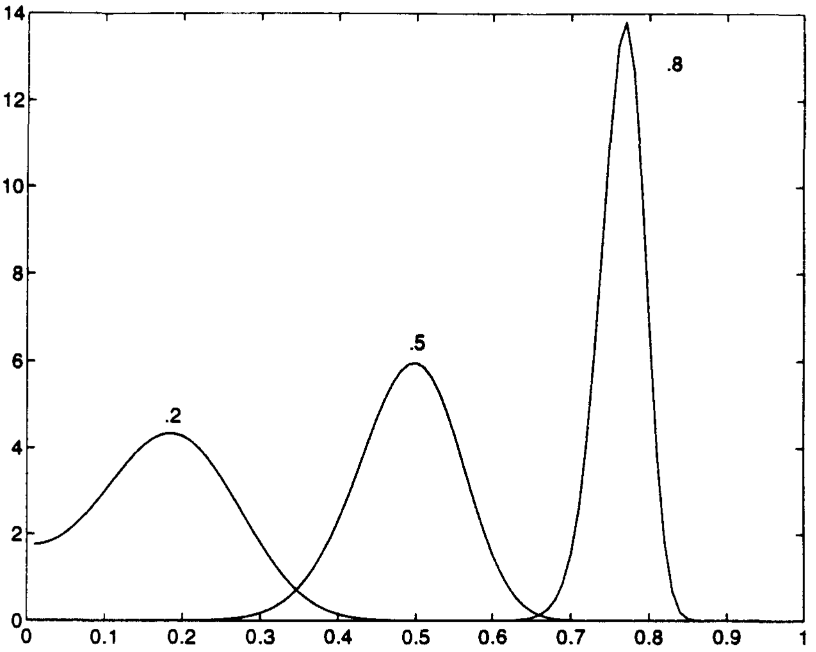

Figure A.4: Goodman posterior density function (Foster and Guinzy). Degrees of freedom: 64.

Appendix B

SOFTWARE FOR INTERFEROGRAM GENERATION

In figure B.1 a schematic diagram of the software for interferogram generation is presented.

A first coarse registration between interferometric images is estimated by exploiting the cross-correlation between detected images (block #2).

A more accurate registration, with a sub-pixel precision, is obtained by maximising the amplitude of the complex coherence in different zones of the images, some in near and some in far range (block #3).

Parameters for registration are applied to one of the images, to obtain a pixel-by-pixel correspondence (block #4).

The interferogram is now generated by means of images cross-multiplication (block #5).

Frequencies correspondent to layover areas are then eliminated by half-band filtering (block #6).

A first guess of the flat terrain phase is obtained from ancillary data; it is used to flatten the interferogram (block #7).

A first estimate of local derivatives in range and azimuth is obtained from the subsampled interferogram with the periodogram technique (block #9).

These derivatives are used to eliminate the uncorrelated part of the spectrum of the two images and to compute the local complex coherence (blocks #9 and #10).

A new interferogram is generated from filtered images (blocks #11, #12, #13 and #14) and it is used to produce a more accurate estimation of local derivatives. The first estimate of local derivatives (block #9) is used to demodulate locally the interferogram, and the new derivatives are estimated by averaging the principal value of phase differences between adjacent pixels in the two directions (block #15).

Local derivatives are then used to band pass the interferogram (block #16). The estimation and filtering can be iterated using narrower and narrower filters.

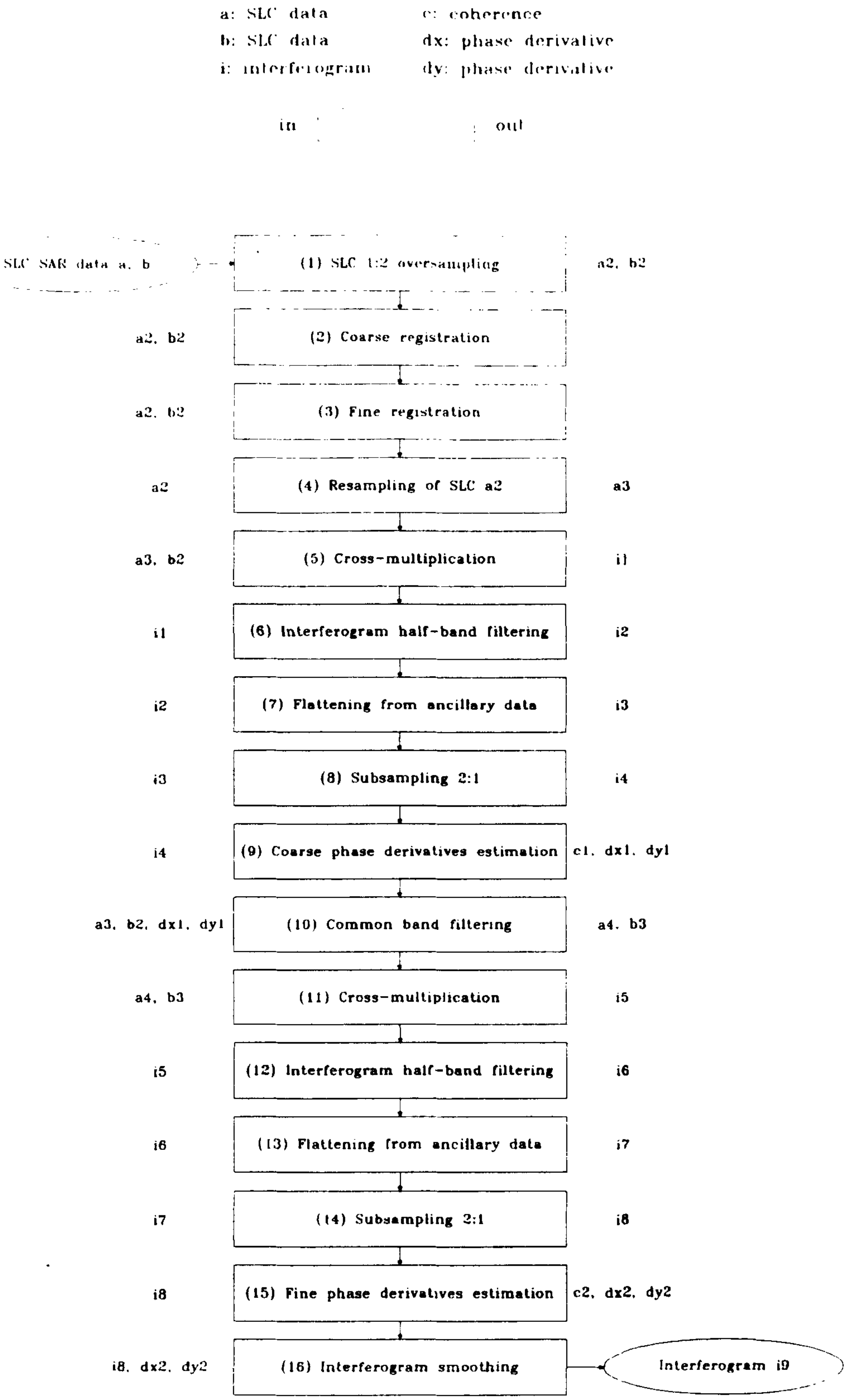

Figure B.1: Schematic diagram of the interferometric software.

Bibliography

[1] Gabriel A., Goldstein R., 1988, *Crossed orbits interferometry: theory and experimental results from SIR-B*, Int. Jou. on Remote sensing, 9, No.5, 857-872.

[2] Prati C., Rocca F., Monti Guarnieri A., Damonti E., 1990, *Seismic migration for SAR focusing: Interferometrical applications*, IEEE Transactions on Geoscience and Remote Sensing, Vol.28, N.4, pp.627-640.

[3] E. Rodriguez, J.M. Martin, 1992, *Theory and design of interferometric synthetic aperture radars*, IEE Proceedings-F, Vol.139, No.2, pp.147-159.

[4] P. Piau, J-C. Cael, M. Deschaux, A. Lopes, *Analysis of the resolution of multitemporal SAR systems*, Proceedings of IGARSS'93, Tokyo, August 1993, pp. 1196-1199.

[5] A. J. Sieber, 1993, *The European Microwave Signature Laboratory*, EARSel Advances in Remote Sensing, Vol. 2, No. 1, January 1993, pp. 195-204.

[6] C. Prati, F. Rocca, *Range resolution enhancement with multiple SAR surveys combination*, Proceedings of IGARSS'92, Houston, May 1992.

[7] C. Prati, F. Rocca, 1993, *Improving slant range resolution of stationary objects with multiple SAR surveys*, IEEE Transactions on AES, Vol. 29, No.1, 135-144

[8] C. Werner, S. Hensley, R. M. Goldstein, P. A. Rosen, H. A. Zebker, *Techniques and applications of SAR interferometry for ERS-1: Topographic mapping, change detection, and slope measurement*, Proc. First ERS-1 Symposium, Cannes, 4-6 November 1992, pp. 205-210.

[9] E. Rodriguez, J.M. Martin, 1992, *Theory and design of interferometric synthetic aperture radars*, IEE Proceedings-F, Vol.139, No.2, pp.147-159.

[10] R. Bamler, *A Comparison of Range-Doppler and Wavenumber Domain SAR Focusing Algorithms*, IEEE Trans. on Geoscience and Remote Sensing, Vol. 30, n.4, 1992, pp. 707-713.

[11] C. Cafforio, C. Prati, F. Rocca, 1991, *SAR data focusing using seismic migration techniques*, IEEE Transactions on AES, Vol.27-2, pp.194-207.

[12] R. K. Raney, 1992, *An exact wide field digital imaging algorithm*, International Journal of Remote Sensing, 13-5, pp.991-998.

[13] H. Runge, R. Bamler, 1992, *A novel high precision SAR focussing algorithm based on chirp scaling*, Proceedings of IGARSS'92, Houston, pp. 372-375.

[14] N. Leuratti, 1990, Dissertation for the degree of Dottore in Ingegneria, Politecnico di Milano.

[15] Q. Lin, J. F. Vesecky, *Topography estimation with interferometric Synthetic Aperture Radar using fringe detection*, Proceedings of IGARSS'91, Helsinki, 1991, pp.2173-2176.

[16] F. Vinelli, Experimental Activities on ERS-1 Reference Data Set, Proceedings of 1st SAR Interferometry Workshop, ESA ESRIN, Frascati, 12th October 1992.

[17] C. Cafforio, F. Rocca, 1976, *Methods for Measuring Small Displacements of Television Images*, IEEE Transactions on Information Theory, Vol.IT-22, No.2, pp.573-579.

[18] FOSTER, M. R. and GUINZY, J., 1967, The Coefficient of Coherence, its Estimation and Use in Geophysical Data Processing. *Geophysics*, 32, pp.602-616.

[19] GOODMAN, N. R., 1963, Statistical Analysis Basend on a Certain Multivariate Complex Gaussian Distribution (An Introduction). *Ann. Math. Stats.*, 34, pp.152-177.

[20] Lefauconnier B., Chorowicz J., Deffontaine B., Parrot J.F., Rudant J.P., Massonnet D., Rabaute T., *Validation of SAR (Synthetic Aperture Radar) data from ERS-1 on Spitsbergen, Svalbard. Preliminary glaciological and geomorphological interpretation*, Proc. Second ERS-1 Symposium, Hamburg, 11-14 October 1994, pp. 171-176.

[21] Goldstein R.M., Zebker H.A., Werner C.L., 1988, Satellite radar interferometry: Two-dimensional phase unwrapping, Radio Science, Vol.23, N.4, pp. 713-720.

[22] Ulander L., Hagberg J., *Use of InSAR for Radiometric Calibration over Sloping Terrain*, SAR Calibration Workshop, ESTEC - Noordwijk, 1993, pp.147-159.

[23] Werner C., Rosen P., *Topographic Slope form the SAR Interferometric Phase Gradient*, Proceedings of PIERS'93, Pasadena - CA, 1993, p. 922.

[24] Ph. Hartl, M. Reich, K. Thiel, Y. Xia, *SAR Interferometry applying ERS-1 - Some preliminary test results*, Proc. First ERS-1 Symposium, Cannes, 4-6 November 1992, pp. 219-222.

[25] C. Prati, F. Rocca, A. Monti Guarnieri, *SAR interferometry experiments with ERS-1*, Proc. First ERS-1 Symposium, Cannes, 4-6 November 1992, pp. 211-218.

[26] A. Monti Guarnieri, F. Parizzi, P. Pasquali, C. Prati, F. Rocca, *Developments in ERS-1 SAR interferometry*, Proc. of 1st Workshop FRINGE, ESA-ESRIN, Frascati, 12 Ottobre 1992.

[27] U. Spagnolini, 1991. 2-D Phase Unwrapping, *Proceeding of SEG*, Houston - Texas, Vol. II, pp. 1350-1353.

[28] U. Spagnolini, 1993, 2-D Phase Unwrapping and Phase Aliasing, Geophysics, Vol.58, N.9, pp.1324-1334.

[29] M. Giani, C. Prati, F.Rocca, 1992, "SAR interferometry and its applications", ESA report N.8928/90/F/BZ.

[30] D. Massonnet et al., *The Displacement Field of the Landers Earthquake Mapped by Radar Interferometry*, Nature, Vol.364, July 8, 1993, pp.138-142.

[31] Gabriel A.K., Goldstein R.M., Zebker H.A., *Mapping small elevation changes over large areas: differential radar interferometry*, Journal of Geophysical research, Vol.94, N.B7, July 1989, pp.9183-9191.

[32] F. Gatelli, A. Monti Guarnieri, F. Parizzi, P. Pasquali, C. Prati, F. Rocca, *The wavenumber shift in SAR interferometry* , to appear in IEEE Transaction on GARS